High Efficiency Quasi-Optical Mode Converters for Overmoded Gyrotrons

by

Monica Blank

B.E.E., The Catholic University of America (1988)
M.S.E.E., Massachusetts Institute of Technology (1991)

Submitted to the Department of Electrical Engineering and Computer Science
in partial fulfillment of the requirements for the degree of

Doctor of Philosophy

at the

MASSACHUSETTS INSTITUTE OF TECHNOLOGY

September 1994

Author .....
Department of Electrical Engineering and Computer Science
August 5, 1994

Certified by .....
Dr. Richard J. Temkin
Senior Research Scientist, Physics Department
Thesis Supervisor

Accepted by .....
Professor Frederic R. Morgenthaler
Chairman, Departmental Committee on Graduate Students

High Efficiency Quasi-Optical Mode Converters for Overmoded Gyrotrons

by

Monica Blank

Submitted to the Department of Electrical Engineering and Computer Science
on August 3, 1994, in partial fulfillment of the
requirements for the degree of
Doctor of Philosophy

Abstract

This thesis reports on the design and experimental verification of two novel high efficiency quasi-optical mode converters for gyrotron oscillators. Gyrotrons produce high order $TE_{m,p}$ modes ($m, p >> 1$) at high frequencies (100–300 GHz). These modes must be converted to low order linearly polarized modes for transmission in corrugated waveguides or open mirror transmission lines. Because traditional waveguide converters are inefficient and impractical for very high order modes, quasi-optical mode converter techniques must be developed. Both converters described in this thesis achieved 95% conversion efficiency from high order waveguide modes to Gaussian-like beams in free space, allowing them to be used in practical high power continuous wave (cw) gyrotrons.

A Vlasov-type converter was designed to transform the $TE_{16,2}$ cylindrical waveguide mode at 146 GHz to a Gaussian beam in free space. The converter consists of a helically cut waveguide launcher and a doubly curved focussing reflector. The preliminary design of the converter was made with the geometric optics approximation. A vector diffraction theory was developed to simulate the launch and propagation of the beam through the converter system and to modify and improve upon the design made with geometric optics theory. The analysis reported in this thesis was the first full diffraction theory calculation to predict the output of the Vlasov-type converter. The converter was built and tested on a MW power level, $3\mu s$ pulsed gyrotron operating in the $TE_{16,2}$ mode at 146 GHz. Calorimetric power measurements and focal plane scans showed that 95% of the $TE_{16,2}$ power leaving the gyrotron was directed to a Gaussian-like focus in the far field. Beam expansion measurements indicated that 88% of this power was contained in the TEM_{00} fundamental Gaussian mode, giving an overall conversion efficiency of 83%. The beam was then directed into a 1.25 in. diameter corrugated waveguide and calorimetric measurements showed an efficiency of 82.5% for converting the $TE_{16,2}$ to the HE_{11} mode of the corrugated guide. Experimental results were compared to predictions of vector diffraction theory and good agreement was obtained. The Vlasov-type converter also provided a novel method for determining the mode mix of the radiation leaving the gyrotron.

A pre-bunching converter, which is a modified Vlasov-type, was designed to transform the $TE_{22,6}$ cylindrical waveguide mode at 110 GHz to a Gaussian beam in free space.

The converter consists of an irregular waveguide section followed by a step cut launching aperture and two focussing reflectors. The irregular waveguide section, which was designed with coupled mode theory, is used to bunch the radiation into Gaussian bundles prior to the launch. The reflectors that follow were designed with Gaussian optics and vector diffraction theory, and their surfaces are simple toroidal shapes. The converter was built and tested on a MW power level, 3μs pulsed gyrotron operating in the $TE_{22,6}$ mode at 110 GHz. Experiments showed that the $TE_{22,6}$ power leaving the gyrotron was directed to a small, Gaussian-like focus in the far field. Beam expansion measurements indicated that virtually all the power in the beam was contained in the TEM_{00} mode. The beam was directed into a 1.25 inch corrugated waveguide and calorimetric efficiency measurements showed that 98% of the $TE_{22,6}$ power leaving the gyrotron was coupled to the HE_{11} mode of the corrugated guide. The experimental results were compared to predictions of vector diffraction theory and good agreement was obtained. Four additional reflectors were built to transform the fundamental Gaussian beam, produced by the launcher and first two reflectors, into two fundamental Gaussian beams of approximately equal power level. The surfaces of the beam splitting reflectors are simple sinusoidal and toroidal shapes, which are compact and easy to manufacture. Measurements showed that the mirror relay produced two Gaussian-like beams, one containing 52% of the power leaving the gyrotron and the other containing 42%, giving a total efficiency of 94%. The results show that simple sinusoidal and toroidal mirrors can be used to produce high quality Gaussian beams. The simplicity of the mirror surfaces greatly reduces the large computing times necessary for a full diffraction theory analysis of the system.

The results presented in this thesis show great promise for the use of quasi-optical mode converters in high power cw gyrotrons.

Thesis Supervisor: Dr. Richard J. Temkin
Title: Senior Research Scientist, Physics Department

Thesis Supervisor: Dr. Kenneth E. Kreischer
Title: Principal Research Scientist

Thesis Reader: Professor Hermann A. Haus
Title: Professor of Electrical Engineering and Computer Science

Thesis Reader: Professor Frederic R. Morgenthaler
Title: Professor of Electrical Engineering and Computer Science

Acknowledgments

I would like to express my gratitude to all the people who have helped me with my thesis work, especially my supervisors, Drs. Richard Temkin and Kenneth Kreischer. In addition, I owe a great debt to Dr. Jeffrey Casey and Anita Li, who got me started on the quasi-optical converter problem. Their codes and experimental techniques provided the foundation for this entire thesis. I truly appreciate the assistance I received from the scientists in the group, Drs. William Guss, Bruce Danly, and Shien Chi Chen. I would also like to thank all the students in the group, especially Philipp Borchard, who's microwave scanner simplified and improved my measurements, and Will Menninger, who solved so many geometry problems for me. I appreciate all the laboratory aid from Mark Basten and Terry Grimm. Also, I am grateful to William Mulligan and George Yarworth for keeping the experiment in running order and for all their technical advice. Lastly, I thank Profs. Haus and Morgenthaler, my thesis readers.

Contents

Chapter 1

Introduction

1.1 Background

Gyrotron oscillators are efficient, high power, high frequency sources of coherent electromagnetic radiation. Gyrotron research is driven by the need for powerful sources in the hundreds of GHz range, where conventional microwave devices are limited to low output power and lasers are inherently inefficient. The primary use of gyrotrons is in the electron cyclotron resonance heating (ECRH) of fusion plasmas [1] [2]. Gyrotrons also have applications in the fields of plasma diagnostics [3], radar systems, communications, and materials processing [4].

The typical configuration of a gyrotron oscillator is shown in Fig. 1.1. A magnetron injection gun emits an annular beam of electrons, which is guided by an axial magnetic field. As the beam enters a region of high magnetic field, it is compressed and the perpendicular velocity of the electrons is increased. The beam then travels into a resonant cylindrical cavity, where perpendicular energy in the electrons is transferred to an rf wave. As the beam leaves the cavity, it travels into a region of lower magnetic field and, thus, expands. The beam is collected on a copper surface while the rf wave continues to propagate along the collector and exits through a vacuum window. In order for a gyrotron to be operated in the continuous wave (cw) regime, the ohmic losses on the walls of the cavity must be kept low, typically below 2 kW/cm^2. For high power, high frequency operation, this ohmic loss constraint necessitates the use of large, highly overmoded cavities.

Recently, much progress has been made in the development of megawatt power level, overmoded gyrotron oscillators [5] [6]. Generally, the high order $TE_{m,p}$ modes ($m, p >> 1$) produced by gyrotrons are not suitable for long path transmission or plasma heating. For efficient transport and heating, the radiation must be converted to linearly polarized, low order waveguide modes or Gaussian modes in free space.

Conversion of high order modes to low order modes using conventional waveguide converters is cumbersome and lossy. The conversion is made in several stages, stepping through intermediate modes on the way from the input mode to the final low order output

mode. This stepwise process leads to very long converters, which are impractical and difficult to manufacture in many cases. The conversion can become inefficient due to ohmic losses on the converter walls or the excitation of undesired modes in the overmoded waveguide where so many modes can propagate. Because conventional in-guide conversion from high order modes to low order modes is inefficient and impractical, novel mode converter techniques must be developed. This thesis investigates two quasi-optical mode converters, the Vlasov-type [7-11] and pre-bunching [12] [13] converters.

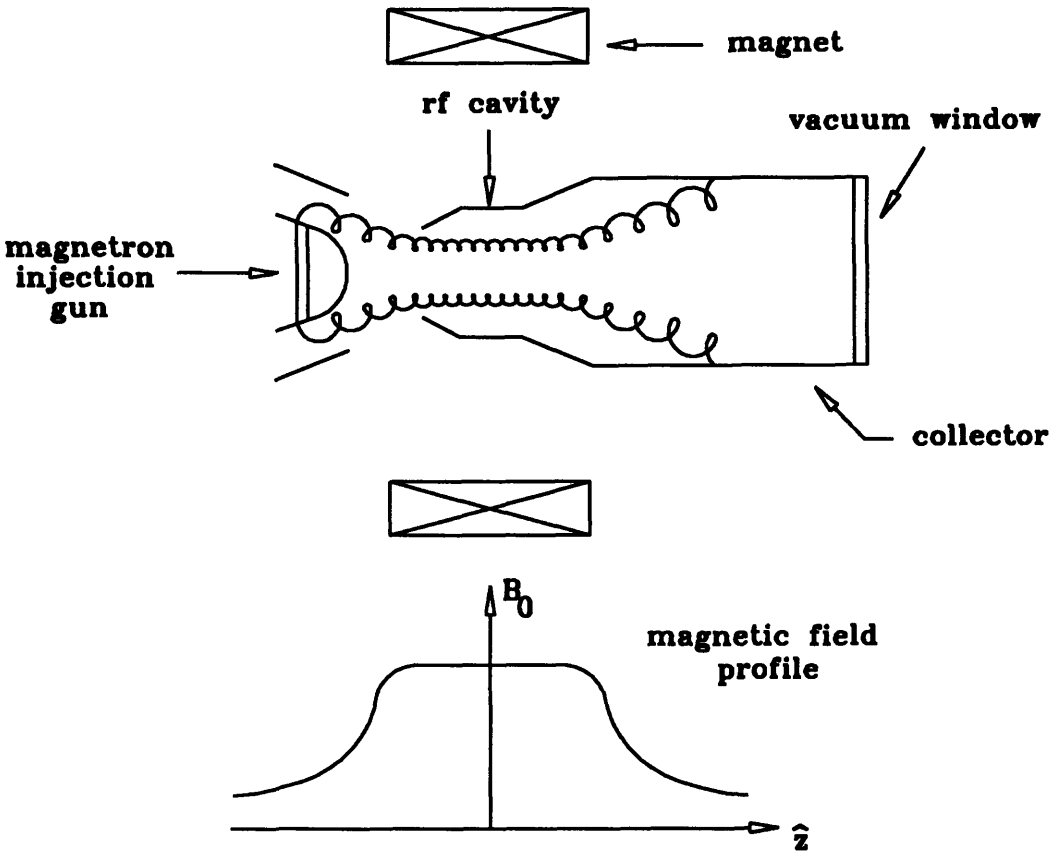

Figure 1.1 Schematic of a typical gyrotron oscillator.

The Vlasov-type converter, shown in Fig. 1.2, consists of a helically cut waveguide launcher and a doubly curved focussing reflector, which directs the radiation to a small, Gaussian focus. The fundamental designs of the launcher and reflector, proposed by Vlasov *et al.* in 1975 [7], are rooted in the geometric optics approximation. An experimental

investigation of the original device [7], in which a Vlasov converter was used to transform the $TE_{10,1}$ cylindrical waveguide mode to a narrow beam in free space, achieved a modest power transfer efficiency of 80%. Since the introduction of the Vlasov converter, several modifications and improvements have been reported. A rigorous conservation of energy calculation was performed to find the optimum helical cut length [11]. Also, shaped sub-reflector surfaces were added to the launcher to improve its radiation properties by reducing side lobes [14,15,16]. These additional reflector surfaces were designed using geometric optics techniques. In this thesis, a rigorous vector diffraction theory was developed to simulate the Vlasov-type converter operation and predict the final output beam.

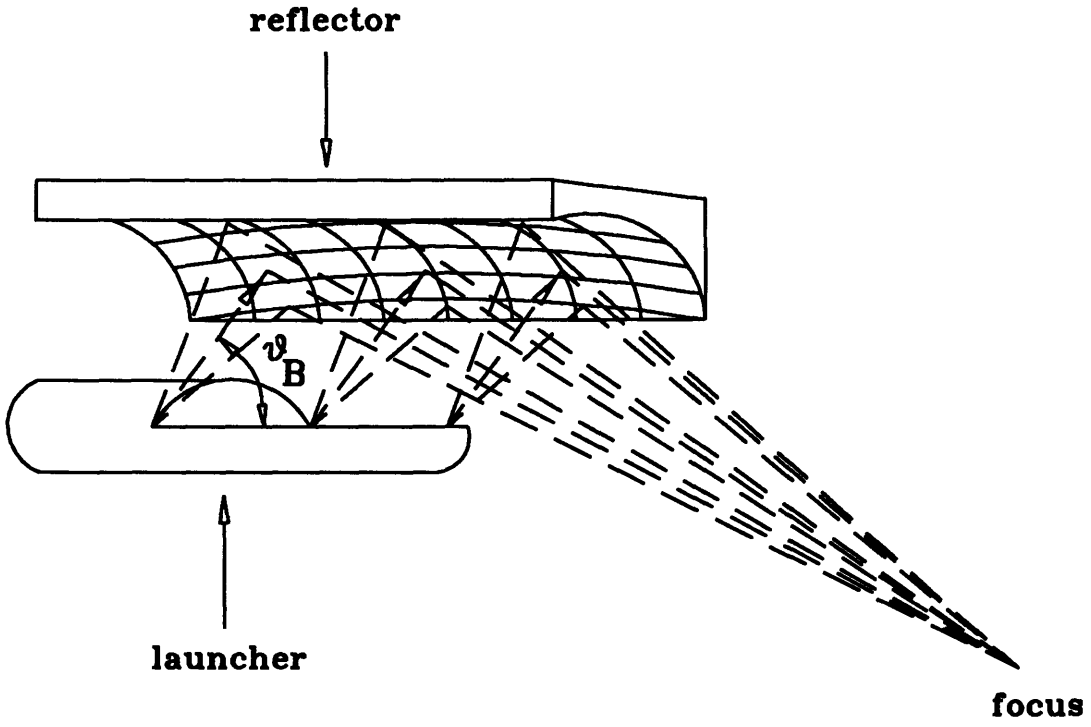

Figure 1.2 Schematic of the Vlasov-type converter, consisting of a helically cut launcher and a doubly curved focussing reflector.

The pre-bunching converter, which is a variation on the Vlasov-type, consists of a rippled wall waveguide section, followed by a step cut launching aperture (Fig. 1.3) and a series of focussing reflectors. The rippled wall waveguide, which is designed using coupled mode theory, bunches the incident radiation into Gaussian bundles so that an elliptic Gaussian beam is launched from the step cut. This type of pre-bunching launcher, along with the subsequent phase correcting mirrors, was proposed by Denisov *et al.* in 1992 [12]. Denisov *et al.* [12] investigated a pre-bunching launcher, along with a mirror relay to provide phase correcting and focussing, designed to transform the $TE_{15,4}$ mode at 110 GHz to a Gaussian beam in free space. Experiments [12] showed a power transfer efficiency of 95%, which is substantially higher than the efficiency observed for a Vlasov-type converter with sub-reflector shaping mirrors (87%). In this thesis, it is shown that simple, toroidal shaped mirrors, designed with Gaussian optics and vector diffraction theory, can be used to transform the beam radiated from the pre-bunching launcher to a fundamental, circular Gaussian beam suitable for transmission in an open mirror relay or a corrugated waveguide. In addition, a rigorous diffraction theory to simulate the operation of the pre-bunching converter was developed as part of the work of this thesis.

Because of limitations on the power handling capability of the gyrotron window, it may prove advantageous to divide the power produced in the oscillator and direct it out of the vacuum through two windows. In this thesis, a novel beam splitting mirror relay, consisting of toroidal and sinusoidal shaping reflectors, is investigated. This mirror relay, in conjunction with the pre-bunching converter, is used to divide a fundamental Gaussian beam into two Gaussian beams of approximately equal power. The simply shaped reflectors provide a beam splitting mirror relay that is compact and easy to manufacture.

1.2 Thesis Overview

This thesis presents a theoretical and experimental investigation of novel mode converters. The objective is to design, construct, and test efficient quasi-optical mode converters to transform high order cylindrical waveguide modes produced by gyrotron oscillators to Gaussian-like beams in free space. Converters for two specific gyrotrons will be investigated, the first operating in the $TE_{16,2}$ mode at 146 GHz and the second operating in the $TE_{22,6}$ mode at 110 GHz. The design of the converters, as well as the experimental demonstration will be described. Experimental results will be compared to predictions of a vector diffraction theory, which was developed as part of the work of this thesis.

This thesis is organized in the following manner. Chapter 2 describes the design and experimental verification of the $TE_{16,2}$ Vlasov-type converter. In Chapter 3, the modified

Vlasov-type converter, or pre-bunching converter, which was designed for the $TE_{22,6}$ mode, is discussed. The theory and experimental verification of the novel beam splitting mirror relay is also described in Chapter 3. Chapter 4 details theory and experiments investigating the competition between counter rotating modes in a gyrotron oscillator, an issue which is crucial to the success of the quasi-optical mode converters described in this thesis. In Chapter 5, the theoretical and experimental results are summarized.

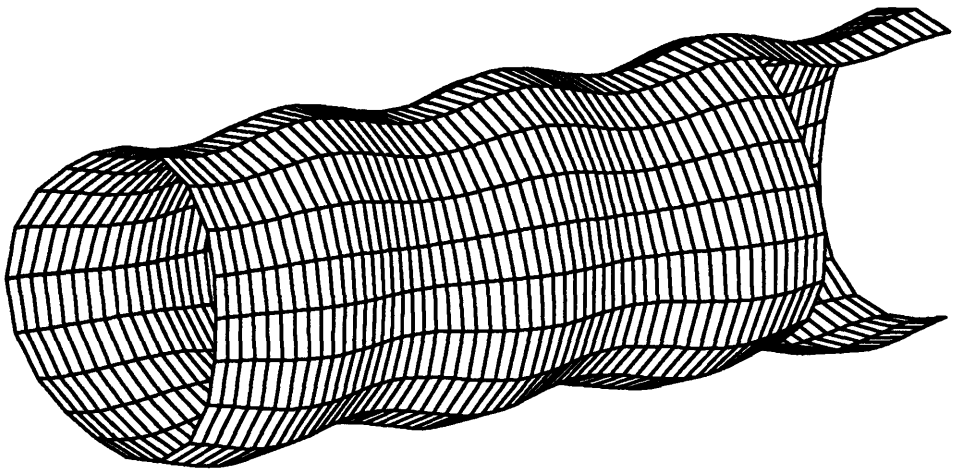

Figure 1.3 Rippled wall waveguide section, shown with greatly exaggerated ripple amplitude.

Chapter 2

Vlasov-Type Converter

A Vlasov-type converter was designed to transform the $TE_{16,2}$ cylindrical waveguide mode at 146 GHz to a Gaussian-like beam in free space. The converter consists of a helically cut waveguide launcher and a doubly curved focussing reflector (Fig. 1.2). The launcher was designed with geometric optics theory, while both geometric optics and vector diffraction theories were used to calculate the reflector parameters. The converter was built and tested on a megawatt power level gyrotron oscillator. The theoretical analysis and experimental verification of the converter are described below.

2.1 Geometric Optics Theory

In an effort to simplify the design of the Vlasov-type converter, the geometric optics approximation of waveguide modes was used. The geometric optics model is rigorously correct only in the limit where the wavelength approaches zero. However, the ray model is useful when the dimensions of the launcher are large compared to the wavelength, λ. In the case considered here, where launcher diameter is approximately 20λ and the helical cut length is approximately 100λ, the geometric optics model provides enough accuracy to warrant its use in the preliminary design of the converter.

The geometric optics model of waveguide modes can be derived by starting with the equations for the unperturbed modes of a cylindrical waveguide. The fields of $TE_{m,p}$ waves travelling in the $+\hat{z}$ direction can be written in cylindrical coordinates as

$$\mathbf{H} = H_0 e^{i(k_z z \pm m\phi - \omega t)} \left[\frac{ik_z}{k_r} J'_m(k_r r)\hat{r} \mp \frac{mk_z}{k_r^2 r} J_m(k_r r)\hat{\phi} + J_m(k_r r)\hat{z} \right] \tag{2.1}$$

$$\mathbf{E} = \eta_0 H_0 e^{i(k_z z \pm m\phi - \omega t)} \left[\mp \frac{mk}{k_r^2 r} J_m(k_r r)\hat{r} - \frac{ik}{k_r} J'_m(k_r r)\hat{\phi} \right], \tag{2.2}$$

where the upper and lower signs refer to the right-handed and left-handed azimuthal rotations, respectively. In Eqs. 2.1 and 2.2 $k = \frac{\omega}{c}$, where ω is the angular frequency of the

wave and c is the speed of light; $k_r = \frac{\nu_{mp}}{R_w}$, where ν_{mp} is the p^{th} zero of $J'_m(x)$ and R_w is the waveguide radius; $k_z = \sqrt{k^2 - k_r^2}$; and η_0 is the free space wave impedance.

Through a decomposition of the Bessel functions, the waveguide fields can be represented as superpositions of plane waves [17]. The Bessel function can be written in integral form according to Eq. 2.3.

$$J_m(x) = \frac{1}{\pi} \int_0^{\pi} \cos(x \sin\theta - m\theta)\, d\theta \tag{2.3}$$

Using the following equivalence

$$\frac{2m}{x} J_m(x) = J_{m-1}(x) + J_{m+1}(x) \tag{2.4}$$

and substituting in the integral representation from Eq. 2.3 gives

$$\frac{2m}{x} J_m(x) = \frac{1}{\pi} \int_0^{\pi} \{\cos[x \sin\theta - (m-1)\theta] + \cos[x \sin\theta - (m+1)\theta]\}\, d\theta$$

$$= \frac{1}{\pi} \int_0^{\pi} 2\cos\theta \cos(x \sin\theta - m\theta)\, d\theta. \tag{2.5}$$

Because the integral is symmetric about π, Eq. 2.5 can be rewritten as

$$\frac{2m}{x} J_m(x) = \frac{1}{\pi} \int_0^{2\pi} \cos\theta \cos(x \sin\theta - m\theta)\, d\theta. \tag{2.6}$$

Using the identity $\int_0^{2\pi} \cos\theta \sin(x \sin\theta - m\theta)\, d\theta = 0$, Eq. 2.7 follows directly from Eq. 2.6.

$$\frac{m}{x} J_m(x) = \frac{1}{2\pi} \int_0^{2\pi} \cos\theta e^{i(x \sin\theta - m\theta)} d\theta \tag{2.7}$$

The equivalence given in Eq. 2.8 is then used to find the integral representation of the Bessel function derivative, $J'_m(x)$.

$$J'_m(x) = J_{m-1}(x) - J_{m+1}(x) \tag{2.8}$$

Following a method similar to that detailed in Eqs. 2.3–2.7 gives

$$J'_m(x) = -\frac{i}{\pi}\int_0^{2\pi} \sin\theta e^{i(x\sin\theta - m\theta)}d\theta. \tag{2.9}$$

Substituting Eqs. 2.7 and 2.9 into Eq. 2.2 for the right rotating cylindrical waveguide mode gives

$$E_r = -\frac{\eta_0 H_0 k}{2\pi k_r}\int_0^{2\pi} d\theta \cos\theta e^{i(-\omega t + k_z z + k_r r\sin\theta + m(\phi-\theta))} \tag{2.10}$$

$$E_\phi = -\frac{\eta_0 H_0 k}{\pi k_r}\int_0^{2\pi} d\theta \sin\theta e^{i(-\omega t + k_z z + k_r r\sin\theta + m(\phi-\theta))} \tag{2.11}$$

Thus, with Eqs. 2.10 and 2.11, the electric fields of the right rotating $TE_{m,p}$ cylindrical waveguide mode are represented as a continuum of plane waves of the form

$$E \propto e^{i(kS(\mathbf{r})-\omega t)}, \tag{2.12}$$

where the eikonal, $S(\mathbf{r})$, is

$$S(\mathbf{r}) = \frac{1}{k}\left(k_z z + k_r r\sin\theta + m(\phi-\theta)\right). \tag{2.13}$$

Following [17] and [18], the eikonal equation

$$\begin{aligned} |\nabla S|^2 &= \left(\frac{\partial S}{\partial r}\right)^2 + \frac{1}{r^2}\left(\frac{\partial S}{\partial \phi}\right)^2 + \left(\frac{\partial S}{\partial z}\right)^2 = 1 \\ &= \frac{1}{k^2}\left(k_z^2 + k_r^2\sin^2\theta + \frac{m^2}{r^2}\right) = 1 \end{aligned} \tag{2.14}$$

can be solved to give an intuitive picture of the propagation paths of these plane waves, or rays. The direction of the rays is given by ∇S [18]. Solving Eq. 2.14 for θ gives

$$k^2 - k_z^2 = k_r^2 = k_r^2\sin^2\theta + \frac{m^2}{r^2} \tag{2.15a}$$

$$1 = \sin^2\theta + \frac{m^2}{r^2 k_r^2} \tag{2.15b}$$

$$\theta(r) = \cos^{-1}\left(\frac{m}{r}\frac{R_w}{\nu_{mp}}\right) \tag{2.15c}$$

At $r = R_w$,

$$\theta = \cos^{-1}\left(\frac{m}{\nu_{mp}}\right) = \alpha, \tag{2.15d}$$

where α is the azimuthal bounce angle of the rays at the waveguide wall. Rays that reflect at this angle are tangent to a caustic surface at R_c, where

$$R_c = R_w\frac{m}{\nu_{mp}}. \tag{2.16}$$

Figure 2.1 shows the rays travelling with azimuthal bounce angle α and helical pitch angle θ_B, where $\tan\theta_B = \frac{k_r}{k_z}$. The caustic radius, R_c, also has significance in the field representation of the waveguide mode (Eqs. 2.1 and 2.2); for $r > R_c$ the fields are oscillatory and for $r < R_c$ the fields are exponentially decaying.

Thus, in the geometric optics limit, the flow of energy in a cylindrical waveguide mode can be represented by a set of rays travelling tangent to a caustic surface with an azimuthal bounce angle α and a helical pitch angle θ_B. A Vlasov-type antenna launches the spiraling rays through a one turn helical cut in the waveguide wall, the cut following the trajectories of the rays in the guide. The length of the cut, L, is found by equating the energy flux through the waveguide cross section to the energy flux through the rectangular aperture of width R_w and length L [11], which is shown in Fig. 2.2.

$$L = L_B\frac{(\nu_{mp}^2 - m^2)}{\nu_{mp}}\frac{J_m^2(\nu_{mp})}{1 - J_0^2(\nu_{mp}) + J_m^2(\nu_{mp}) - 2\sum_{k=1}^{m} J_k^2(\nu_{mp})}, \tag{2.17}$$

where L_B, the bounce length, is given by Eq. 2.18.

$$L_B = 2\pi R_w\left(\frac{k_z}{k_r}\right) \tag{2.18}$$

An alternative approach to finding the appropriate helical cut length is based on a correction to the bounce length [8]. In the limit where $R_c \to R_w$, $\alpha \to 0$ and the rays travel along the waveguide wall. In this case, the one turn azimuthal path length is equal to the circumference of the waveguide, $2\pi R_w$, and the bounce length, L_B, is equal the one turn axial path length of a ray, L'. In the realistic case, when $R_c < R_w$ and the rays travel in chords from one point on the waveguide wall to the next (Fig. 2.1), the azimuthal path

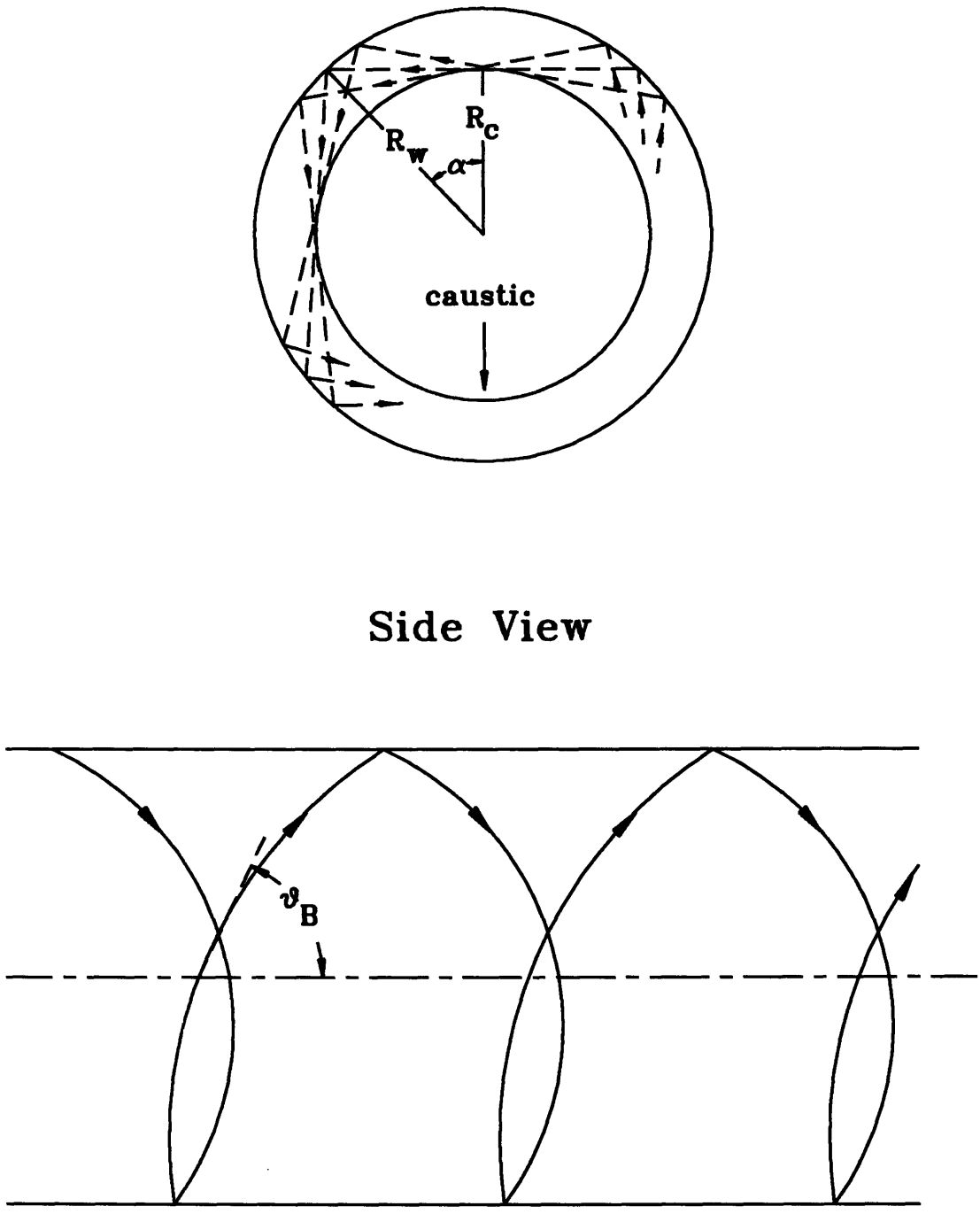

Figure 2.1 Geometric optics view of cylindrical waveguide modes showing rays travelling tangent to a caustic with radius R_c. The rays travel with an azimuthal bounce angle α and a helical pitch angle θ_B.

length of the ray is less than the waveguide circumference and the bounce length no longer equals the one turn axial path length, L'. The corrected cut length, L', is the bounce length multiplied by the ratio of the chord length to the arc length for one chord

$$L' = L_B \frac{\sin \alpha}{\alpha}, \tag{2.19}$$

where α is the azimuthal bounce angle defined above. Although L' and L are not equal, they are numerically equivalent to within 0.1% for a wide range of modes [11].

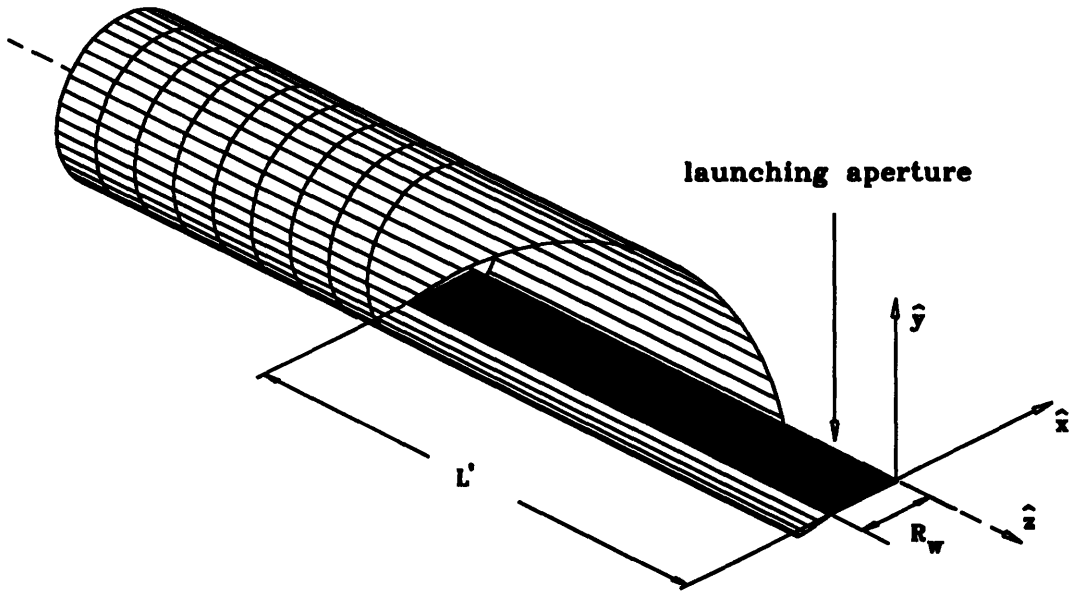

Figure 2.2 The Vlasov-type launcher with the rectangular launching aperture and coordinate system indicated.

Thus, if a one turn helix of length L (or L') is cut from the waveguide, the radiation, which is concentrated in the region between the helix and the straight edge, will launch from the straight edge. The rays radiate from the cut in an azimuthal range limited to 2α and at polar bounce angle θ_B relative to the waveguide axis. The direction of the helical cut fixes the launcher applicability to either left-hand or right-hand rotating modes. Generally, gyrotrons produce radiation of only one rotation, depending on the radial position of the electron beam. A further investigation of competing counter rotating modes can be found in Chapter 4.

The last step in the design of the Vlasov-type mode converter is the calculation of a reflector surface to provide focussing and profile shaping for the launched beam. In the geometric optics limit, the radiating source is a segment of the caustic surface bounded in azimuth by the angle 2α and in length by the straight cut, L. The reflector satisfies the condition given in Eq. 2.20, which requires that all rays leaving the caustic arrive in phase at the focus, which is a single point in the ray optics approximation [19].

$$m\phi + k_z z_c + kd_1 + kd_2 = C, \tag{2.20}$$

where $m\phi + k_z z_c$ is the phase of the ray on the radiating caustic surface, d_1 is the distance a ray travels from the caustic to the reflector, and d_2 is the distance a ray travels from the reflector to the focus. The constant in Eq. 2.20, C, is determined by the location of the reflector relative to the launcher and focus. Equation 2.20 is solved for each launched ray and a reflector surface is generated.

The geometric optics description of cylindrical waveguide modes was employed in an effort to simplify the design of the Vlasov-type launcher and focussing reflector. Additionally, vector diffraction theory was used to simulate the operation of the converter and to verify the geometric optics design. The predictions of the two theories will be compared and the validity of the ray optics approximation will be discussed in Section 2.4.

2.2 Vector Diffraction Theory

The vector diffraction theory used to simulate the operation of the Vlasov-type mode converter consists of three parts. First, the near field radiation pattern of the launcher is calculated. With this information, the fields on the doubly curved reflector are found. Next, the resultant surface currents on the reflector are determined. Finally, the surface currents are re-radiated and the near field radiation pattern on an observation plane of interest is found.

There are two methods for calculating the near field radiation pattern of the launcher. The problem can be solved by using wall currents as a radiating source or by using an aperture field integration method. In the case of the Vlasov-type launcher, the aperture field method is the simpler approach because the integration can be reduced from three to two spatial dimensions. The Stratton-Chu formula [20], which is a vector formulation of Huygens' principle, is appropriate for the specified aperture integration and near field calculation. With the Stratton-Chu formula, the fields at an observation point are calculated by integrating the response to the point source Green's function over all source regions, with the source points weighted by the amplitude and phase of the fields on the aperture.

The source aperture under consideration is the rectangular plane bounded by the waveguide axis, the straight cut length L, and the two segments radially connecting them (Fig. 2.2). The fields on this aperture are assumed to be the unperturbed waveguide fields, described in Eqs. 2.1 and 2.2. The unit normal, $\hat{n}$, is in the direction marked $\hat{y}$ in Fig. 2.2. The **E** and **H** fields at an observation point, **r**, are given by [20]

$$\mathbf{E}(\mathbf{r}) = \oint_{S'} dS' \left\{ i\omega\mu[\hat{\mathbf{n}} \times \mathbf{H}(\mathbf{r}')]g(\mathbf{r},\mathbf{r}') + [\hat{\mathbf{n}} \cdot \mathbf{E}(\mathbf{r}')]\nabla' g(\mathbf{r},\mathbf{r}') + [\hat{\mathbf{n}} \times \mathbf{E}(\mathbf{r}')] \times \nabla' g(\mathbf{r},\mathbf{r}') \right\} \tag{2.21}$$

$$\mathbf{H}(\mathbf{r}) = \oint_{S'} dS' \left\{ -i\omega\epsilon[\hat{\mathbf{n}} \times \mathbf{E}(\mathbf{r}')]g(\mathbf{r},\mathbf{r}') + [\hat{\mathbf{n}} \cdot \mathbf{H}(\mathbf{r}')]\nabla' g(\mathbf{r},\mathbf{r}') + [\hat{\mathbf{n}} \times \mathbf{H}(\mathbf{r}')] \times \nabla' g(\mathbf{r},\mathbf{r}') \right\} \tag{2.22}$$

In Eqs. 2.21 and 2.22, μ is the permeability, ϵ is the permittivity, and $g(\mathbf{r},\mathbf{r}')$ is the point source Green's function, defined by

$$g(\mathbf{r},\mathbf{r}') = \frac{e^{i\mathbf{k}\cdot\mathbf{R}}}{R}, \tag{2.23}$$

where $R = |\mathbf{r} - \mathbf{r}'|$ is the distance between the observation point and the source point. The primed variables indicate a source point and the unprimed indicate an observation point.

Unfortunately, the Stratton-Chu formula (Eqs. 2.21 and 2.22) yields two dimensional integrals that can not be solved in closed form for the case under consideration. A computer code was written to numerically integrate $TE_{m,p}$ cylindrical waveguide modes over the launcher aperture.

Using the computer code to solve the Stratton-Chu equation, the near field launcher pattern can be calculated at any point of interest or, more specifically, on the surface of the doubly curved reflector. Once again, the near field pattern reflected from the mirror can be

calculated by either a field aperture method or a current source method. In this case, where the reflector is not a plane but a three dimensional grid of points, the current source method proves to be more tractable than the field integration method.

In order to compute the currents on the reflector surface from the fields calculated with the Stratton-Chu equation, the physical optics approximation is used. The physical optics current, given by Eq. 2.24, is rigorously correct for a reflector that is perfectly conducting, perfectly flat, and infinite in extent. The physical optics approximation is justified for the case under consideration, where the smallest dimension of the copper reflector is approximately 60 wavelengths and the curvature is slight.

$$\mathbf{J_s} = 2(\hat{\mathbf{n}} \times \mathbf{H}) \tag{2.24}$$

The surface currents on the reflector, calculated with Eqs. 2.22 and 2.24, can be re-radiated and the resultant fields computed at a near field observation point according to Eqs. 2.25 and 2.26 [21].

$$\mathbf{E} = \frac{i}{4\pi\omega\epsilon}\int_{S'}[(\mathbf{J_s}\cdot\nabla')\nabla' + k^2\mathbf{J_s}]\frac{e^{i\mathbf{k}\cdot\mathbf{R}}}{R}dS' \tag{2.25}$$

$$\mathbf{H} = \frac{1}{4\pi}\int_{S'}(\mathbf{J_s}\times\nabla')\frac{e^{i\mathbf{k}\cdot\mathbf{R}}}{R}dS' \tag{2.26}$$

Once again, the current source integrals in Eqs. 2.25 and 2.26 do not have closed form solutions, so a second computer code was written to perform the integrations and calculate the resulting near field pattern.

Thus, using the Stratton-Chu vector diffraction formula (Eqs. 2.21 and 2.22), the near field launcher pattern can be calculated on the doubly curved focussing reflector. The physical optics approximation (Eq. 2.24) is then used to solve for the resultant surface currents, which can be re-radiated according to Eqs. 2.25 and 2.26. In this way, the Vlasov-type converter, which was designed with geometric optics theory, can be modelled with a vector diffraction theory and the two results can be compared.

2.3 Vlasov-Type Converter Experiments and Results

A Vlasov-type converter was designed to transform the $TE_{16,2}$ cylindrical waveguide mode at 146 GHz to a Gaussian-like beam in free space. The design parameters of the converter are summarized in Table 2.1. The shape of the doubly curved reflector was calculated according to Eq. 2.20 and the launcher and reflector were constructed. The experimental verification of the converter is described below.

input mode	$TE_{16,2}$
frequency	146 GHz
waveguide radius, R_w	1.746 cm
launcher length, L	20.8 cm
polar bounce angle, θ_B	25.8°
azimuthal expansion angle, 2α	93°
⊥ distance from wg axis to mirror center, $r_\perp$	3.81 cm
⊥ distance from wg axis to focus, $r_{f\perp}$	25.4 cm

Table 2.1 Design parameters of the $TE_{16,2}$ Vlasov-type converter.

2.3.1 Converter Test Apparatus

A megawatt power level, 3 μsec pulsed gyrotron oscillator operating in the $TE_{16,2}$ mode at 146 GHz [5] [22] was the radiation source used in converter tests. The output port of the gyrotron is comprised of several parts. Inside the vacuum tube, there is a cylindrical waveguide, R_w = 1.746 cm. The internal waveguide extends to within a few millimeters of a quartz vacuum window, which is 0.025 cm thick. An external waveguide, or sleeve, is positioned on the atmosphere side of the vacuum window and held in place with a collar. The sleeve, on which the launcher is mounted, is also a cylindrical waveguide with radius R_w = 1.746 cm, and it is designed as an external continuation of the gyrotron collector. A schematic of the gyrotron output port and Vlasov-type launcher is shown in Fig. 2.3.

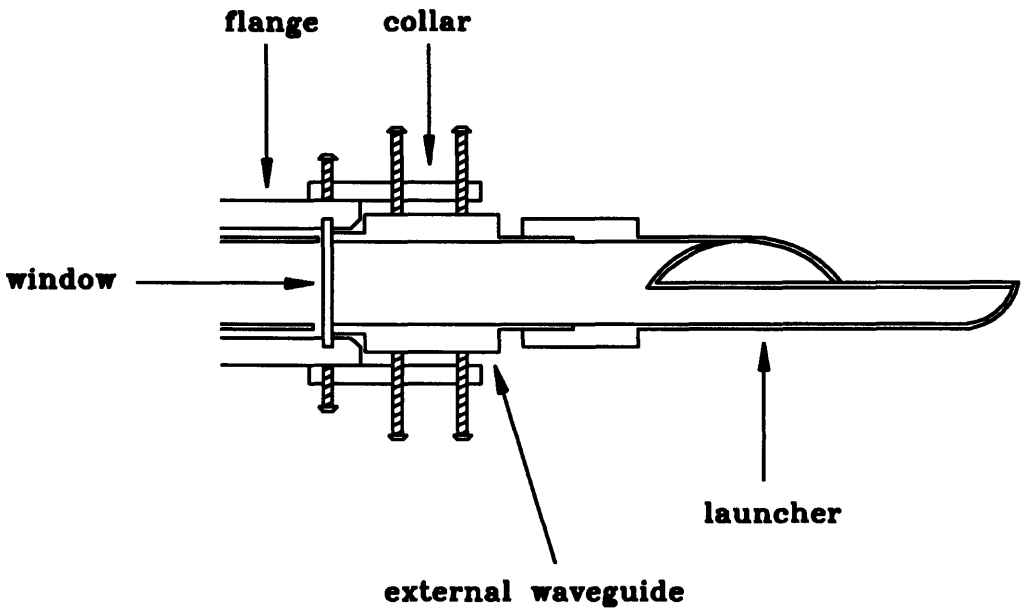

Figure 2.3 Schematic of the Vlasov-type launcher mounted on the gyrotron output port.

The vacuum window automatically produces a discontinuity in the waveguide, although the external waveguide section is carefully aligned to minimize the mode conversion caused by the disruption.

Several experiments were performed to determine the mode purity of the radiation incident on the converter and to assess the converter performance. The experiments, described below, include radiation pattern measurements as well as calorimetric efficiency measurements.

2.3.2 Mode Purity Measurements

First, far field polar pattern scans were made to determine the mode content of the radiation leaving the gyrotron. The polar scan measurement apparatus is shown in Fig. 2.4. A WR6 21 dB pyramidal horn, a calibrated attenuator, and a WR6 diode detector formed the receiving unit. This unit was mounted on a platform, which was rotated along the polar angle ($\hat{\theta}$) at a constant radius of 79 cm, with the pivot point directly beneath the end of the launching waveguide. Measurements were made by adjusting the variable attenuator to keep the diode signal at a constant level. In this way, the V–I characteristics of the diode did

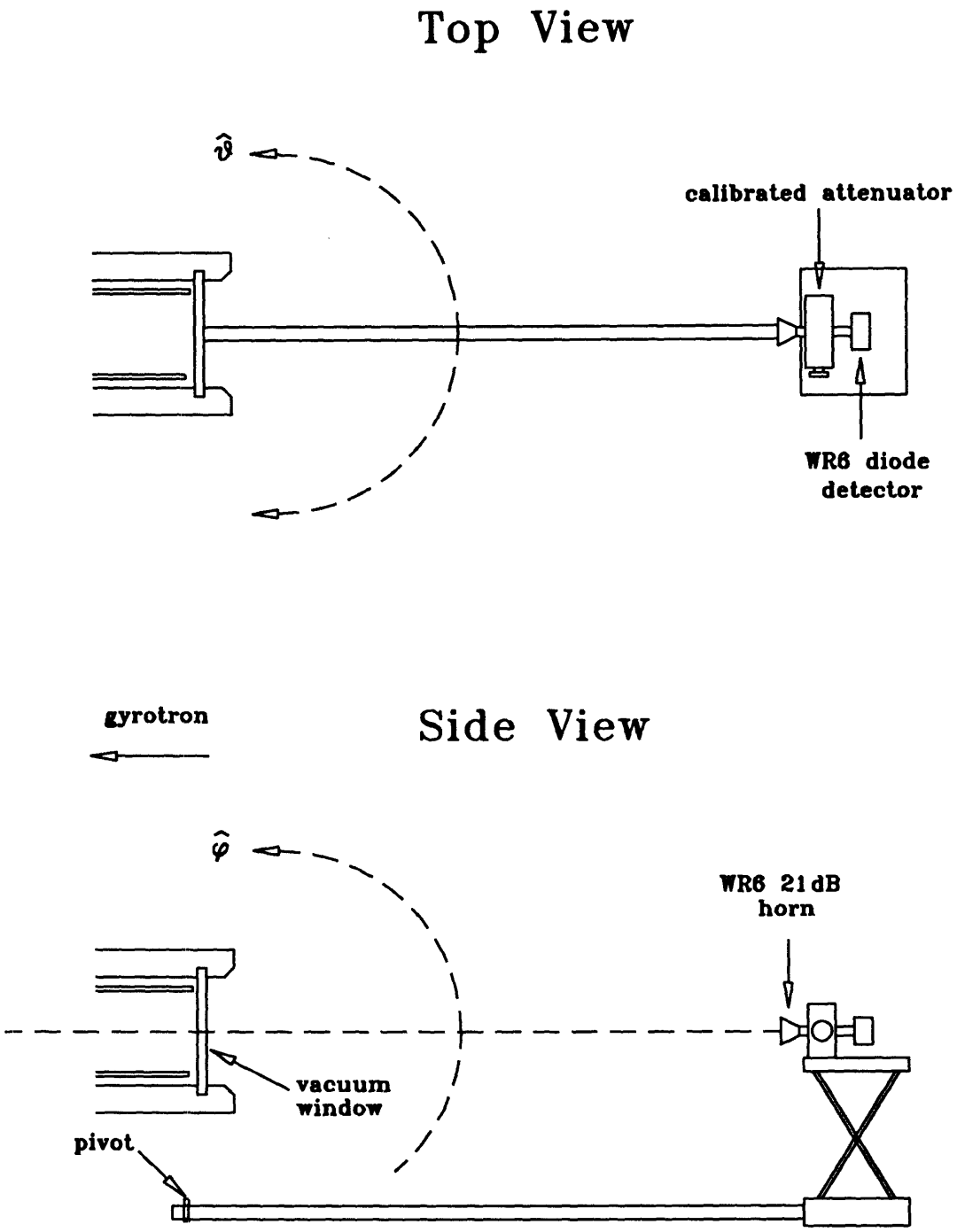

Figure 2.4 Schematic of the polar scan measurement apparatus.

not enter into the measurement. In the experiment, the horn was mounted in the orientation for detecting E_ϕ, which is the dominant component of the far field radiation pattern for the $TE_{16,2}$ and neighboring modes.

Figure 2.5 shows the results of the E_ϕ polar scan of the gyrotron radiation pattern. The measured values of $|E_\phi|^2$, plotted in dB below peak intensity, are indicated by x's. The best fit to the experimental data was found by assuming a mode mix of 0.3% $TE_{16,1}$, 99.0% $TE_{16,2}$, 0.3% $TE_{16,3}$, and 0.4% $TE_{17,2}$, all at 146 GHz. The solid line in Fig. 2.5 shows theoretical far field pattern for this mix of modes.

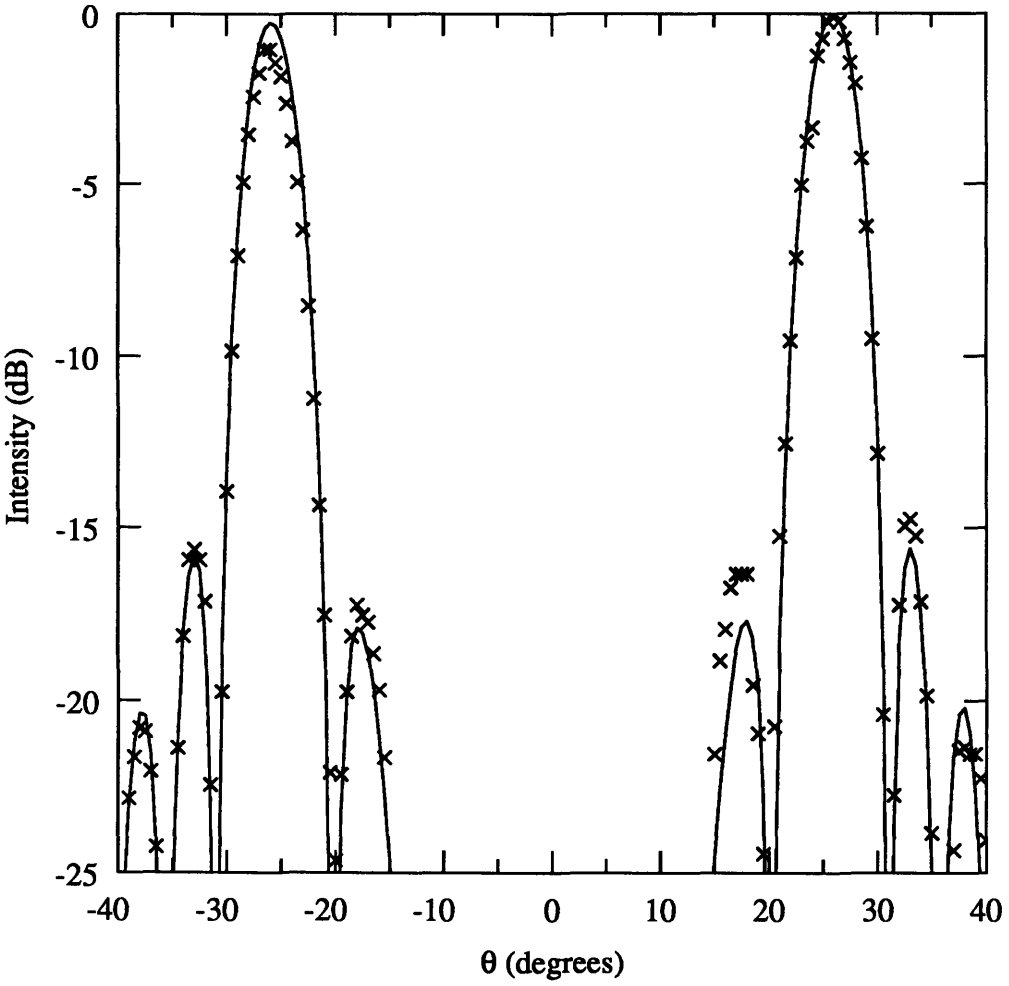

Figure 2.5 Far field polar radiation pattern scan of power exiting the gyrotron directly. The x's represent measured values of $|E_\phi|^2$. The solid line shows the theoretical far field pattern for the mode mix of 0.3% $TE_{16,1}$, 99.0% $TE_{16,2}$, 0.3% $TE_{16,3}$, and 0.4% $TE_{17,2}$.

Thus, the polar scan indicates that the gyrotron operates in the $TE_{16,2}$ mode with approximately 99% mode purity. The small amounts of neighboring azimuthal and radial modes are due to mode conversion after the cavity, most likely in the cavity output taper or at the cavity/collector joint.

Next, the external waveguide, or sleeve, was mounted on the gyrotron window flange (Fig. 2.3). The sleeve was carefully aligned in order to minimize mode conversion from the desired $TE_{16,2}$ mode. Another far field polar scan was made, and the results are shown in Fig. 2.6.

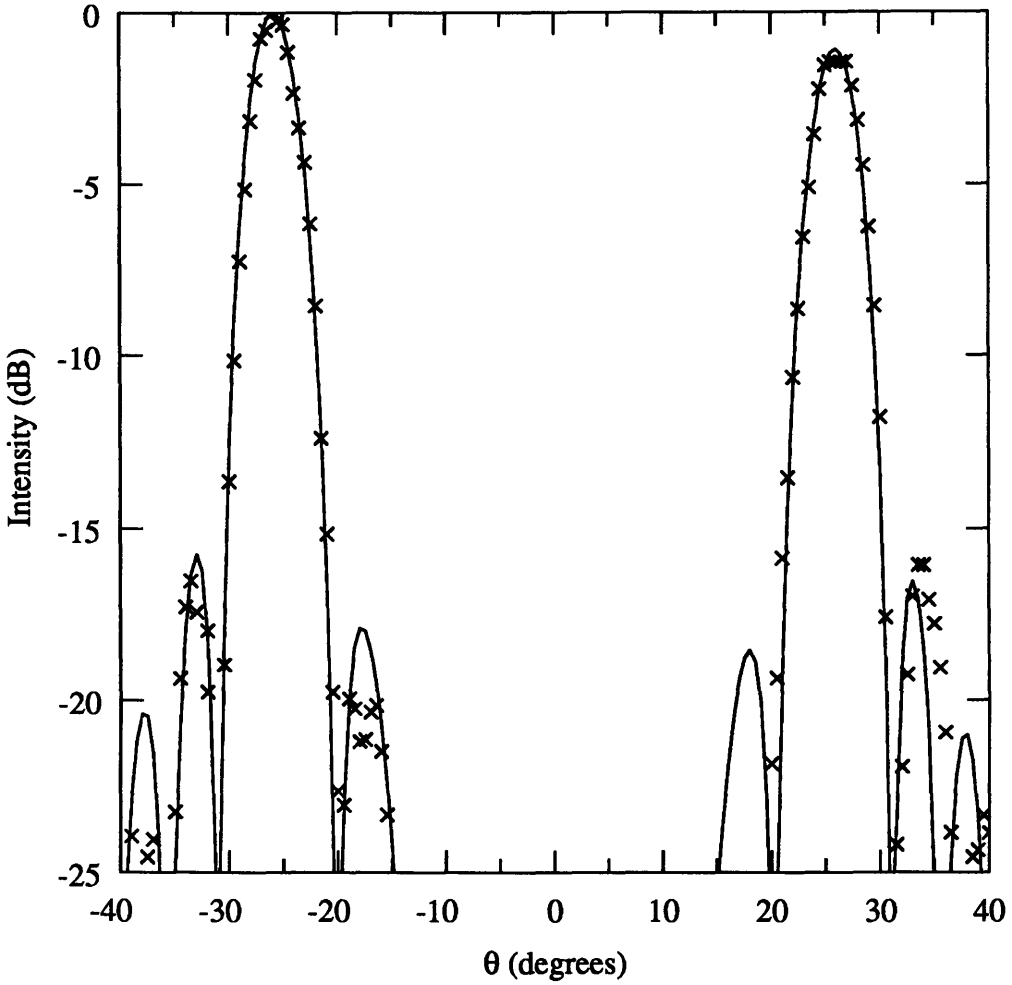

Figure 2.6 Far field polar radiation pattern scan of power exiting the sleeve. The x's represent measured values of $|E_\phi|^2$. The solid line shows the theoretical far field pattern for the mode mix of 0.3% $TE_{16,1}$, 97.2% $TE_{16,2}$, 0.3% $TE_{16,3}$, 1.6% $TE_{15,2}$, and 0.6% $TE_{17,2}$.

Once again, the experimental data points are indicated by x's. The best fit to the data was found by assuming a mode mix with the following power break down: 0.3% $TE_{16,1}$, 97.2% $TE_{16,2}$, 0.3% $TE_{16,3}$, 1.6% $TE_{15,1}$, and 0.6% $TE_{17,2}$. The theoretical far field pattern for this mix is shown by the solid line in Fig. 2.6. The additional mode conversion from the $TE_{16,2}$ to the adjacent modes is most likely caused by a slight tilt or offset of the external waveguide relative to the gyrotron collector. The polar scan of the radiation from the sleeve indicates that $> 97\%$ of the power at the sleeve output, which is the power incident on the launcher, is in the $TE_{16,2}$ mode, with approximately 3% in other modes. With this information, the performance of the converter can be experimentally evaluated.

2.3.3 Near Field Launcher Pattern Measurements

After the mode mix at the output of the sleeve was determined through the far field polar scans described above, the Vlasov-type launcher was positioned on the sleeve and the near field radiation pattern was measured. The scans were made by rotating the launcher in the azimuthal ($\hat{\phi}$) direction while sliding the receiving unit along a platform running parallel to the launcher straight edge. In this way, the near field pattern on a cylinder concentric with the waveguide was obtained. The scan was made at $r_\perp$ = 4.25 cm, near the position of the doubly curved reflector. For this experiment an open ended WR6 waveguide was used rather than the pyramidal horn used in the polar scan experiments. The receiving unit was rotated by an angle θ_B to be perpendicular to the incoming rays. The detector was oriented to measure the $\hat{\phi}$ component of E. The experimental apparatus for measuring the near field launcher pattern is shown in Fig. 2.7.

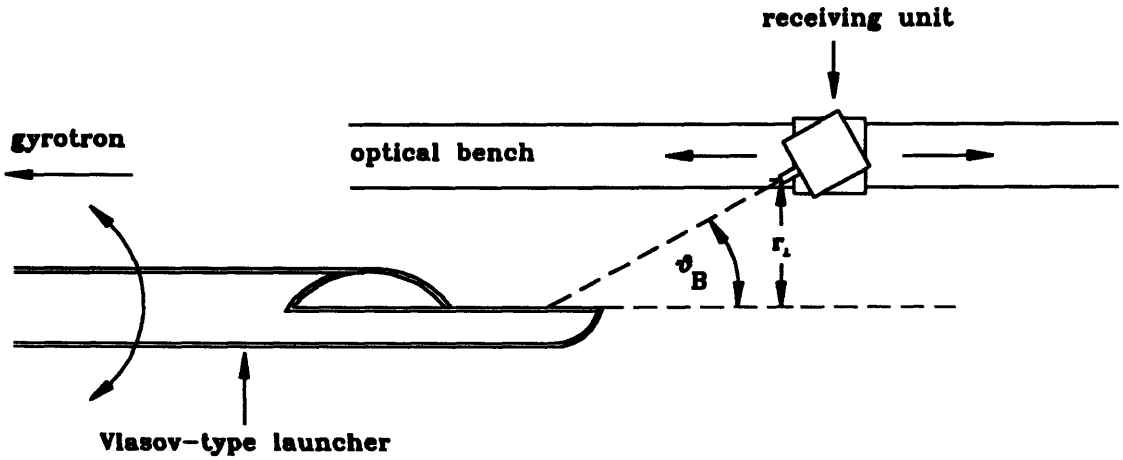

Figure 2.7 Experimental apparatus for measuring near field $\hat{\phi} - \hat{z}$ patterns from the Vlasov-type launcher.

The results of the near field $\hat{\phi} - \hat{z}$ scan are shown in Fig. 2.8. The figure shows lines of constant $|E_\phi|^2$, plotted in dB below peak intensity. The boundary of the focussing reflector is indicated. A piece-wise integration of the experimental pattern shows that > 97% of the E_ϕ radiation from the launcher is intercepted by the doubly curved reflector.

The experimental result (Fig. 2.8) can be compared to the near field diffraction theory prediction for a mode mix of 0.3% $TE_{16,1}$, 97.2% $TE_{16,2}$, 0.3% $TE_{16,3}$, 1.6% $TE_{15,2}$, and 0.6% $TE_{17,2}$, which is shown in Fig. 2.9.

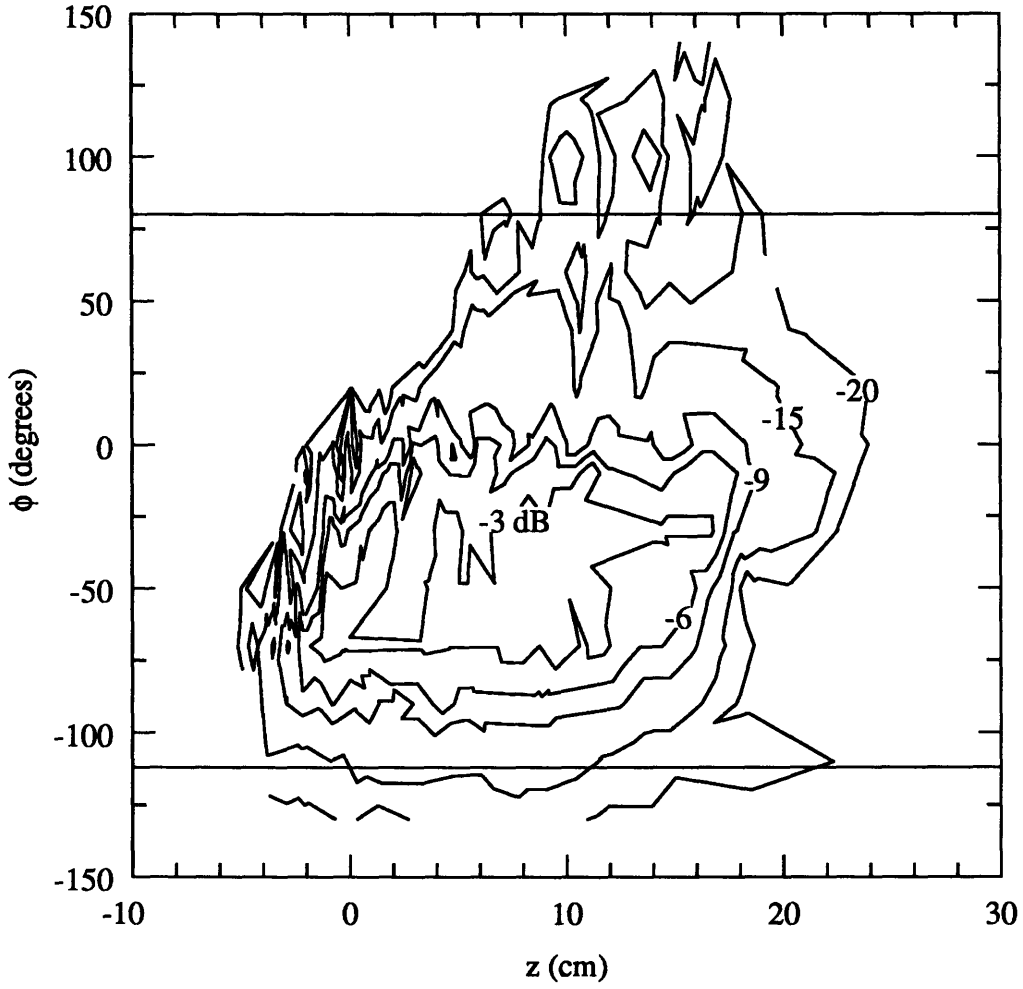

Figure 2.8 Experimental near field launcher pattern taken at the reflector position. Lines of constant $|E_\phi|^2$ are shown in dB below peak intensity. The boundary of the doubly curved reflector is indicated.

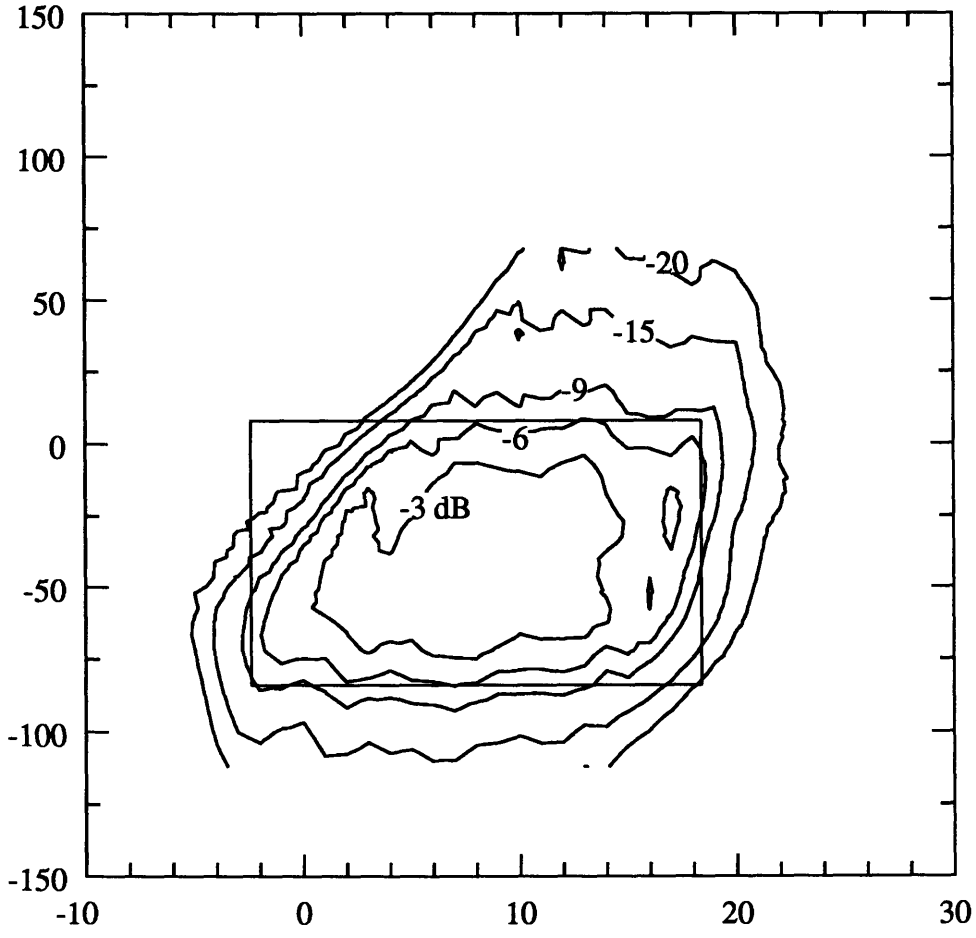

Figure 2.9 Theoretical near field launcher pattern at the reflector position, as predicted by the Stratton-Chu formula, for the mode mix of 0.3% $TE_{16,1}$, 97.2% $TE_{16,2}$, 0.3% $TE_{16,3}$, 1.6% $TE_{15,2}$, and 0.6% $TE_{17,2}$. Lines of constant $|E_\phi|^2$ are shown in dB below peak intensity. The boundary for the pattern predicted by geometric optics is indicated.

The size and shape of the experimental (Fig. 2.8) and theoretical (Fig. 2.9) patterns are in good agreement. The slight differences at levels below -15 dB are most likely due to edge diffraction effects. The vector diffraction theory assumes the unperturbed waveguide fields (Eqs. 2.1 and 2.2) over the aperture, and does not include the effects of the interrupted wall currents.

Figure 2.9 also shows the boundary for the pattern predicted by geometric optics theory. As described in Section 2.1, the geometric optics pattern subtends an angle $2\alpha = 93^{o}$ in azimuth and extends $L = 20.8$ cm in the axial dimension. It is immediately apparent that the geometric optics theory generates a near field pattern which is significantly smaller than either the diffraction theory prediction or experimentally determined pattern. In fact, the diffraction theory shows that the mirror must subtend 4α degrees in order to intercept all the radiation from the launcher. A piece-wise integration of the diffraction theory pattern indicates that approximately 75% of the power falls within the geometric optics extents. For this reason, in designing the doubly curved reflector, the size is determined using diffraction theory, while the shape is calculated with the geometric optics approximation (Eq. 2.20). To extend the mirror beyond the geometric optics limits, the radiating caustic source is extended to 4α in the azimuthal direction. The mirror surface, determined by Eq. 2.20, is, thus, shaped to focus the additional, non-geometric optics rays as if they came through the waveguide wall, which is non-physical. It is expected that the radiation that falls outside the geometric optics limits will be directed to the focal plane, but will most likely arrive at the focus with phase errors due to the improper shaping at the edges of the extended reflector. However, the goal of the experiments described here was to verify the vector diffraction theory and to design a reflector that was large enough to direct $> 95\%$ of the radiated power to the focal plane. The extended geometric optics mirror is adequate for these purposes.

2.3.4 Output Beam Measurements

Once the performance of the launcher was experimentally verified, the operation of the full converter, consisting of the launcher and reflector, was investigated. The doubly curved reflector, which intercepts the launched rays and directs them to a focus in the far field, was placed at its design position and a diode scan was made in a plane slightly beyond the focal point. For this scan, the open ended WR6 waveguide, the precision attenuator, and the diode detector formed the receiving unit. An optical bench was mounted perpendicular to the incoming rays and the detector was moved vertically and horizontally. The experimental apparatus for the focal plane scans is shown in Fig. 2.10. Scans were taken in planes at position d, where d is the distance from the waveguide axis to the center of the pattern,

along the direction perpendicular to the beam propagation path. In this case, the detector was oriented to measure the $\hat{y}$ component of the radiation.

The experimental scan in the perpendicular plane at d = 60 cm, which is 10 cm beyond the focus at d = 50 cm, is shown in Fig. 2.11. Lines of constant $|E_y|^2$ are plotted in dB. The experimental scan shows a small, Gaussian-like focal spot in the theoretical position for the $TE_{16,2}$ mode focus, with two other foci in the theoretical positions for the $TE_{15,2}$ and $TE_{17,2}$ modes. The mode converted $TE_{15,2}$ and $TE_{17,2}$ at 146 GHz have polar bounce angles of $\theta_B = 24.5^\circ$ and $\theta_B = 27.2^\circ$, respectively. Since the $TE_{15,2}$ mode has a smaller bounce angle than the $TE_{16,2}$ mode, its focal position is at a smaller value of x than the $TE_{16,2}$ focus. Similarly, the $TE_{17,2}$ mode, which has a larger bounce angle than the $TE_{16,2}$, focuses at a larger value of x.

Performing a piece-wise power integration over the experimental E_y scan indicates that 97.8% of the total measured power is in the $TE_{16,2}$ focus, 1.6% is in the $TE_{15,2}$ focus, and 0.6% is in the $TE_{17,2}$ focus. As seen in Fig. 2.11, the beam radius at which the amplitude of the $TE_{16,2}$ focus is $\frac{1}{e}$ its on axis value, w, is 1.15 cm in the horizontal ($\hat{x}$) direction and 1.1 cm in the vertical ($\hat{y}$) direction. The peak intensity in the cross polarization, E_x, was measured to be <-20 dB from the peak of the E_y intensity.

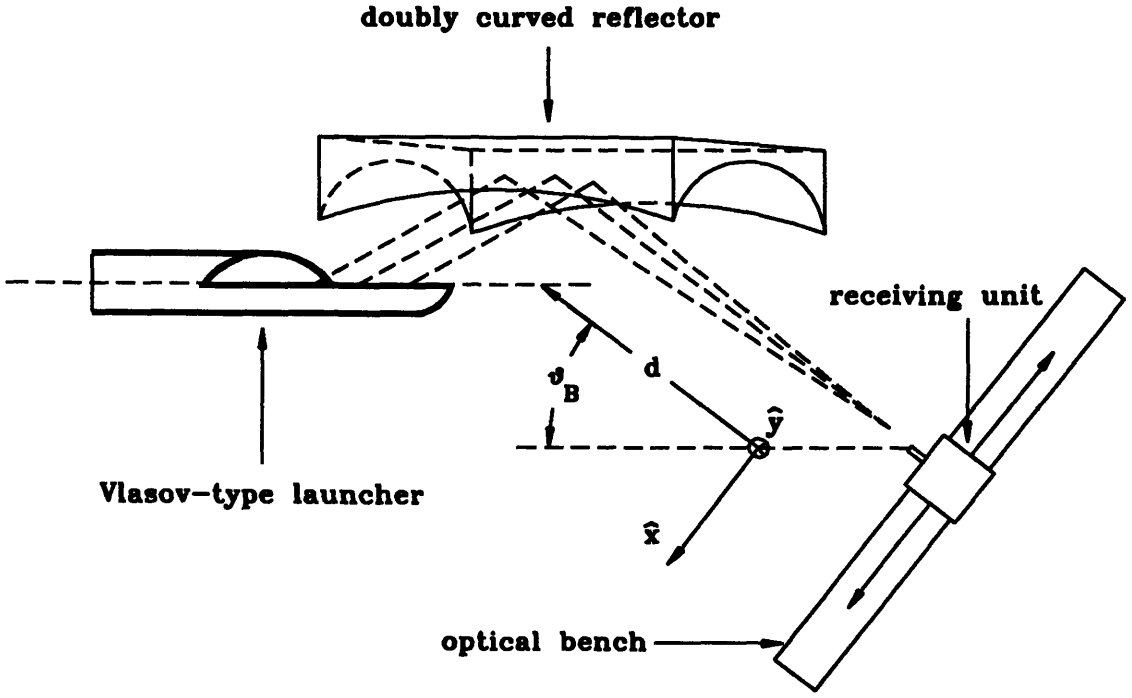

Figure 2.10 Experimental apparatus for focal plane measurements.

The experimentally determined pattern at d = 60 cm (Fig. 2.11) can be compared to the diffraction theory prediction in the same plane, which is shown in Fig. 2.12. The theoretical pattern assumes a mix of modes incident on the launcher with 97.8% of the power in the $TE_{16,2}$ mode, 1.6% in the $TE_{15,2}$ mode, and 0.6% in the $TE_{17,2}$ mode. Figs. 2.11 and 2.12 show excellent agreement between the experimental result and the diffraction theory prediction.

Next, the receiving unit was removed and a Scientech laser calorimeter, 10 cm in diameter, was placed perpendicular to the incoming rays in the d = 60 cm plane. The power in the beam was measured and normalized to the power exiting the sleeve with the mode converter removed. Calorimetric measurements showed that 95% of the power leaving the sleeve was directed to focal plane.

The measured mode mixes and power percentages at various points in the converter system are summarized in Table 2.2. The power percentages are normalized to the total power exiting the gyrotron window. Table 2.2 highlights the fact that each of the measurements described above suggests a mix of modes that is consistent with the mix indicated by the other measurements.

	$\%TE_{16,1,1}$	$\%TE_{16,2,1}$	$\%TE_{16,3,1}$	$\%TE_{15,2,1}$	$\%TE_{17,2,1}$	Total
Window	0.3	99.0	0.3	0.0	0.4	100
Sleeve	0.3	97.2	0.3	1.6	0.6	100
Reflector	0.3	94.3	0.3	1.5	0.6	97
Focus	0.0	92.9	0	1.5	0.6	95

Table 2.2 Mode mixes and power percentages at several points in the converter system.

In an effort to characterize the beam formed by the converter, diode scans, such as that shown in Fig. 2.11, were made at several values of d, and the horizontal ($\hat{x}$) and vertical ($\hat{y}$) beam radii were measured at each location. The minimum beam radii, w_{0x} = 0.8 cm and w_{0y} = 0.7 cm, were found at d = 50 cm. The measured values of horizontal and vertical beam radii versus d are shown in Figs. 2.13 and 2.14, respectively. Also plotted in Figs. 2.13 and 2.14 are the theoretical beam radii for an elliptic Gaussian beam with the measured

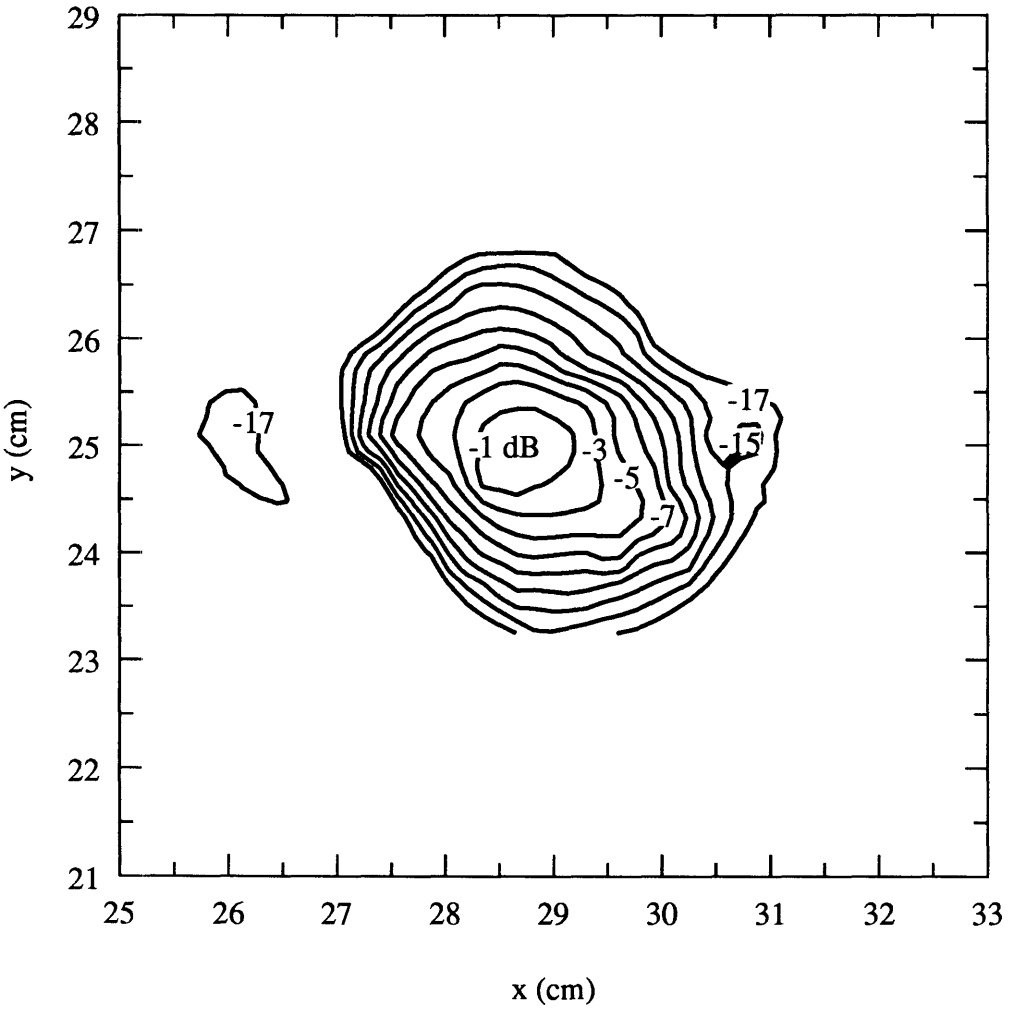

Figure 2.11 Diode scan in the plane d = 60 cm. Lines of constant $|E_y^2|$ are plotted in dB. The peak of the cross polarization, E_x, is <-21 dB from the peak of E_y.

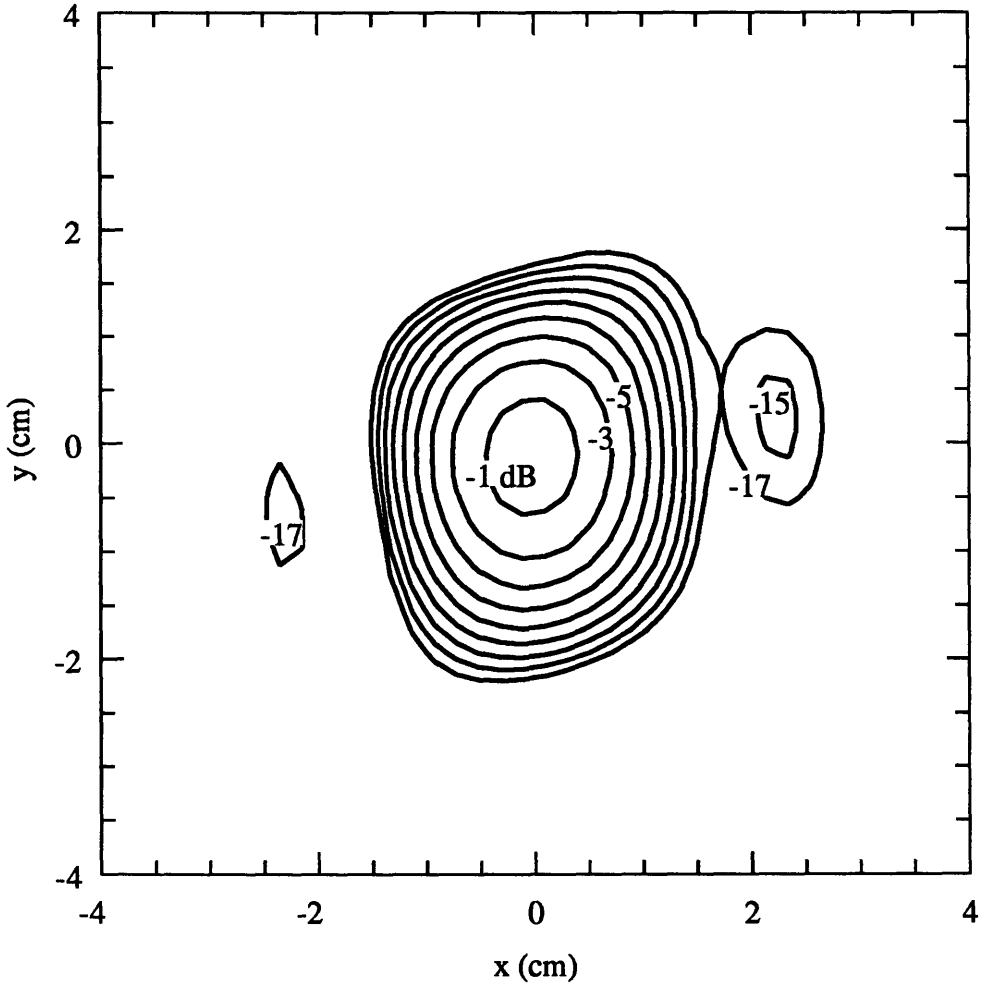

Figure 2.12 Theoretical pattern in the plane d = 60 cm for a mix of modes consisting of 97.8% $TE_{16,2}$, 1.6% $TE_{15,2}$, and 0.6% $TE_{17,2}$. Lines of constant $|E_y^2|$ are plotted in dB. The peak of the cross polarization, E_x, is <-21 dB from the peak of E_y.

beam waists, w_{0x} and w_{0y}, as well as the beam radii predicted by the Stratton-Chu diffraction theory. The radius of a Gaussian beam, w, is given by Eq. 2.27.

$$w^2(z) = w_0^2 \left[1 + \left(\frac{\lambda z}{\pi w_0^2} \right)^2 \right] \tag{2.27}$$

where λ is the wavelength and $z = 0$ is the position of the minimum beam radius, w_0.

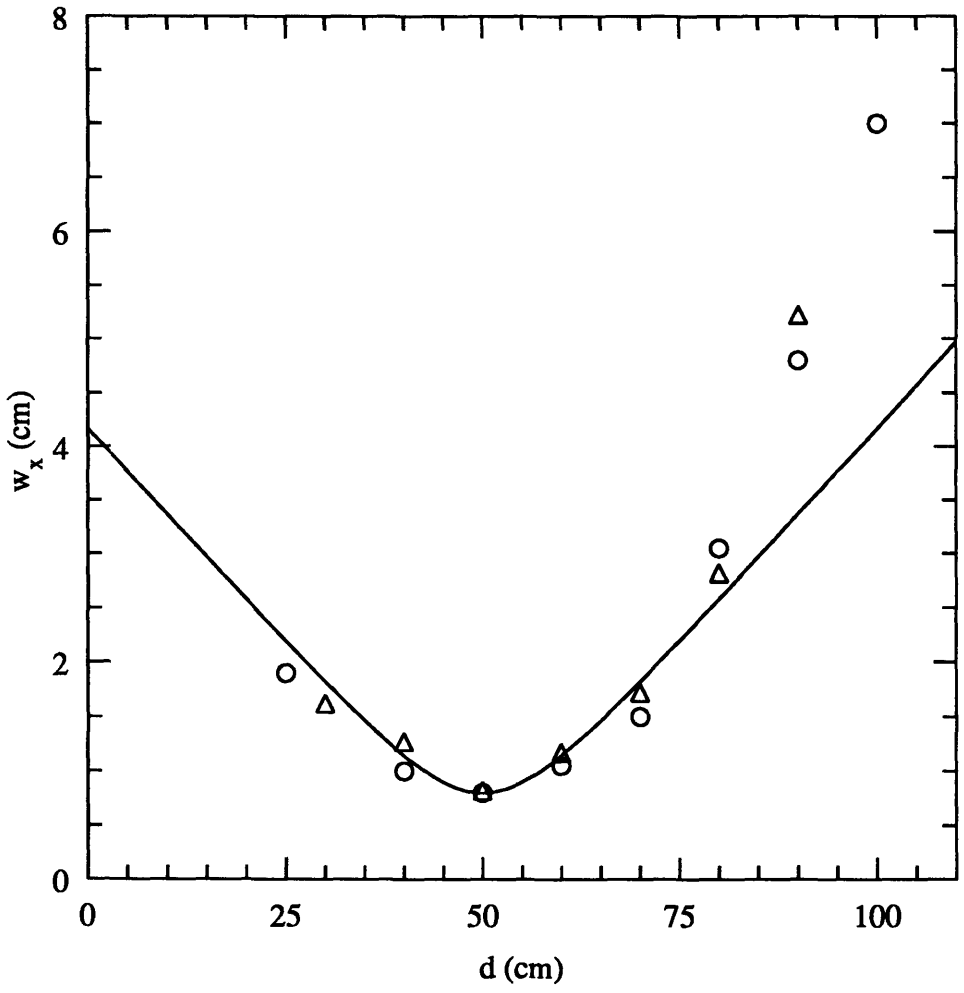

Figure 2.13 Experimental and theoretical beam radius expansion in the horizontal ($\hat{x}$) direction for the beam produced by the $TE_{16,2}$ Vlasov-type converter. The circles indicate the measured values of w_x. The triangles mark the values of w_x predicted by the vector diffraction theory. The solid line shows the theoretical beam radius for a fundamental Gaussian beam with waist $w_{0x} = 0.8$ cm at $d = 50$ cm.

As is evident in Fig. 2.13, the beam formed by the converter expands more rapidly in the horizontal direction than a fundamental Gaussian beam would, indicating non-Gaussian variations of the phase fronts. The same non-Gaussian beam expansion is predicted by the vector diffraction theory, which generates beam radii that agree well with the measured values.

Figure 2.14 shows that the measured beam expands in the vertical direction more rapidly than a fundamental Gaussian beam expands, once again indicating non-Gaussian phase fronts. The diffraction theory predicts beam radii that agree well with the measured values of w_y.

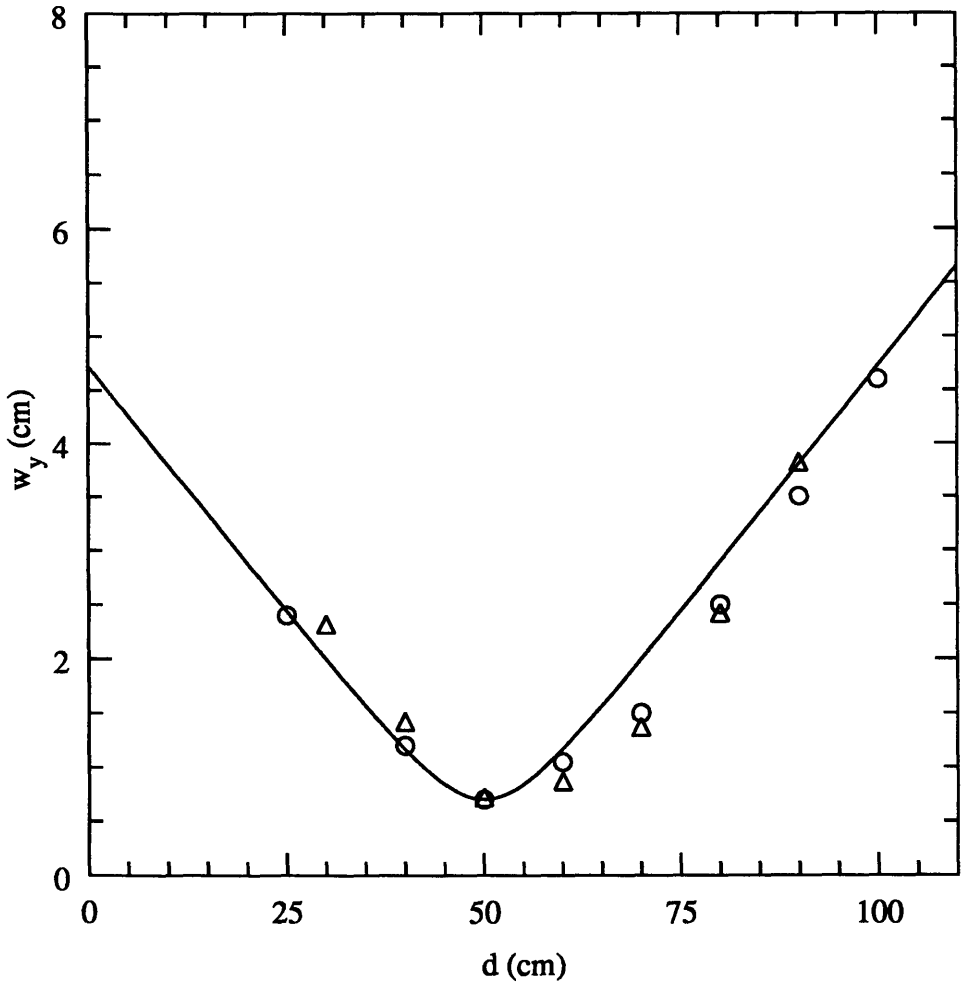

Figure 2.14 Experimental and theoretical beam radius expansion in the vertical ($\hat{y}$) direction for the beam produced by the $TE_{16,2}$ Vlasov-type converter. The circles indicate the measured values of w_y. The triangles mark the values of w_y predicted by the vector diffraction theory. The solid line shows the theoretical beam radius for a fundamental Gaussian beam with waist w_{0y} = 0.7 cm at d = 50 cm.

To determine the mode content of the beam, dot product integrations between the measured beam and a fundamental Gaussian beam were made at several points along the propagation path. The integrations suggest that approximately 88% of the power in the $TE_{16,2}$ beam was contained in the fundamental Gaussian beam mode (TEM_{00}), with 12% in higher order components. With the calculation of the mode content, the overall efficiency for converting the $TE_{16,2}$ mode to the TEM_{00} mode can be estimated by:

$$\eta_{(TE_{16,2}-TEM_{00})} = \frac{0.929\ (TE_{16,2}\text{ at focus})}{0.972\ (TE_{16,2}\text{ at sleeve exit})} \times 0.88\ TEM_{00} = 0.84 \qquad (2.28)$$

2.3.5 Corrugated Waveguide Experiments

With the beam expansion characteristics known and the percentage of TEM_{00} estimated, the final step in testing the $TE_{16,2}$ Vlasov-type converter was directing the focussed beam into a corrugated waveguide. A schematic of the experimental configuration is shown in Fig. 2.15. The waveguide line consists of two sections of 1.25 in. diameter cylindrical corrugated guide, manufactured by General Atomics. The two waveguides are joined by a 90° HE_{11} miter bend. The entrance to the line was placed at d = 50 cm, the focus of the beam formed by the Vlasov-type converter. The guide was aligned with the beam propagation direction.

A fundamental Gaussian beam with waist $w_o = 0.596 \times R_w$ couples to the HE_{11} mode in a corrugated waveguide with an efficiency >98% [23]. For the given guide, R_w = 1.25 in., the beam waist for optimum coupling is 0.9 cm. Therefore, for the beam formed by the Vlasov-type converter, it is expected that approximately 98% of beam power that is contained in a fundamental Gaussian mode would couple to the HE_{11} mode, propagate through the low loss line, and exit the guide. Thus, the total predicted efficiency can be calculated by:

$$\eta_{(TE_{16,2}-HE_{11})}(\text{calc}) = \frac{0.929\ (TE_{16,2}\text{ at focus})}{0.972\ (TE_{16,2}\text{ at sleeve exit})} \times 0.88\ TEM_{00} \times 0.98\ \eta_{coup} = 0.825 \qquad (2.29)$$

In a sense, the corrugated guide experiments provide a measure of the TEM_{00} mode content in the beam formed by the converter. Power in the fundamental Gaussian mode couples well to the HE_{11} mode and travels with virtually no loss through the line. Power in higher order Gaussian or non-Gaussian modes will couple to higher order corrugated

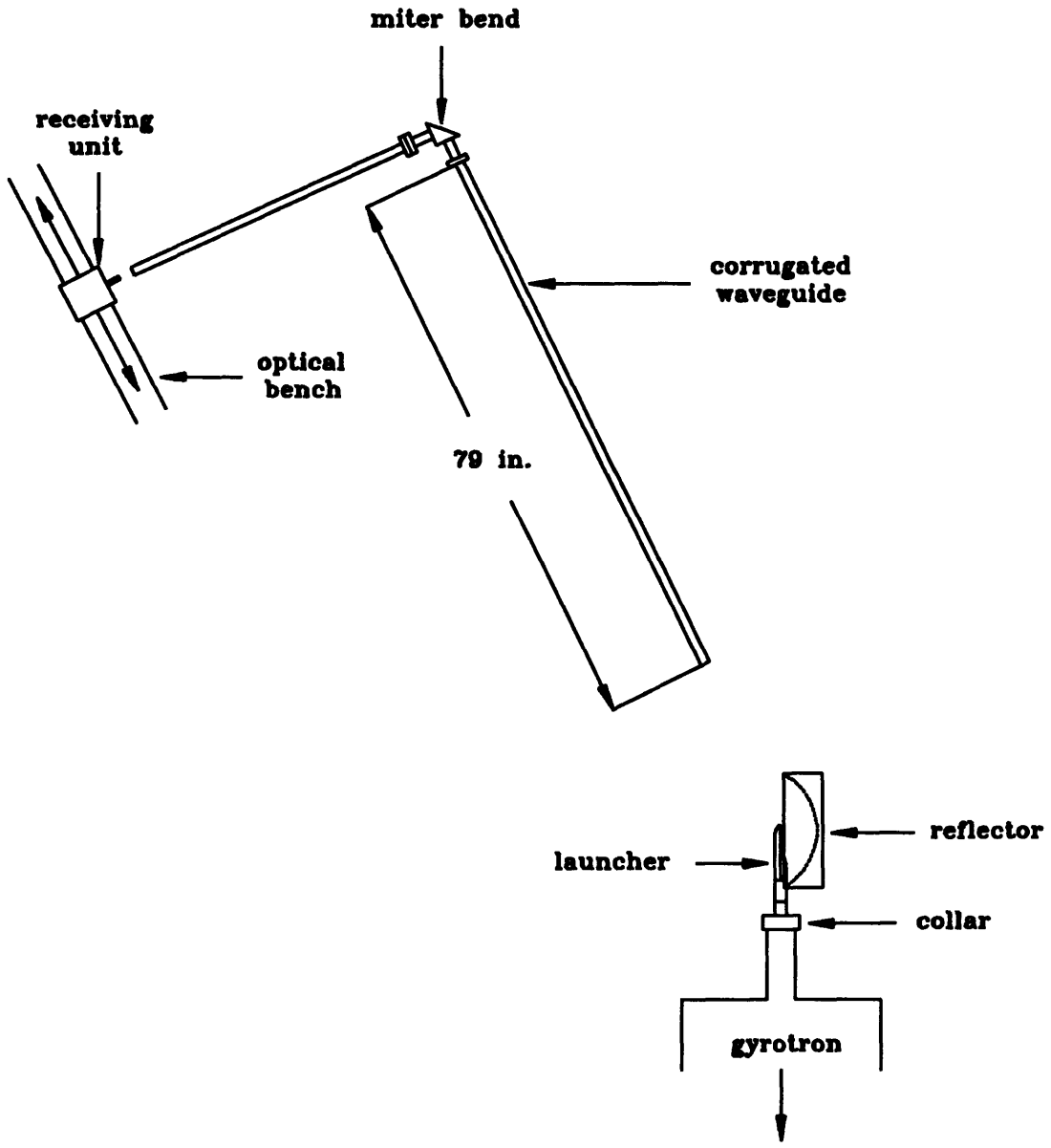

Figure 2.15 Schematic of the the corrugated waveguide experimental apparatus.

waveguide modes or will be reflected at the guide input. Thus, the ratio of the total power in the HE_{11} mode at the guide exit to the total power at the entrance is an approximate measure of TEM_{00} content in the input beam.

A two dimensional scan of the radiation leaving the corrugated waveguide was made. The receiving unit, consisting of a truncated WR6 waveguide, a calibrated attenuator, and a WR6 diode, was oriented in the direction for measuring E_y. The unit was mounted on an optical bench, perpendicular to the incoming beam. The detector was moved vertically and

horizontally in a plane at d = 11 cm. The results of the scan are shown in Fig. 2.16, where lines of constant $|E_y|^2$ are plotted in dB below peak intensity. Figure 2.16 shows a small, Gaussian-like radiation pattern with $w_{0x} = w_{0y}$ = 1.3 cm . The theoretical beam radii for the near field pattern of the HE_{11} launched from a 1.25 inch guide in the plane d = 11 cm are $w_{0x} = w_{0y}$ = 1.35 cm. The peak intensity in the cross polarization, E_x, was measured at <-21 dB below the peak of the E_y intensity. The experimental scan (Fig. 2.16) indicates that the radiation launched from the corrugated waveguide is predominantly in the HE_{11} mode.

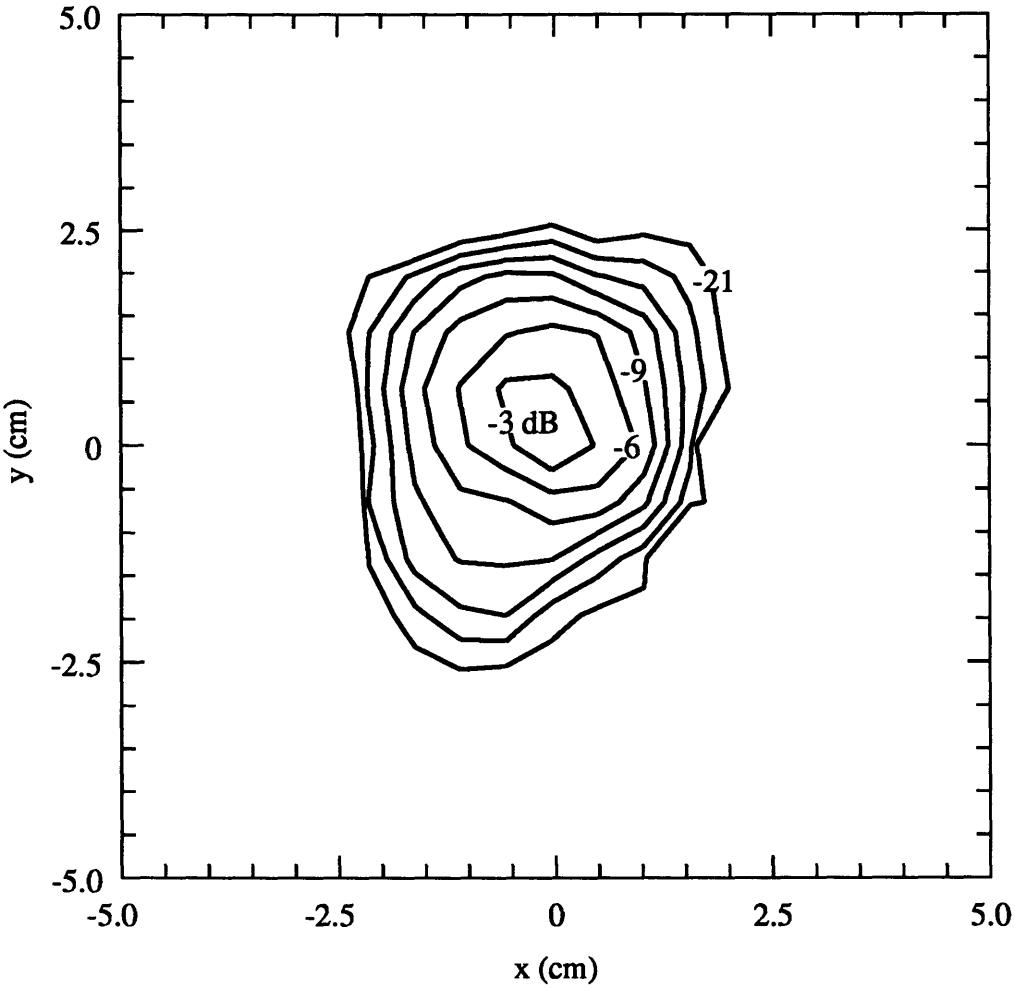

Figure 2.16 Diode scan of the radiation leaving the corrugated waveguide transmission line. The scan was made in the plane perpendicular to the guide at a distance d = 11 cm from the exit. Lines of constant $|E_y^2|$ are plotted in dB below peak intensity. The peak of the cross polarization, E_x, is <-21 dB from the peak of E_y.

Next, the 10 cm laser calorimeter was placed at the guide exit and the power leaving the line was measured to be 80% of the total power leaving the gyrotron. The overall conversion efficiency of the $TE_{16,2}$ mode to an HE_{11} mode is

$$\eta_{(TE_{16,2}-HE_{11})}(\text{measured}) = \frac{\text{power in } HE_{11}}{\text{power in } TE_{16,2}} = \frac{0.80}{0.972} = 0.82 \qquad (2.30)$$

The predicted conversion efficiency (Eq. 2.29), 82.5%, is in excellent agreement with the measured efficiency, 82%.

The conversion efficiency for transforming the $TE_{16,2}$ mode to the HE_{11} mode can be used to estimate the efficiency of transforming the $TE_{16,2}$ mode to the TEM_{00} Gaussian mode in free space by correcting for the 98% coupling efficiency from the TEM_{00} to the HE_{11} mode.

$$\eta_{(TE_{16,2}-TEM_{00})} = \frac{\text{power in } HE_{11}}{\text{power in } TE_{16,2}} \frac{1}{\text{coupling efficiency}} = \frac{0.80}{0.972} \frac{1}{0.98} = 0.83 \qquad (2.31)$$

Thus, the $TE_{16,2}$–TEM_{00} conversion efficiency estimated from the corrugated waveguide experiments (83%) is in excellent agreement with the efficiency estimated from the beam expansion measurements and mode content calculation (84%).

2.4 Discussion of Results

The experiments described in Section 2.3 fully characterized the operation of the $TE_{16,2}$ Vlasov-type mode converter. First, far field polar scans of the power from the collector showed that the gyrotron operates in the $TE_{16,2}$ mode with 99% mode purity. An external waveguide, or sleeve, which was designed to continue the collector after the vacuum window, was mounted at the output of the gyrotron and a second set of far field polar scans showed that the power at the sleeve exit was composed of 97.2% $TE_{16,2}$ mode with the remaining 2.8% in adjacent azimuthal and radial modes. The additional mode conversion was caused by a slight tilt or offset of the external waveguide, and by the break in the waveguide due to the presence of the vacuum window.

Next, the launcher was mounted on the sleeve and near field scans were made. The pattern predicted by vector diffraction theory for the mode mix suggested by the polar scan (0.3% $TE_{16,1}$, 97.2% $TE_{16,2}$, 0.3% $TE_{16,3}$, 1.6% $TE_{15,1}$, and 0.6% $TE_{17,2}$) was in excellent agreement with the experimentally observed pattern. However, the pattern predicted by geometric optics theory was significantly smaller than either the measured pattern or the pattern predicted by diffraction theory. An integration over the diffraction theory pattern showed that only 75% of the power fell within the geometric optics extents. The mirror extents were chosen based on diffraction theory pattern and an integration was performed over the measured pattern to show that 97% of the power would be incident on the reflector.

The reflector was placed at its design position and measurements of the beam produced by the converter were made. Calorimetric power measurements showed that 95% of the total power incident on the launcher was directed to the focal plane. A diode scan in a plane perpendicular to the incoming beam showed a strong $TE_{16,2}$ mode focus, with two other focii corresponding to the neighboring azimuthal modes, $TE_{15,2}$ and $TE_{17,2}$. An integration over the experimental pattern showed that 97.8% of the power was contained in the $TE_{16,2}$ focus, 1.6% was found in the $TE_{17,2}$ focus and 0.6% was in the $TE_{17,2}$ focus. This power break down agrees well with the mode mixes inferred from the far field polar scan at the sleeve output and the near field launcher pattern scan.

The focal plane scans point out a useful property of the Vlasov-type converter. Each mode that is incident on the launcher appears as a distinct focal spot in the far field. The converter is, thus, a good diagnostic for determining mode content.

Next, the beam radius expansion measurements showed that although the $TE_{16,2}$ pattern has a Gaussian-like amplitude profile in the focal plane, the beam expands in a non-Gaussian way, indicating phase front aberrations. A dot product integration suggested that 88% of the $TE_{16,2}$ beam, or $0.88 \times 0.95 = 0.84$ of the total $TE_{16,2}$ power leaving the gyrotron, was in the TEM_{00} mode, with the remaining 12% in higher order modes. The non-Gaussian

components are the result of designing the reflector surface with geometric optics. It was previously noted that only 75% of the radiation falls within the geometric optics extents. The additional radiation, which is not predicted by ray optics, is incident on a surface designed by ray optics. Thus, it is not surprising that this radiation outside the bounds of the geometric optics pattern arrives at the focus out of phase, leading to aberrations on the beam.

Finally, corrugated waveguide experiments showed that 82% of the $TE_{16,2}$ power from the sleeve is coupled into the HE_{11} mode of a 1.25 inch diameter corrugated waveguide. The $TE_{16,2}$–HE_{11} conversion efficiency is predicted at 82.5% by knowing that 95% of the $TE_{16,2}$ power from the sleeve arrives at the focus and that 88% of this power is in the TEM_{00} mode. The measured $TE_{16,2}$–HE_{11} efficiency, 82%, and the predicted efficiency, 82.5% are in excellent agreement. By correcting the $TE_{16,2}$–HE_{11} measured efficiency for the 98% theoretical coupling of the TEM_{00} mode to the HE_{11} mode of the corrugated guide, the $TE_{16,2}$–TEM_{00} conversion efficiency is found to be 83%.

It is somewhat surprising that the Vlasov-type converter, with a design rooted in the geometric optics approximation, can achieve such a high conversion efficiency. The geometric optics model is, in fact, a fairly good model for describing the pattern that is radiated from the Vlasov launcher. As shown in Fig. 2.9, the near field launcher pattern predicted by the rigorous vector diffraction theory is quite similar to the pattern predicted by geometric optics. The simple geometric optics theory predicts a uniformly illuminated rectangular patch and the vector diffraction also predicts a rectangular pattern. The -6 dB lines of the vector diffraction theory pattern are approximately the same size as the geometric optics prediction, indicating that geometric optics describes $\sim$ 75% of the beam in an accurate manner. Thus a reflector designed with geometric optics should focus the majority of the power to the desired Gaussian beam, as was observed in the experiments described in the previous section.

The possibility of improving the overall efficiency of the Vlasov-type converter exits with the Stratton-Chu diffraction theory. With a more sophisticated reflector design that incorporates vector diffraction theory as well as geometric optics theory, the phase aberrations on the beam could be lessened and more power could be successfully converted into the TEM_{00} mode.

However, even with the improvements that a vector diffraction theory mirror design would bring, the Vlasov-type converter has inherent properties that make it undesirable for converting certain classes of modes. As discussed in Section 2.1, the geometric optics expansion angle of the radiation pattern from the Vlasov-type launcher, α, goes as $\cos^{-1}(\frac{m}{\nu_{mp}})$. For $TE_{m,p}$ whispering gallery modes, where the azimuthal index, m, is large

and the radial index, p, is small, $\frac{m}{\nu_{mp}} \sim 1$, and the expansion angle, α, is small. However, for high order volume modes, where m is not much greater than p, $\frac{m}{\nu_{mp}}$ is smaller, and the expansion angle gets to be quite large. Since the reflector must subtend a minimum of 2α degrees, the mirrors for volume mode Vlasov-type converters are large. In fact, conventional Vlasov-type converters become impractical for high order volume modes, and the converter's applicability is limited to whispering gallery modes in many cases.

Another limitation is the substantial diffraction from the Vlasov-type launcher. For a whispering gallery mode, the radiation on the launching aperture is concentrated in a region between the caustic radius and the waveguide radius. Since this illuminated region on the launching aperture is small, the diffraction of the radiated pattern will be large. The Stratton-Chu theory indicates that the true angular expansion angle for a whispering gallery mode launcher is about 4α, which is twice the value predicted by geometric optics. Large diffraction leads to large reflectors, which are impractical in many cases.

Because much of the near field pattern falls outside the bounds of geometric optics predictions, a reflector designed solely with geometric optics is not always adequate. With the vector diffraction theory developed as part of this thesis, and improved reflector design is possible. However, to design a reflector with diffraction theory is complicated, and the amount of computing time required renders the design process unattractive. Perhaps a more useful solution is to modify the launcher so that a more controlled beam is radiated from the aperture, which is the method used in designing the converter described in the next chapter.

Based on the above discussion, it can be concluded that for whispering gallery modes ($m >> 1, p \approx 1$), the Vlasov-type converter with a geometric optics reflector design is practical and can achieve conversion efficiencies in excess of 80%. Higher efficiencies are possible if the Stratton-Chu vector diffraction theory could be incorporated in the design of the reflector surface. However, for volume modes ($m, p >> 1$), or modes with extremely large diffraction, the approach loses validity as the reflectors get larger and less practical.

The second converter in the proposed thesis, which is a variation on the Vlasov-type, is applicable for converting high order volume modes in overmoded waveguides to Gaussian modes in free space.

Chapter 3

Pre-Bunching Converter

A quasi-optical mode converter was designed to transform the $TE_{22,6}$ mode at 110 GHz to a Gaussian beam in free space. The converter was configured so that it could be tested external to the gyrotron, which was the method used in the $TE_{16,2}$ Vlasov-type converter experiments, or internal to the tube. When the converter is inside the gyrotron, it serves not only to convert the output mode, but also to separate the spent electron beam from the microwave power. The internal converter has several advantages over a long, cylindrical collector leading from the cavity to the output window (Fig. 1.1). With the converter inside the gyrotron, the microwaves exit the tube along a path that is perpendicular to the electron beam path. Contrary to the long cylindrical collector configuration, any power reflected from the window is not likely to be directed back into the interaction cavity. Also, separating the spent electron beam from the microwaves allows for a depressed beam collector, which would improve the overall efficiency of the tube. Additionally, the internal converter configuration increases the vacuum pumping conductance within the gyrotron tube, which improves the running conditions.

Thus, a size constraint was imposed with the requirement that the entire converter fit within the 5 inch diameter vacuum tube of the $TE_{22,6}$ gyrotron oscillator. The geometric optics azimuthal expansion angle (2α) for the $TE_{22,6}$ mode is 122° and, as was shown in the previous chapter, a mirror must subtend at least 4α in order to intercept all the radiation launched from a Vlasov-type antenna. The desire to improve upon the results of the Vlasov-type converter, along with the impracticality of a mirror subtending 244° led to a modification in the design of the previously discussed mode converter. The Vlasov launcher was altered in an effort to pre-shape the fields on the aperture, allowing for a more controlled, well defined beam to be radiated from the launcher.

The $TE_{22,6}$ pre-bunching converter, which is a modified Vlasov-type, consists of an irregular waveguide section, or pre-bunching section, followed by a step cut launching aperture (Fig. 1.3) and two focussing reflectors. The converter was built and tested both externally and internally on a $TE_{22,6}$ gyrotron operating at 110 GHz.

The vacuum window is a limiting component in determining the output power capability

of a high frequency gyrotron oscillator. Because of power handling limitations for present window designs, it may prove advantageous to divide the microwave radiation produced by the gyrotron and direct it through two vacuum windows, which would serve to reduce the power handling requirements of each window by a factor of two. With this in mind, four additional reflectors were designed to split the fundamental Gaussian beam formed by the launcher and two mirror relay into two fundamental Gaussian beams, each containing approximately half the total power. The beam splitting mirror relay was built and tested in conjunction with the external pre-bunching converter experiments.

The design, theoretical analysis, and experimental verification of the pre-bunching converter and beam splitting mirror relay are discussed below.

3.1 Coupled Mode Theory and Launcher Design

The wall current, or field intensity on the wall, of a pure rotating mode travelling in a cylindrical guide (Eqs. 2.1 and 2.2) is uniform over the entire waveguide wall. The goal of the pre-bunching section is to create a mode mix in the launching waveguide such that the wall current exhibits a Gaussian, rather than uniform, profile. This favorable mode mix can be achieved by pumping power from the main mode, $TE_{m,p}$, to two satellite modes, the TX_{m_i,p_i} and the TX_{m_j,p_j}. The symbol TX indicates that the satellite mode can be either TE or TM. A helicoidal converter, with a wall shape described by Eq. 3.1, is used to obtain this type of mode conversion [12][13].

$$r(\phi, z) = a\left[1 + \epsilon_1(z)\cos(\beta_1 z - l_1\phi) + \epsilon_2(z)\cos(\beta_2 z - l_2\phi)\right], \tag{3.1}$$

where

$$\beta_1 \approx \pm(\beta_0 - \beta_i) \tag{3.2}$$

$$l_1 = \pm(m_0 - m_i) \tag{3.3}$$

$$\beta_2 \approx \pm(\beta_0 - \beta_j) \tag{3.4}$$

$$l_2 = \pm(m_0 - m_j) \tag{3.5}$$

The subscript 0 corresponds the main mode, and the subscripts i and j refer to the first and second satellite modes, respectively. The first cosine variation, $\epsilon_1(z)\cos(\beta_1 z - l_1\phi)$, couples power from the main mode the the first satellite mode, TX_{m_i,p_i}, and the second cosine variation, $\epsilon_1(z)\cos(\beta_1 z - l_1\phi)$, couples power from the main mode the the second satellite, TX_{m_j,p_j}. In Eq. 3.1, a is the constant mean radius of the rippled wall waveguide.

The fields in a smooth walled cylindrical waveguide of constant radius a are the normal modes of the guide, described by Eqs. 2.1 and 2.2. When the wall is distorted, as in Eq. 3.1, the fields are no longer described by one normal mode and the wall perturbations effectively couple energy between several normal modes of the waveguide.

In general, the equations for coupling between forward travelling modes are given by:

$$\frac{dA_i^+}{dz} = ik_{zi}A_i^+ + \sum_p c_{ip}A_p^+ + \sum_q c_{iq}A_q^+ \tag{3.6}$$

$$\frac{dA_j^+}{dz} = ik_{zj}A_j^+ + \sum_p c_{jp}A_p^+ + \sum_q c_{jq}A_q^+, \tag{3.7}$$

where the subscripts i and p denote TE modes and the subscripts q and j denote TM modes. In Eqs. 3.6 and 3.7, A is the complex amplitude of the mode. For weak waveguide deformations of the form $r(\phi, z) = a + \delta(\phi, z)$, previously reported methods [24–26] can be used to determine the coupling coefficients in Eqs. 3.6 and 3.7, c_{ip}, c_{iq}, c_{jp}, and c_{jq}.

$$c_{ip} = \frac{1}{2}\left[Q_{ip}\frac{\omega\mu}{\sqrt{k_{zi}k_{zp}}} + R_{ip}\sqrt{\frac{k_{zp}}{k_{zi}}}\right] \tag{3.8}$$

$$c_{iq} = \frac{1}{2}S_{iq}\frac{\omega}{c\sqrt{k_{zi}k_{zq}}} \tag{3.9}$$

$$c_{jp} = \frac{1}{2}\left[T_{jp}c\sqrt{\frac{k_{zj}}{k_{zp}}} + U_{jp}\frac{1}{c}\sqrt{\frac{k_{zp}}{k_{zj}}} + V_{jp}\frac{c}{\omega}\sqrt{k_{zj}k_{zp}}\right] \tag{3.10}$$

$$c_{jq} = \frac{1}{2}\left[W_{jq}\sqrt{\frac{k_{zj}}{k_{zq}}} + X_{jq}\frac{\omega\epsilon}{\sqrt{k_{zj}k_{zq}}}\right] \tag{3.11}$$

To first order in the small amplitude perturbation, $\delta(\phi, z)$, the eight unknowns in Eqs. 3.8–3.11 are defined by Eqs. 3.12–3.19 [24–26]. In the following equations, the subscripts i, p, j, and q refer to modes i, p, j, and q, where mode i is the TE_{m_1,p_1}, mode p is the TE_{m_2,p_2}, mode j is the $TM_{m_1',p_1'}$, and mode q is the $TM_{m_2',p_2'}$.

$$Q_{ip} = \frac{i(\frac{\nu_{m_2p_2}}{a})^2}{a\pi\omega\mu\sqrt{\nu_{m_2p_2}^2 - m_2^2}} \times$$

$$\int_0^{2\pi} \left[\frac{im_1 e^{im_1\phi}}{\sqrt{\nu_{m_1p_1}^2 - m_1^2}} \frac{\partial\delta(\phi,z)}{\partial\phi} + \delta(\phi,z) e^{im_1\phi} \sqrt{\nu_{m_1p_1}^2 - m_1^2} \right] e^{-im_2\phi} d\phi \quad (3.12)$$

$$R_{ip} = \frac{m_1 m_2}{a\pi\sqrt{\nu_{m_1p_1}^2 - m_1^2}\sqrt{\nu_{m_2p_2}^2 - m_2^2}} \int_0^{2\pi} e^{im_1\phi} e^{-im_2\phi} \frac{\partial\delta(\phi,z)}{\partial z} d\phi \quad (3.13)$$

$$S_{iq} = \frac{im_1}{a\pi\sqrt{\nu_{m_1p_1}^2 - m_1^2}} \int_0^{2\pi} e^{im_1\phi} e^{-im_2'\phi} \frac{\partial\delta(\phi,z)}{\partial z} d\phi \quad (3.14)$$

$$T_{jp} = \frac{i(\frac{\nu_{m_2p_2}}{a})^2}{a\pi\omega\mu\sqrt{\nu_{m_2p_2}^2 - m_2^2}} \int_0^{2\pi} \left[e^{im_1'\phi} \frac{\partial\delta(\phi,z)}{\partial\phi} + im_1' e^{im_1'\phi} \delta(\phi,z) \right] e^{-im_2\phi} d\phi \quad (3.15)$$

$$U_{jp} = \frac{m_2}{a\pi\omega\epsilon\sqrt{\nu_{m_2p_2}^2 - m_2^2}} \left(\frac{\mu_{m_1'p_1'}}{a} \right)^2 \int_0^{2\pi} e^{im_1'\phi} e^{-im_2\phi} \delta(\phi,z) d\phi \quad (3.16)$$

$$V_{jp} = \frac{-im_2}{a\pi\sqrt{\nu_{m_2p_2}^2 - m_2^2}} \int_0^{2\pi} e^{im_1'\phi} e^{-im_2\phi} \frac{\partial\delta(\phi,z)}{\partial z} d\phi \quad (3.17)$$

$$W_{jq} = \frac{1}{a\pi} \int_0^{2\pi} e^{im_1'\phi} e^{-im_2'\phi} \frac{\partial\delta(\phi,z)}{\partial z} d\phi \quad (3.18)$$

$$X_{jq} = \frac{i}{a\pi\omega\epsilon} \left(\frac{\mu_{m_1'p_1'}}{a} \right)^2 \int_0^{2\pi} e^{im_1'\phi} e^{-im_2'\phi} \delta(\phi,z) d\phi, \quad (3.19)$$

where μ_{mp} is the p^{th} zero of $J_m(x)$.

The integrals in Eqs. 3.12–3.19 can be solved for any small amplitude perturbation, $\delta(\phi, z)$. For the helicoidal converter of interest, $\delta(\phi, z) = a\epsilon(z)\cos(\beta z - l\phi)$. Substituting this function into Eqs. 3.12–3.19 and solving gives:

$$Q_{ij} = \frac{-i\nu^2_{m_2p_2}}{a^2\pi\sqrt{\nu^2_{m_1p_1} - m_1^2}\sqrt{\nu^2_{m_2p_2} - m_2^2}}(m_1m_2 - \nu^2_{m_1p_1})\gamma_0 \tag{3.20}$$

$$R_{ij} = \frac{m_1m_2}{a\pi\sqrt{\nu^2_{m_1p_1} - m_1^2}\sqrt{\nu^2_{m_2p_2} - m_2^2}}\gamma_z \tag{3.21}$$

$$S_{iq} = \frac{im_1}{a\pi\sqrt{\nu^2_{m1p1} - m_1^2}}\gamma_z \tag{3.22}$$

$$T_{jp} = \frac{-m_2\nu^2_{m_2p_2}}{a^2\pi\omega\mu\sqrt{\nu^2_{m_2p_2} - m_2^2}}\gamma_0 \tag{3.23}$$

$$U_{jp} = \frac{m_2\mu^2_{m_1'p_1'}}{a^2\pi\omega\epsilon\sqrt{\nu^2_{m_2p_2} - m_2^2}}\gamma_0 \tag{3.24}$$

$$V_{jp} = \frac{-im_2}{a\pi\sqrt{\nu^2_{m_2p_2} - m_2^2}}\gamma_z \tag{3.25}$$

$$W_{jq} = \frac{\gamma_z}{a\pi} \tag{3.26}$$

$$X_{jq} = \frac{i\mu^2_{m_1'p_1'}}{a^2\pi\omega\epsilon}\gamma_0, \tag{3.27}$$

where

$$\begin{aligned}
\gamma_0 &= \pi\epsilon(z)e^{-i\beta z} && if \quad m_2 - m_1 = l, \quad l \neq 0 \\
\gamma_0 &= \pi\epsilon(z)e^{i\beta z} && if \quad m_2 - m_1 = -l, \; l \neq 0 \\
\gamma_0 &= 2\pi\epsilon(z)\cos(\beta z) && if \; m_2 = m_1, \qquad l = 0 \\
\gamma_0 &= 0 && \text{otherwise}
\end{aligned} \tag{3.28}$$

and

$$\gamma_z = a\pi[\epsilon'(z) - i\beta\epsilon(z)]e^{-i\beta z} \qquad if\ \ m_2 - m_1 = l, \qquad l \neq 0$$

$$\gamma_z = a\pi[\epsilon'(z) + i\beta\epsilon(z)]e^{i\beta z} \qquad if\ \ m_2 - m_1 = -l, \qquad l \neq 0$$

$$\gamma_z = 2\pi a[\epsilon'(z)\cos(\beta z) - \beta\epsilon(z)\sin(\beta z)] \quad if\ \ m_2 = m_1, \quad l = 0$$

$$\gamma_z = 0 \qquad \text{otherwise} \tag{3.29}$$

where the prime ($'$) denotes the first derivative with respect to z, $\frac{d}{dz}$.

By substituting Eqs. 3.20–3.29 into Eqs. 3.8–3.11, the coupling coefficients for the small amplitude helicoidal wall perturbation, $r(\phi, z) = a\,[1 + \epsilon(z)\cos(\beta z - l\phi)]$, can be solved. The pre-bunching waveguide of interest, with the wall shape described by Eq. 3.1, is the superposition of two such helicoidal perturbations. In analyzing this waveguide, the coupling coefficients for each term can be solved independently and the results superimposed in Eqs. 3.6 and 3.7.

There are two principle design criteria for the rippled wall waveguide section. First, the section must convert the main mode, the $TE_{22,6}$ in this case, to a mix of modes such that 100% of the power in the waveguide is contained in a bundle with a Gaussian-like amplitude profile. Second, this profile must be achieved in a short distance, typically <20 cm, so that the launcher is short enough to avoid interception of the expanding spent electron beam.

The geometric optics model, although it is not used in the analysis of the rippled wall section, is helpful in illustrating the method of selecting appropriate satellite modes. Figure 3.1 shows the unfolded cylindrical waveguide. In the ray optics view of rotating cylindrical waveguide modes, a ray travels in a helical path around the waveguide, reflecting from the wall at bounce points marked 'b' in Fig. 3.1. The bounce points fall on helical line **A**. All of the rays that form the waveguide mode reflect from the wall in area **B**, where **B** is the region formed when parallel lines **C** and **C**$'$ are drawn from neighboring bounce points to the next intersection with line **A**. As was previously described in Chapter 2, the azimuthal extent of region **B**, or the azimuthal separation of two bounce points, is 2α. The axial extent of region **B** is $L' = 2\pi R_w \frac{k_z}{k_r}\frac{\sin\alpha}{\alpha}$. For a pure, rotating $TE_{m,p}$ mode, region **B** is uniformly illuminated by the rays. After all rays are reflected from the wall in region **B**, they arrive a bounce points in a similar region, **B**$'$, then travel to region **B**$''$, etc.

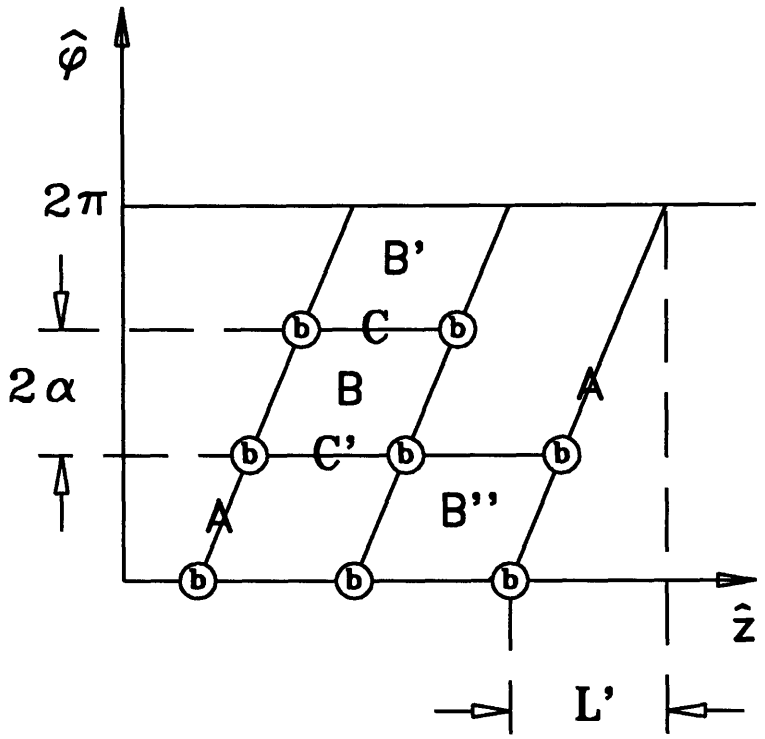

Figure 3.1 Geometric optics view of a cylindrical waveguide mode. The ray travels along helical line **A** reflecting from the waveguide wall at bounce points b. All rays have one bounce point in regions **B**, **B′** and **B″**.

As is evident in Fig. 3.1, the helical cut of a Vlasov-type launcher is equivalent to removing the waveguide wall in the region **B″**; each ray is reflected from the wall in region **B′** and then is radiated out into free space. It is the goal of the pre-bunching waveguide section to improve the radiation characteristics of the launched beam by illuminating the launching region (**B′**) with a Gaussian ray distribution rather than a uniform distribution. Viewing the problem in this light helps in selecting the appropriate satellite modes.

For the $TE_{22,6}$ mode, $2\alpha = 2\cos^{-1}\frac{m}{\nu_{mp}} \approx 122^o$. Since the azimuthal extent of region **B** is 2α, there are three such regions in the 2π radians around the waveguide. Thus, the

satellite mode responsible for azimuthal bunching should have an azimuthal mode index, m, that is 22±3, i.e. m = 19 or m = 25. A mode with an azimuthal index m = 19 or m = 25 will beat with the $TE_{22,6}$ mode and form three peaks around the azimuth of the guide, one for each region **B**.

In order to decouple the azimuthal and the longitudinal bunching, it is desirable to choose an azimuthal satellite mode with $k_z \approx k_{z_{22,6}}$, which is equivalent to choosing a mode with $\nu_{mp} \approx \nu_{22,6}$. There are two modes with $m = 22 \pm 3$ and $\nu_{mp} \approx \nu_{22,6}$, the $TE_{19,7}$ and the $TE_{25,5}$ modes. Either mode can be selected and the helicoidal coefficients, β_1 and l_1, can be found from Eqs. 3.2–3.5. It is interesting to note that because of the symmetry of the mode spectrum, the $TE_{22,6}$ mode couples well to the $TE_{25,5}$ mode through the same helicoidal wall shape that provides coupling from the $TE_{22,6}$ mode to the $TE_{19,7}$ mode. Figure 3.2 shows the resulting field intensity on the waveguide wall ($|E_r|^2$) when the $TE_{22,6}$ mode is mixed with the $TE_{19,7}$ and $TE_{25,5}$ modes. For a pure, rotating $TE_{22,6}$ mode, the field intensity would be uniform at all points on the waveguide wall. Figure 3.2 clearly shows the azimuthal bunching that results from the favorable mixture of modes.

The mode that performs longitudinal bunching should have an azimuthal index m = 22 ± 1 and an axial wave number, $k_z - k_{z_{22,6}} \approx \frac{L'}{2}$. When these conditions are met, the radiation will form bundles that follow along the helical ray path, line **A**. The two modes that meet these criteria for the $TE_{22,6}$ mode are the $TE_{21,6}$ and the $TE_{23,6}$ modes. Just as in the case of the azimuthal satellite modes, the $TE_{22,6}$ mode couples strongly to the $TE_{23,6}$ mode through the same wall perturbations that couple the $TE_{22,6}$ mode to the $TE_{21,6}$ mode. Once again, the helicoidal coefficients, β_2 and l_2, can be solved with Eqs. 3.2–3.5. Figure 3.3 shows the resulting field intensity on the waveguide wall ($|E_r|^2$) when the $TE_{22,6}$ mode is mixed with the $TE_{21,6}$ and $TE_{23,6}$ modes. The favorable mode mixture has created bunching along the helical line **A**.

In the pre-bunching launcher, two helicoidal cosine variations are used simultaneously (Eq. 3.1) to effect both azimuthal and longitudinal bunching. When the satellite modes are properly selected, the result is one Gaussian-like radiation bundle in the center of each region **B**, **B'**, **B''**, etc.

Thus, the $TE_{19,7}$ mode was chosen as the azimuthal bunching satellite mode and the $TE_{23,6}$ mode was chosen to perform the longitudinal bunching. The helicoidal coefficients were solved with Eqs. 3.2–3.5 and were put into Eq. 3.1 to specify the wall shape. A computer code, using Eqs. 3.6 - 3.29, was written to solve for the **E** and **H** fields at all

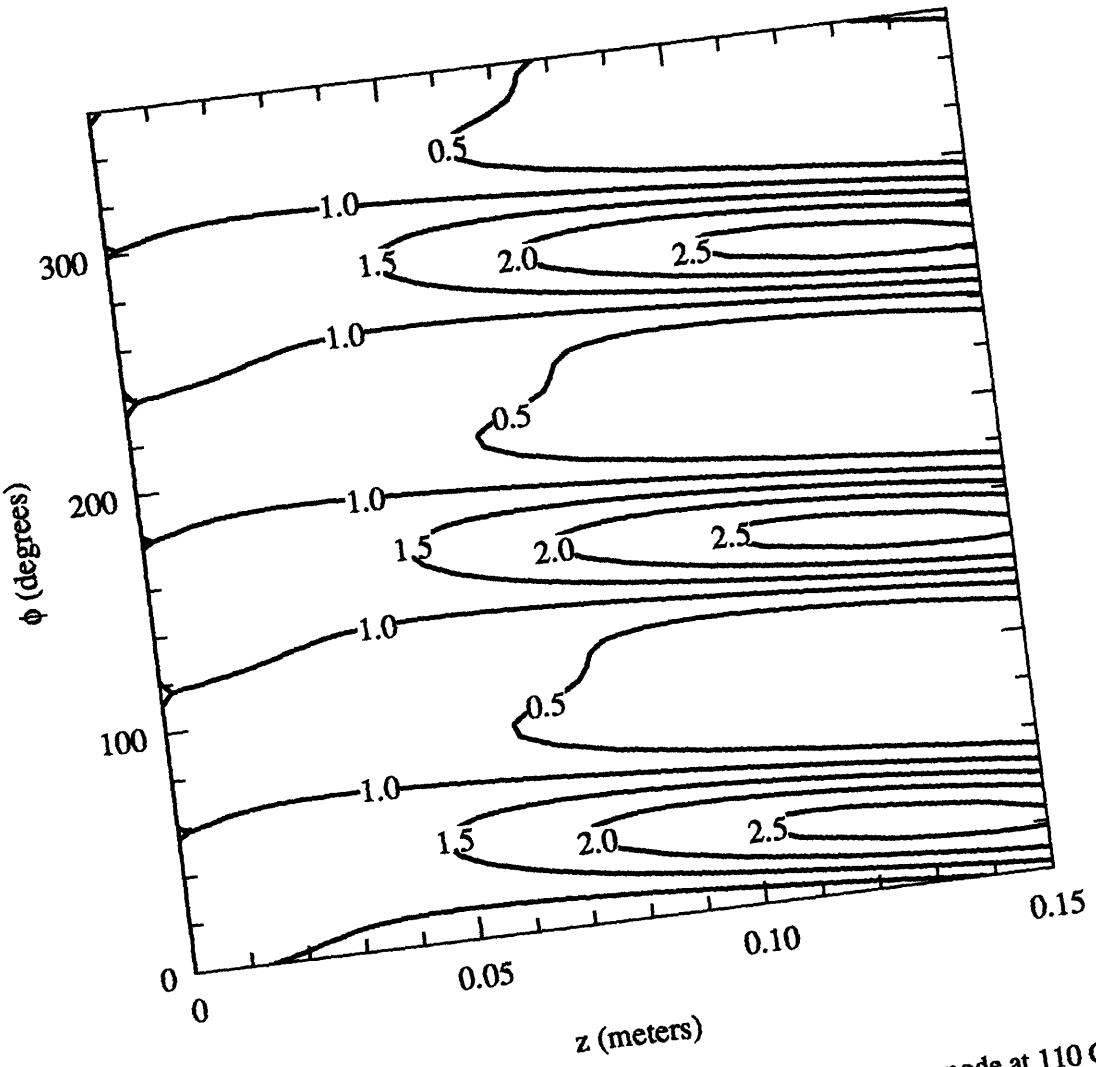

Figure 3.2 Field intensity ($|E_r|^2$) on the waveguide wall when the $TE_{22,6}$ mode at 110 GHz is mixed with the $TE_{19,7}$ and $TE_{25,5}$ modes, also at 110 GHz. Lines of constant intensity, normalized to the uniform intensity of a pure $TE_{22,6}$ rotating mode, are plotted in steps of 0.5.

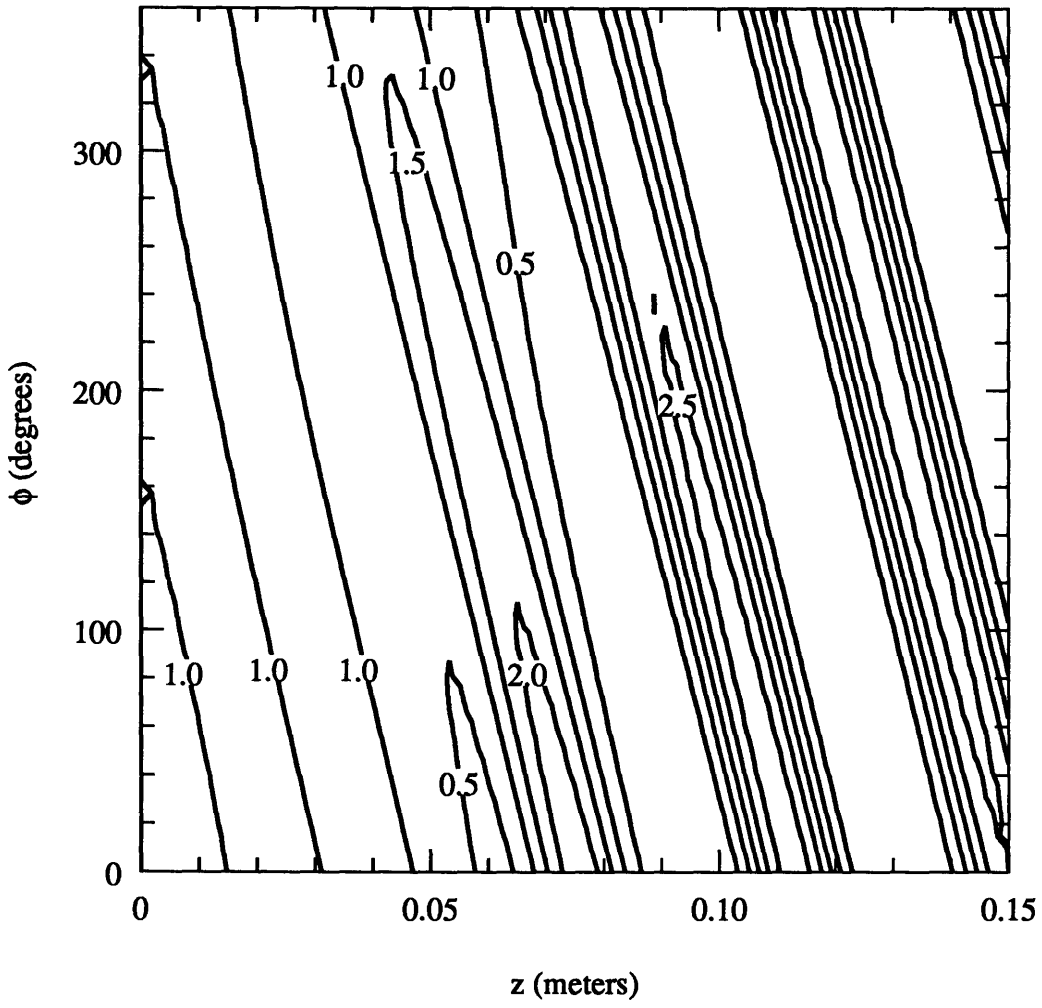

Figure 3.3 Field intensity ($|E_r|^2$) on the waveguide wall when the $TE_{22,6}$ mode at 110 GHz is mixed with the $TE_{21,6}$ and $TE_{23,6}$ modes, also at 110 GHz. Lines of constant intensity, normalized to the uniform intensity of a pure $TE_{22,6}$ rotating mode, are plotted in steps of 0.5.

points in the irregular waveguide described by Eq. 3.1. Using this program and the satellite mode selection method described above, the $TE_{22,6}$ rippled wall launcher was designed.

Table 3.1 summarizes the design parameters for the $TE_{22,6}$ pre-bunching waveguide section. The helicoidal converter was designed to operate on the left rotating $TE_{22,6}$ mode, which is the mode produced by the gyrotron oscillator was used in test. The launcher can, certainly, be designed for either a right or left rotating input mode, but the sense of the helicoidal ripples fixes the converter applicability to one rotation or the other.

input mode	$TE_{22,6}$
frequency	110 GHz
mean radius, a	2.1 cm
$\epsilon_1(z) = \epsilon_1$	0.0019
$\epsilon_2(z) = \epsilon_2$	0.0019
β_1	0.168 cm^{-1}
β_2	1.68 cm^{-1}
l_1	3
l_2	1
1^{st} satellite mode	$TE_{19,7}$ ($TE_{25,5}$)
2^{nd} satellite mode	$TE_{23,6}$ ($TE_{21,6}$)
$\alpha = \cos^{-1}\frac{m}{\nu_{mp}}$	61.17^o
$\theta_B = \tan^{-1}\frac{k_r}{k_z}$	70.56^o

Table 3.1 Design parameters for the $TE_{22,6}$ pre-bunching launcher.

The launcher described in Table 3.1 was analyzed with the coupled mode theory computer code and the results are plotted in Figs. 3.4 and 3.5. Figure 3.4 shows the mode composition in the pre-bunching launcher. The $TE_{22,6}$ mode is incident at $z = 0$, at which

point helicoidal perturbations begin. As the radiation travels along the $\hat{z}$ axis, power in the $TE_{22,6}$ mode is coupled into the four primary satellite modes, the $TE_{19,7}$ / $TE_{25,5}$ pair through the first helicoidal cosine, and the $TE_{23,6}$ / $TE_{21,6}$ pair through the second cosine. In addition, fifteen other modes, listed in Table 3.2, were found to couple through the wall perturbations.

$TE_{19,6}$	$TE_{21,7}$	$TE_{18,7}$
$TE_{24,5}$	$TE_{20,6}$	$TE_{20,7}$
$TE_{15,8}$	$TE_{17,7}$	$TE_{17,8}$
$TE_{16,8}$	$TE_{28,4}$	$TE_{26,5}$
$TE_{24,6}$	$TE_{27,4}$	$TE_{23,5}$

Table 3.2 Additional modes included in the coupled mode theory analysis of the $TE_{22,6}$ pre-bunching launcher.

Figure 3.5 shows the resulting field intensity ($|E_r|^2$) on the wall for the mode mix generated by the pre-bunching section. A distinct Gaussian profile with a peak to valley intensity ratio > 40 is indicated.

The well formed radiation bunch is launched from the rippled wall section by cutting the waveguide wall around one Gaussian bundle, where wall current is at a minimum, which virtually eliminates edge diffraction effects. The Stratton-Chu vector diffraction theory, described in Section 2.2, can be used to simulate the radiation of the aperture fields and examine the properties of the launched beam. The step cut aperture over which the waveguide fields are integrated extends from 10.5 cm to the end of the launcher in the axial direction and is bounded by the chords joining $\phi = 225^\circ$ and $\phi = 325^\circ$ at the two ends of the axial cut. The fields on this aperture, calculated with the coupled mode theory, are shown in Fig. 3.6. Lines or constant $|E_x|^2$ are shown in dB below peak intensity.

Figure 3.7 shows the configuration under consideration. Two coordinate systems are indicated in the figure. In the launcher coordinate system, $\hat{z}$ is the direction parallel to the waveguide axis, $\hat{y}$ is the direction normal to the step cut aperture, which is nearly equal

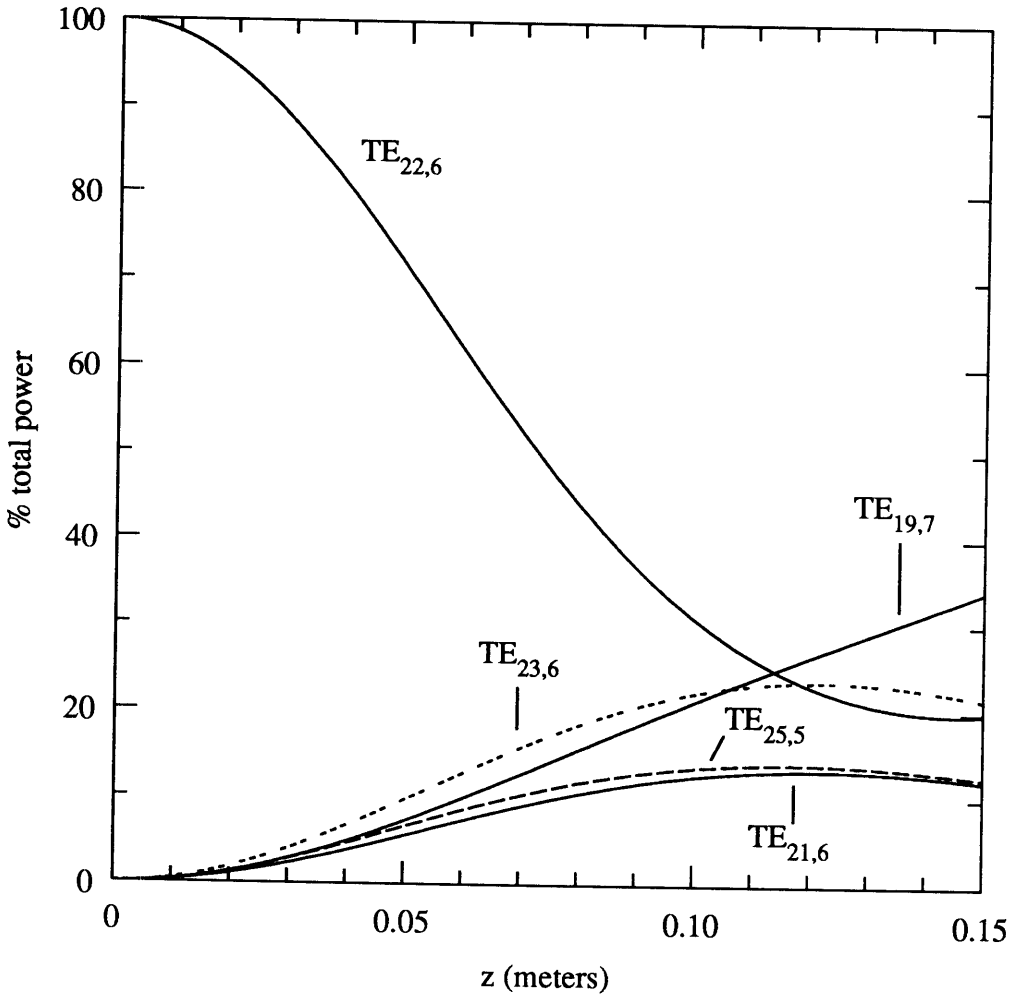

Figure 3.4 Variation of the mode mix along the length of the $TE_{22,6}$ pre-bunching launcher.

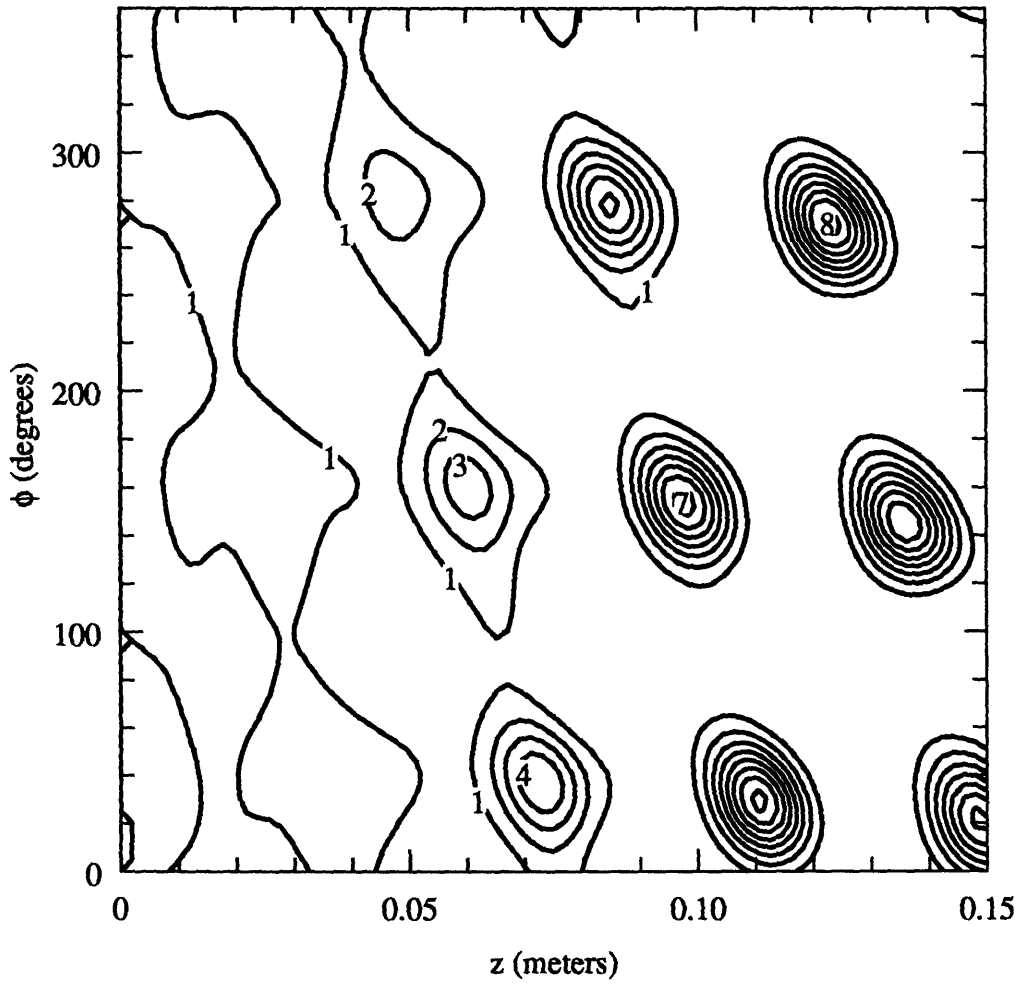

Figure 3.5 Field intensity ($|E_r|^2$) on the pre-bunching launcher wall. Lines of constant intensity, normalized to the uniform intensity of the pure $TE_{22,6}$ rotating mode, are plotted in steps of 1.

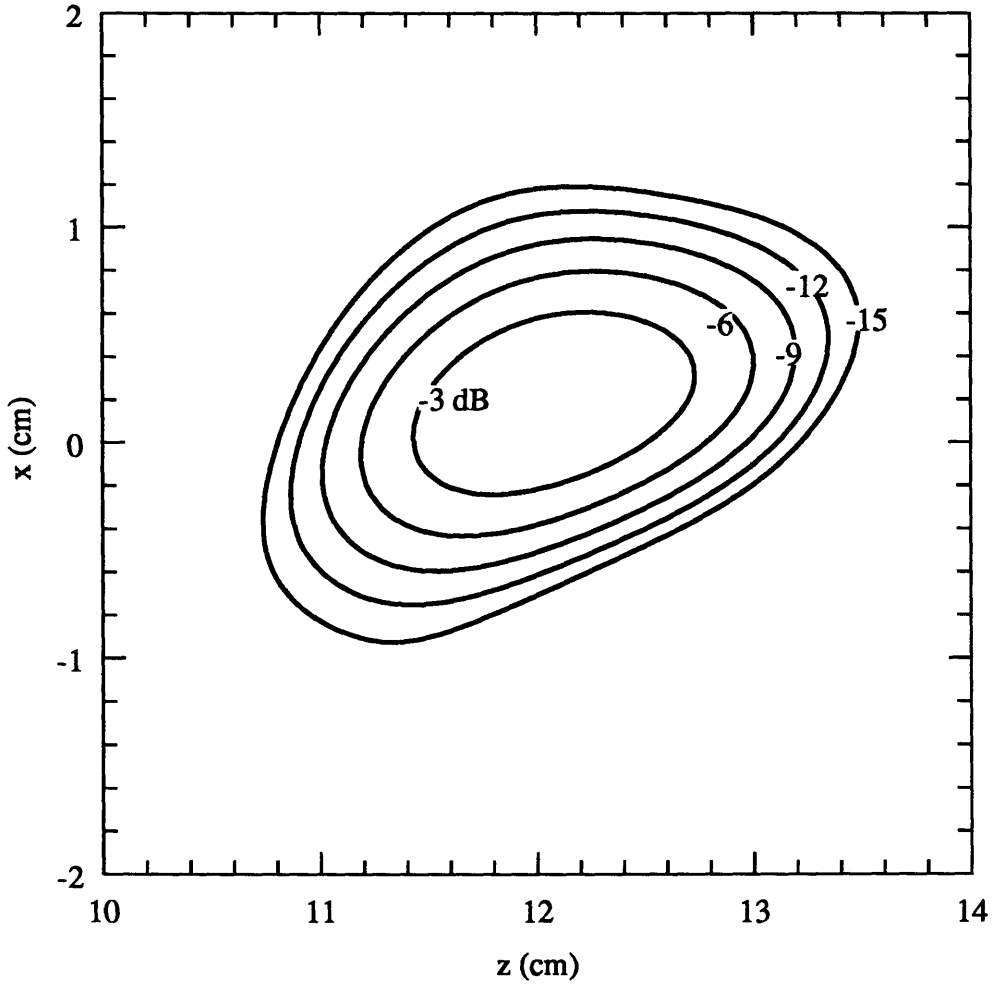

Figure 3.6 Fields on the step cut aperture as calculated by coupled mode theory. Lines of constant $|E_x|^2$ are shown in dB below peak intensity.

to the beam propagation direction, and $\hat{x}$ is normal to the $\hat{y}$ and $\hat{z}$ directions. The origin of the launcher coordinate system is chosen such that $z = 0$ corresponds the start of the rippled wall pattern on the pre-bunching launcher, and $x = 0$ and $y = 0$ correspond to the waveguide axis. In a second coordinate system, the beam coordinate system, $\hat{d}$ is the direction parallel to the propagation direction, $\hat{x}$ is unchanged from the launcher coordinated system, and $\hat{z}'$ the direction normal to both $\hat{d}$ and $\hat{x}$. The two coordinate systems are related by the bounce angle, θ_B. As is evident from Fig. 3.7, $d = \frac{y}{\sin\theta_B}$.

The Stratton-Chu vector diffraction theory was used to calculate the near field pattern on a plane perpendicular to the propagation direction of the launched beam, as shown in Fig. 3.7. This near field launcher pattern is determined by using the aperture fields, calculated by the coupled mode theory, as the source terms in the Stratton-Chu formula (Eqs. 2.21 and 2.22). With the exception of the new source terms, the Stratton-Chu equation used in this analysis is identical to that used in the Vlasov-type converter analysis.

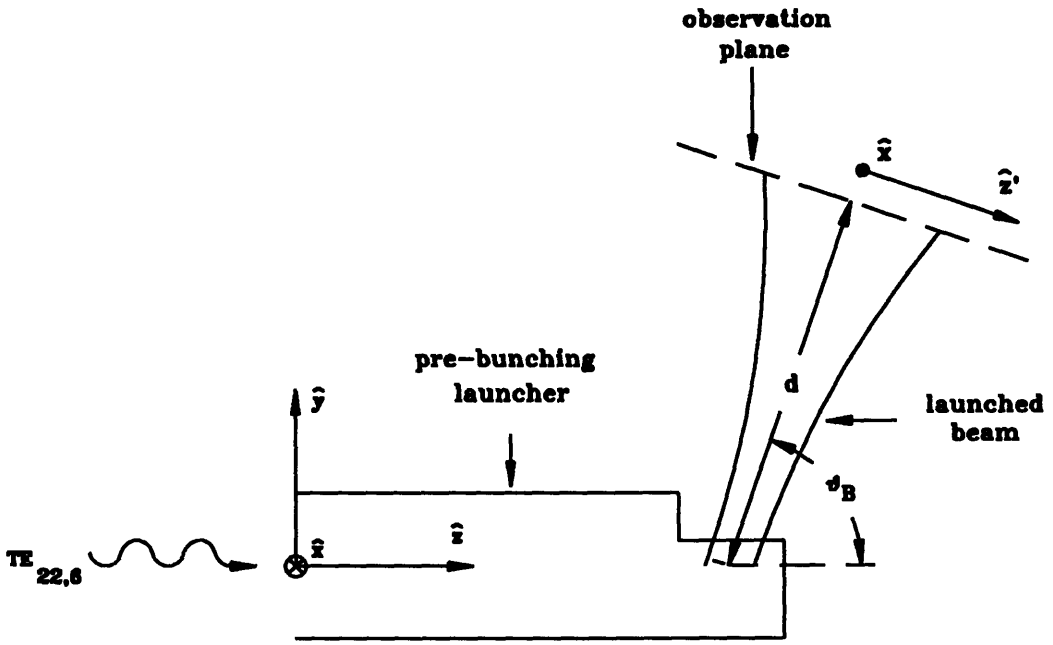

Figure 3.7 Configuration of pre-bunching launcher and observation plane for the vector diffraction theory analysis of radiated beam.

Figure 3.8 shows the Stratton-Chu theory prediction of near field pattern from the launcher on a plane centered at d = 4.78 cm. Theoretical near field pattern calculations, such as that shown in Fig. 3.8, were made in planes at many different d values in an effort to study the expansion of the beam launched from the pre-bunching section. The theoretical

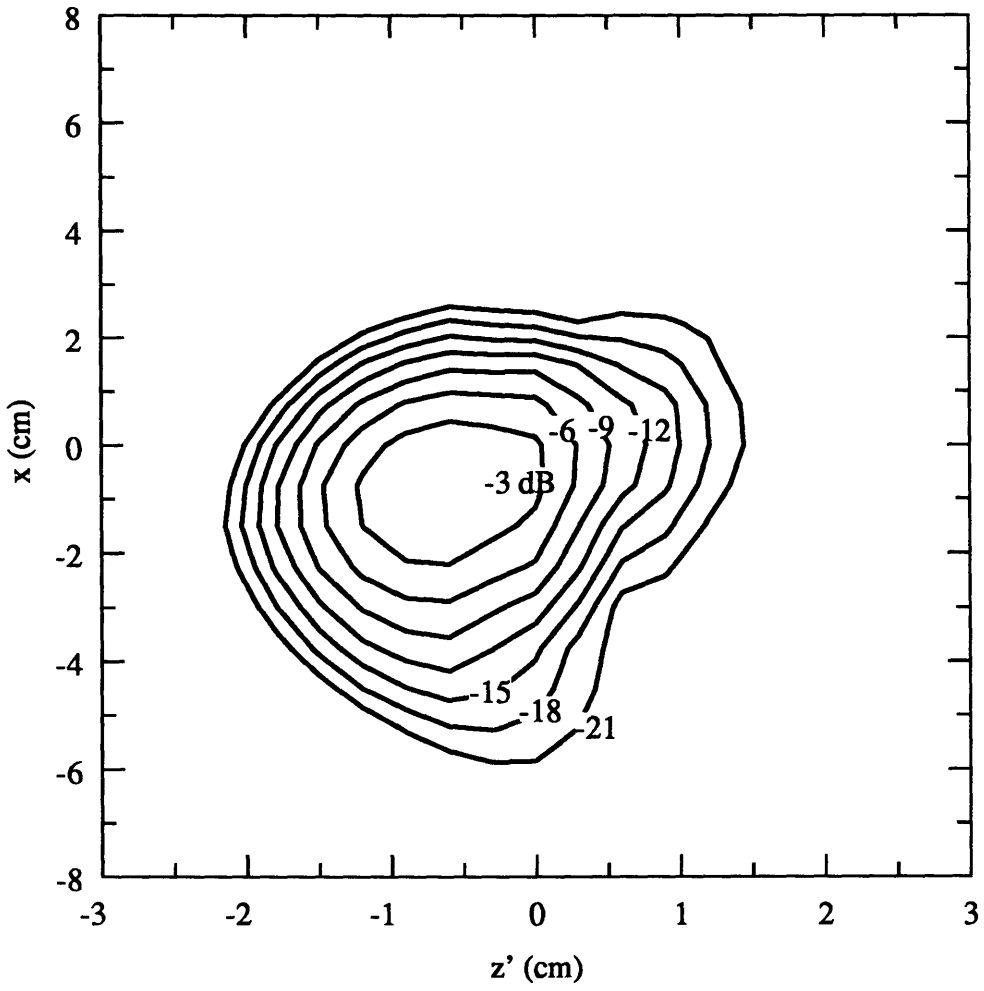

Figure 3.8 Near field vector diffraction theory prediction of the beam radiated from the pre-bunching launcher. The center of the observation plane is at d = 4.78 cm and the plane is perpendicular to the propagation direction of the incoming beam. Lines of constant $|E_x|^2$ are shown in dB below peak intensity.

predictions for the horizontal ($\hat{z}'$) and vertical ($\hat{x}$) expansions are shown in Figs. 3.9 and 3.10, respectively. Also plotted in Figs. 3.9 and 3.10 are the theoretical expansions for an elliptic fundamental Gaussian beam with waists $w_{0z'}$ = 0.9 cm and w_{0x} =0.19 cm. As is indicated in Figs. 3.9 and 3.10, the Stratton-Chu diffraction theory predicts that the beam radiated from the pre-bunching launcher expands in much the same manner as the elliptic Gaussian beam. Because of this, the preliminary design of the focussing reflectors can be made with Gaussian optics theory.

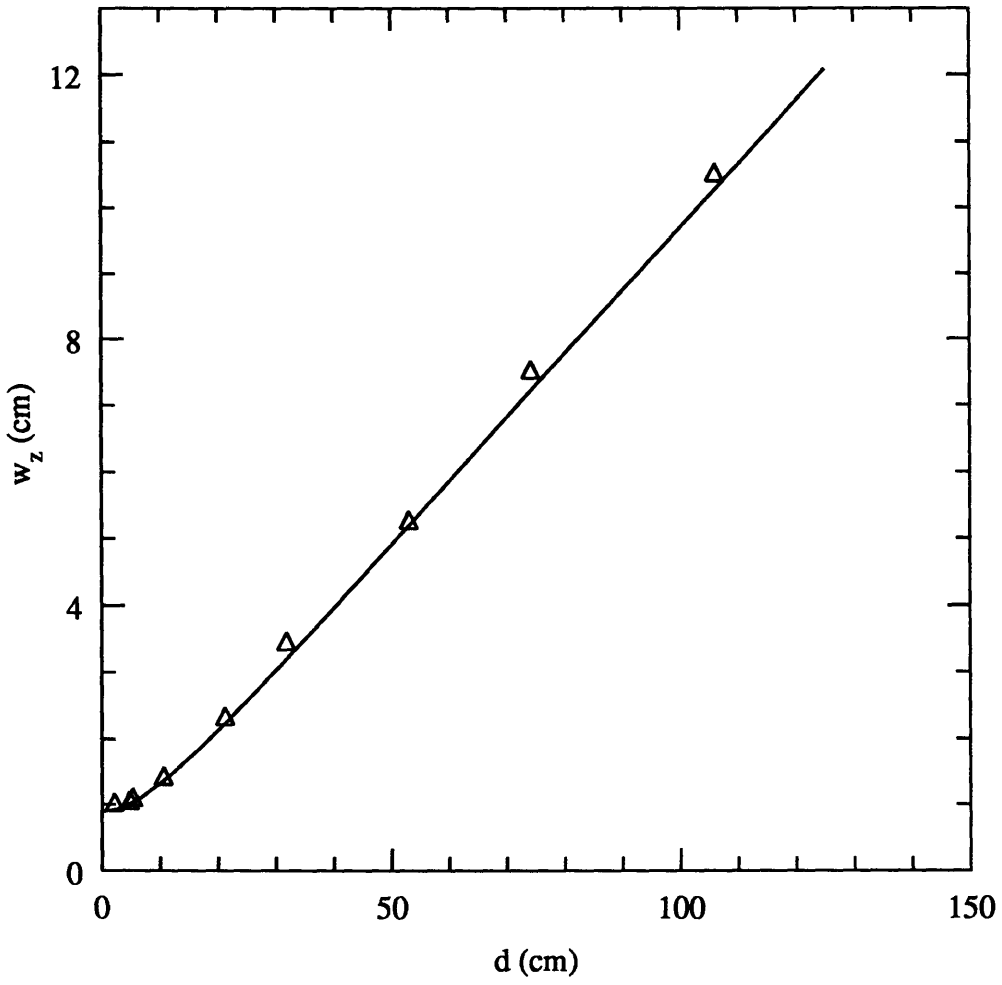

Figure 3.9 Horizontal ($\hat{z}'$) expansion of the beam radiated from the pre-bunching launcher. The triangles show $w_{z'}$ values predicted by the vector diffraction theory and the solid line shows the theoretical expansion for a fundamental Gaussian beam with waist $w_{0z'}$ = 0.9 cm.

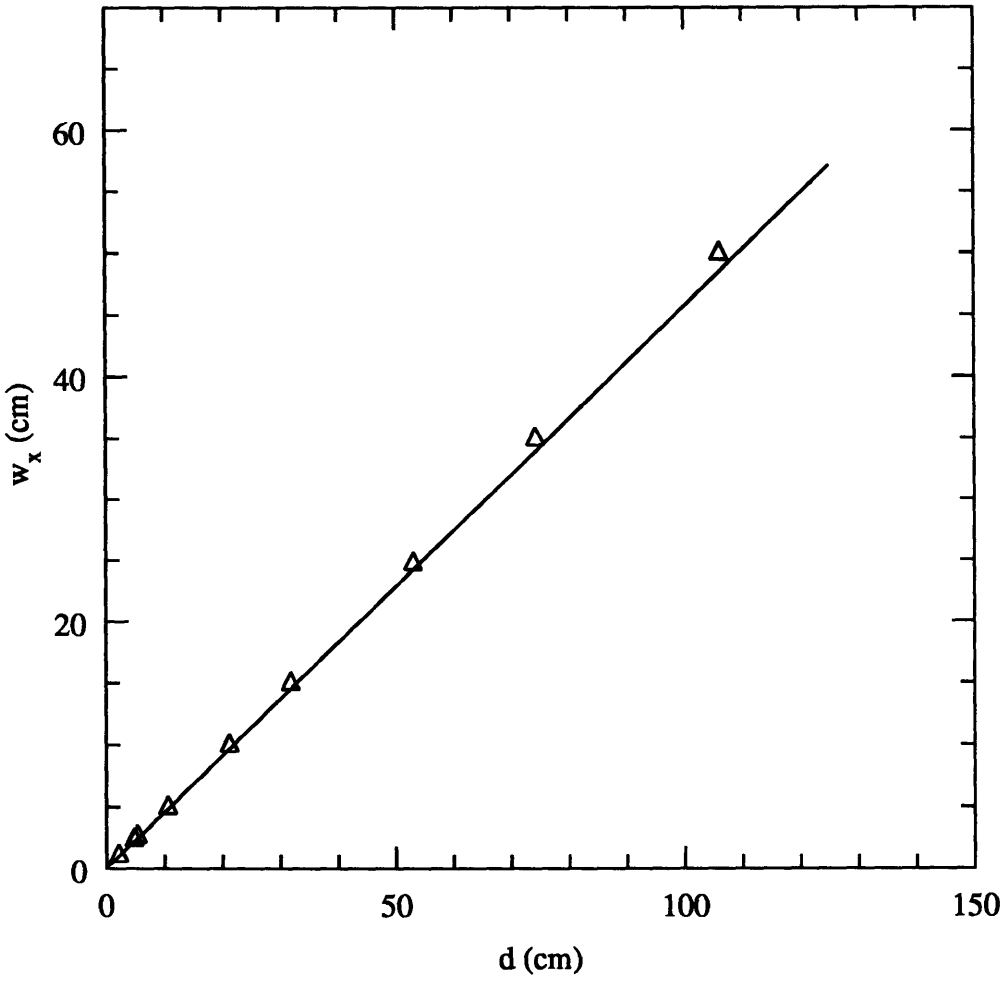

Figure 3.10 Vertical ($\hat{x}$) expansion of the beam radiated from the pre-bunching launcher. The triangles show w_x values predicted by the vector diffraction theory and the solid line shows the theoretical expansion for a fundamental Gaussian beam with waist $w_{0x} = 0.19$ cm.

3.2 Gaussian Optics and Mirror Relay Design

As shown in Figs. 3.9 and 3.10, the beam radiated by the pre-bunching launcher expands in much the same way as an elliptic Gaussian beam with waists $w_{0x} = 0.19$ cm and $w_{0z'} = 0.9$ cm. The purpose of the two mirror transmission line is, thus, to transform the launched beam to the desired fundamental, circular Gaussian beam with waist $w_0 = 0.9$ cm. Because the launched beam behaves like a Gaussian beam, the preliminary reflector design was made using Gaussian optics theory.

The propagation and reflection of a Gaussian beam can be simply described using the q parameter [27][28].

$$\frac{1}{q} = \frac{1}{R} - \frac{j\lambda}{\pi w^2}, \tag{3.30}$$

where R is the radius of curvature of the phase fronts, λ is the free space wavelength of the radiation, j is the imaginary number ($j = \sqrt{-1}$), and w is the beam radius at which the field amplitude decreases to $\frac{1}{e}$ of its on axis value.

The radius of curvature of the phase fronts, R, is given by:

$$\frac{1}{R} = \frac{z}{z^2 + (\frac{\pi w_0^2}{\lambda})^2}, \tag{3.31}$$

where z is the distance of propagation. The beam radius, w,is given by:

$$w^2 = w_0^2 \left[1 + \left(\frac{\lambda z}{\pi w_0^2}\right)^2\right], \tag{3.32}$$

where w_0 is the minimum beam radius, which occurs at $z = 0$.

The Gaussian beam is completely described by the q parameter. Thus, knowing how the q parameter evolves upon propagation and reflection is equivalent to knowing how the Gaussian beam evolves.

The two optical components to be considered are a section of free space of length d and a mirror with radius of curvature R_0. Free space propagation of the beam over length d changes the q parameter from q to q' by the equation [27][28]:

$$q' = q + d \tag{3.33}$$

A mirror with radius of curvature R_0 reflects the beam and alters the radius of curvature of the phase front so the q parameter changes from q to q' by the equation:

$$\frac{1}{q'} = \frac{1}{q} - \frac{2}{R_0} \tag{3.34}$$

With these simple equations for the q parameter and its transformation, the preliminary design of the two mirror transmission line for the $TE_{22,6}$ pre-bunching converter was made. Toroidal mirrors, or mirrors with different vertical and horizontal radii of curvature, are appropriate for converting an elliptic Gaussian beam to a circular beam. The radii of curvature for the two mirrors were calculated according to Eqs. 3.33 and 3.34.

The diffraction and physical optics theories were then used to simulate the launch, reflection, and propagation of the beam through the Gaussian optics mirror transmission line. The results of this theoretical study were used to modify and improve the designs of the two reflectors. Although the radii of curvature of the two mirrors were changed, the toroidal shape of the mirrors was preserved. Table 3.3 summarizes the final design parameters for the mirror relay and the characteristics of the desired output beam. All positions are specified in the launcher coordinate system. In Fig. 3.11, the two mirrors described in Table 3.3 are shown.

	Mirror Center Position	Mirror Curvature	Mirror Size
Mirror1	x=-0.8 cm y=4.3 cm z=12.8 cm	R_{cx}=7.14 cm R_{cz}=370 cm	$\hat{x}$ size = 8.13 cm $\hat{z}$ size = 5.08 cm
Mirror2	x=-0.7 cm y=-3.0 cm z=17.9 cm	R_{cx}=85.55 cm R_{cz}=23.89 cm	$\hat{x}$ size = 6.99 cm $\hat{z}$ size = 6.99 cm
	Output Beam		
	w_{0x}=0.9 cm at y=10 cm w_{0z}=0.9 cm at y=10 cm		

Table 3.3 Design parameters for the $TE_{22,6}$ pre-bunching launcher mirror relay.

mirror1

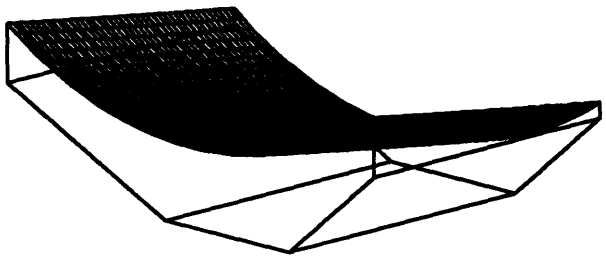

1.98 in. x 3.2 in.

mirror2

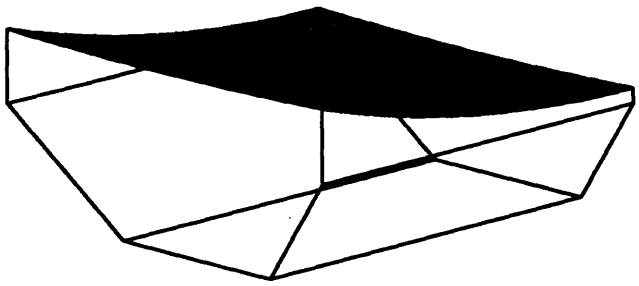

2.72 in. x 2.75 in.

Figure 3.11 The two reflectors of the open mirror transmission line for the $TE_{22,6}$ pre-bunching mode converter.

The diffraction theory predictions of the fields on the reflectors, calculated in the launcher coordinate system, are shown in Figs. 3.12 and 3.13. In Figs. 3.12 and 3.13, lines of constant $|E_x|^2$ are shown in dB below peak intensity. The peak intensity in the cross polarization, E_z, is < -25 dB below the peak of the E_x intensity.

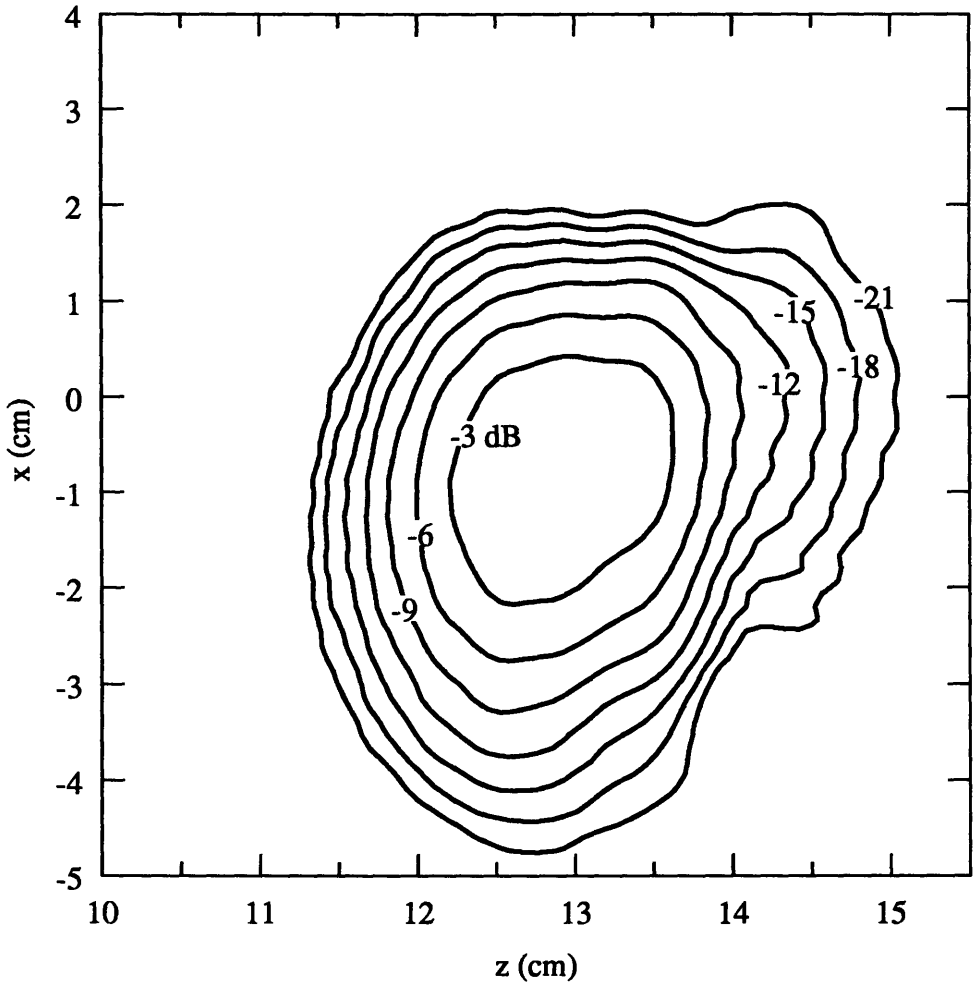

Figure 3.12 Diffraction theory prediction of fields incident on mirror 1, calculated in the launcher coordinate system. Lines of constant $|E_x|^2$ are shown in dB below peak intensity.

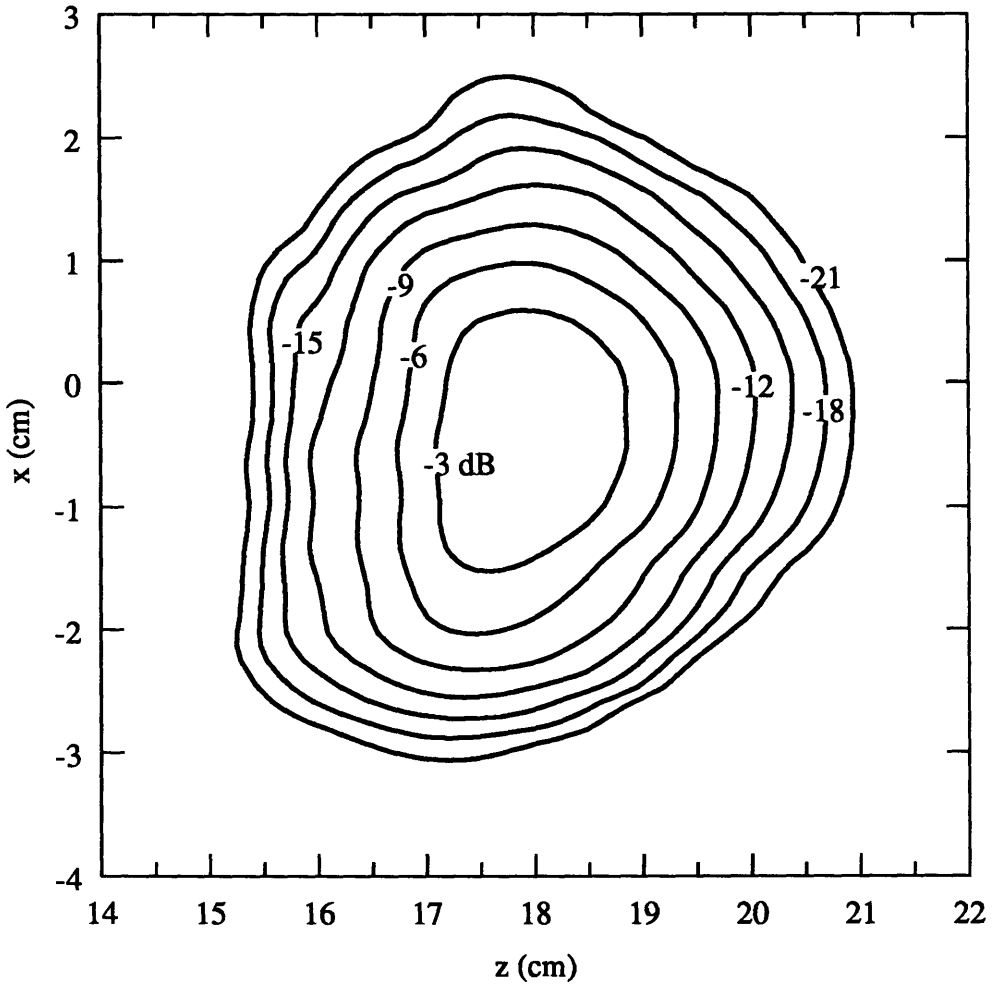

Figure 3.13 Diffraction theory prediction of fields on incident mirror 2, calculated in the launcher coordinate system. Lines of constant $|E_x|^2$ are shown in dB below peak intensity.

The diffraction and physical optics theories were also used to predict the beam at the output of the mirror relay. Figure 3.14 shows the configuration of the launcher, mirrors, and observation plane under consideration. As indicated in Fig. 3.14, the near field beam pattern was calculated on planes perpendicular to the direction of propagation at distances d, where $\hat{d}$ is in the direction of propagation. Once again, the observation plane extends in the $\hat{x}$ and $\hat{z}'$ directions.

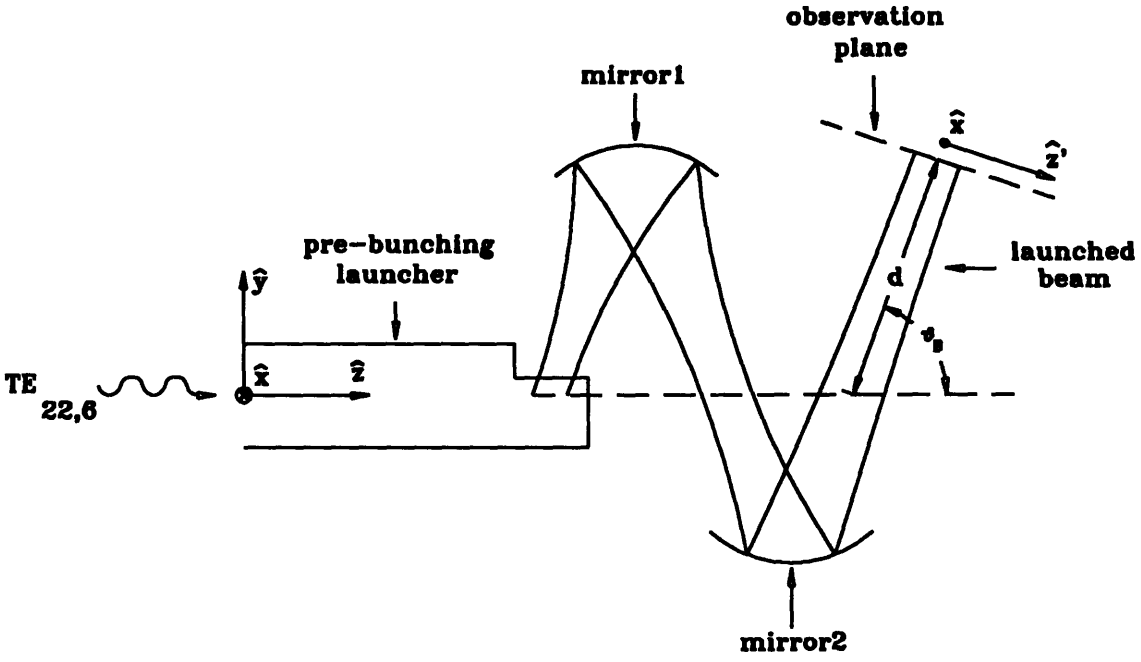

Figure 3.14 Configuration of pre-bunching launcher, two mirror relay, and observation plane for diffraction theory analysis of full converter system.

Figure 3.15 shows the diffraction theory prediction of the beam radiated from the mirror transmission line in the plane of the beam waist, y = 10 cm, which corresponds to the distance d = 10.6 cm. In this plane, the diffraction theory predicts a beam with a Gaussian-like profile and waists $w_{0x} = w_{0z'} = 0.9$ cm, the design value of the output beam waist. Figures 3.16 and 3.17 show the diffraction theory calculations of phase on vertical (Fig. 3.16) and horizontal (Fig. 3.17) cuts through the center of the pattern shown in Fig. 3.15. For a perfect Gaussian beam, the phase fronts are flat at the position of the waist. As seen if Figs. 3.16 and 3.17, the calculated phase fronts are constant to within $\pm 3\%$, indicating that the beam formed by the converter is a good approximation of a Gaussian beam.

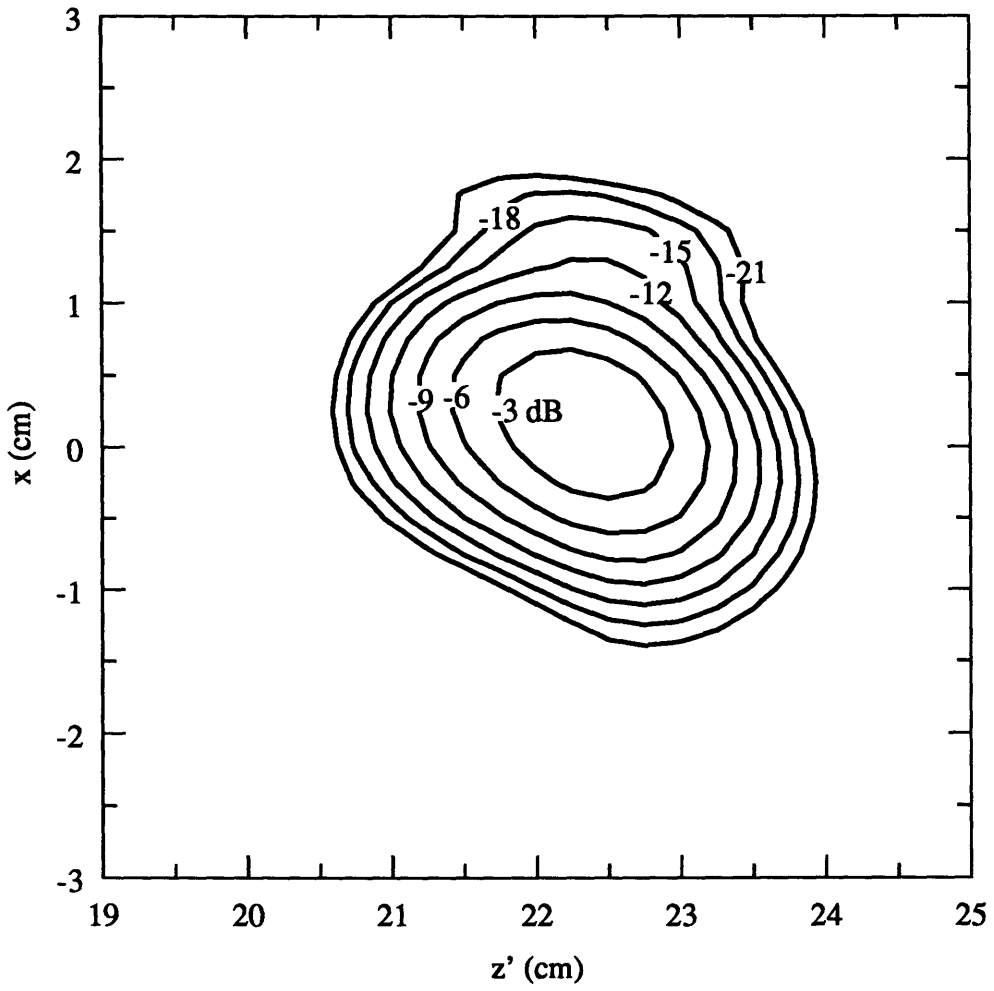

Figure 3.15 Diffraction theory prediction of the beam at the output of the pre-bunching converter. The pattern was calculated on a plane perpendicular to incoming beam at $d = 10.6$ cm. Lines of constant $|E_x|^2$ are shown in dB below peak intensity.

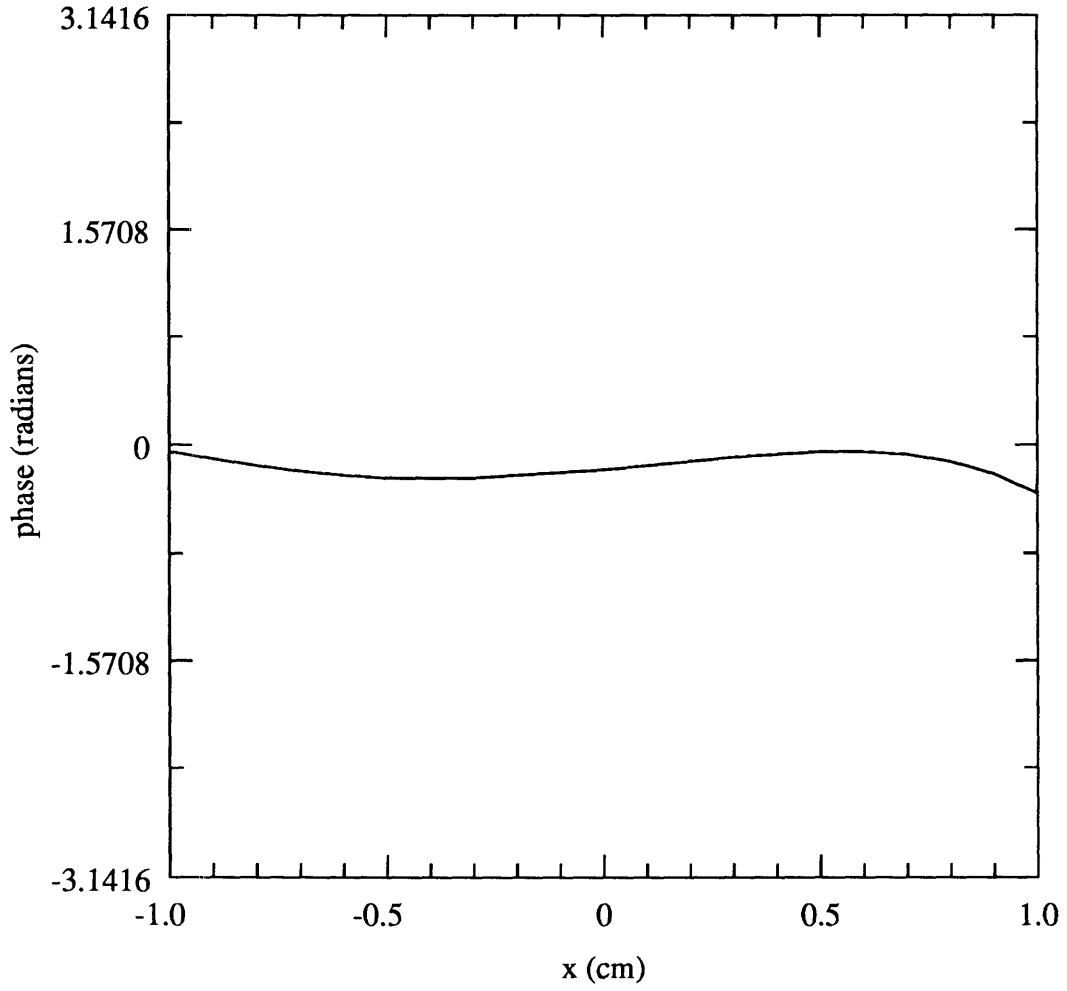

Figure 3.16 The phase along a vertical cut through the center of the output beam at the waist, d = 10.6 cm.

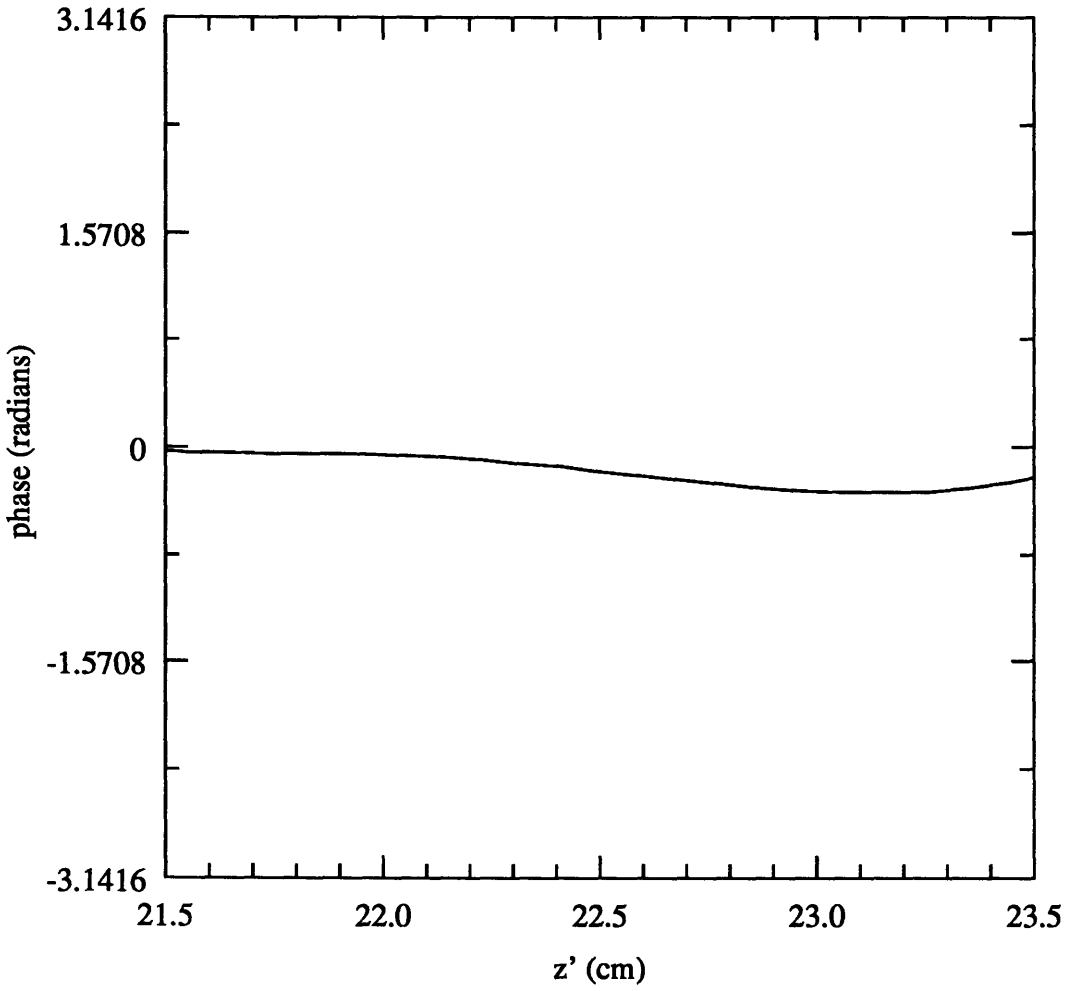

Figure 3.17 The phase along a horizontal cut through the center of the output beam at the waist, $d = 10.6$ cm.

In an effort to study the output beam expansion, the physical optics code was used to calculate the beam pattern on planes at several values of d. Figure 3.18 shows the horizontal and vertical beam waists plotted as a function of d. Figure 3.18 indicates that the output beam generated by the mode converter expands like a fundamental circular Gaussian beam with waists $w_{0x} = w_{0z'} = 0.9$ cm. The calculated expansion is consistent with the nearly flat phase fronts calculated at $y = 10$ cm, shown in Figs. 3.16 and 3.17.

Thus, as shown in Figs. 3.15-3.18, Stratton-Chu and physical optics theories predict that the two mirror relay will convert the beam radiated from the pre-bunching launcher to a fundamental circular Gaussian beam with a waist $w_{0x} = w_{0z'} = 0.9$ cm at $y = 10$ cm.

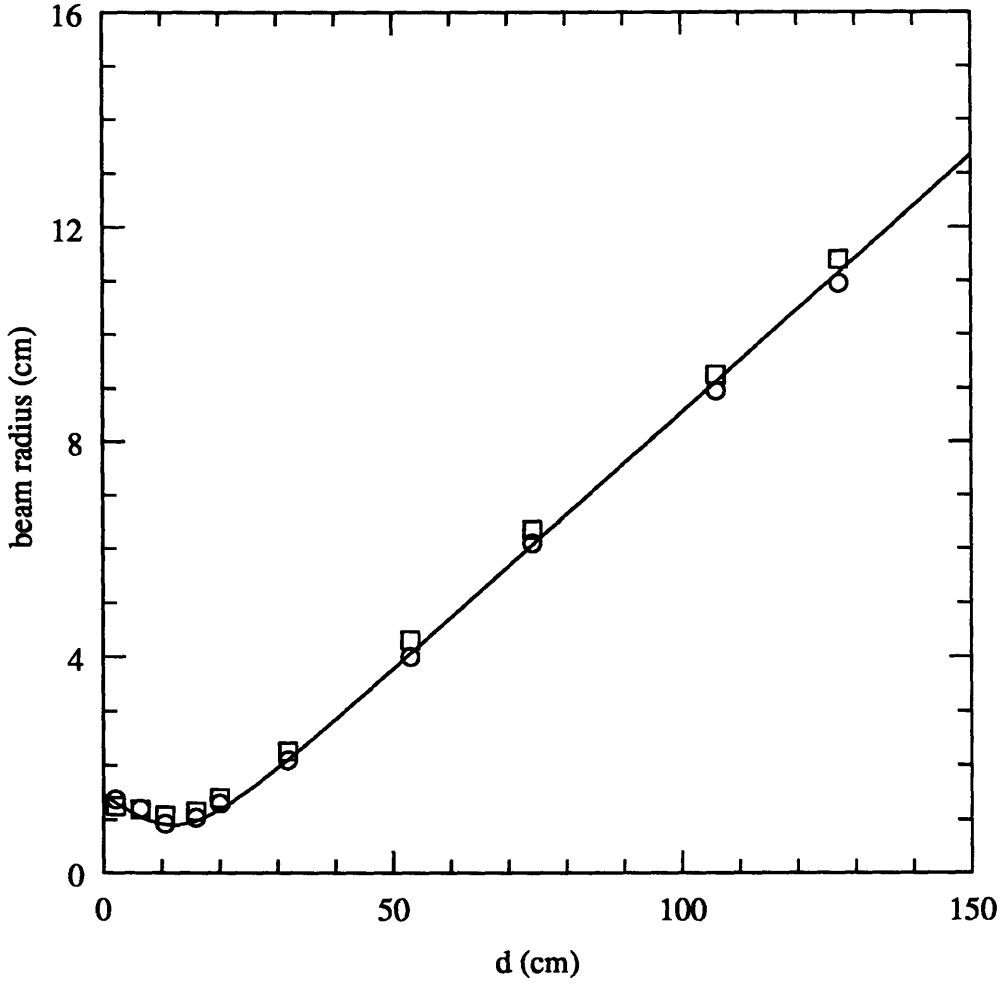

Figure 3.18 Vertical ($\hat{x}$) and horizontal ($\hat{z'}$) expansion of the beam at the output of the pre-bunching converter (launcher and two mirror relay). The squares indicate w_x values predicted by diffraction theory and the circles indicate the diffraction theory predictions for $w_{z'}$. The solid line shows the theoretical expansion for a fundamental circular Gaussian beam with waist $w_0 = 0.9$ cm at a value $d = 10.6$ cm.

3.3 Design of Beam Splitting Mirror Relay

The vacuum window is a limiting component in determining the output power capability of a high power, high frequency gyrotron oscillator. Although novel windows with improved power handling capabilities are currently being investigated [29–31], it may prove advantageous to divide the radiation produced by the gyrotron and direct it through two vacuum windows, which would serve to reduce the power handling requirements of each window by a factor of two. With this in mind, four additional reflectors were designed to split the fundamental Gaussian beam formed by the launcher and two mirror relay into two fundamental Gaussian beams, each containing approximately half the total power. The launcher, two mirror relay (mirrors 1 and 2), and beam splitting relay (mirrors 3–6) are shown in Fig. 3.19.

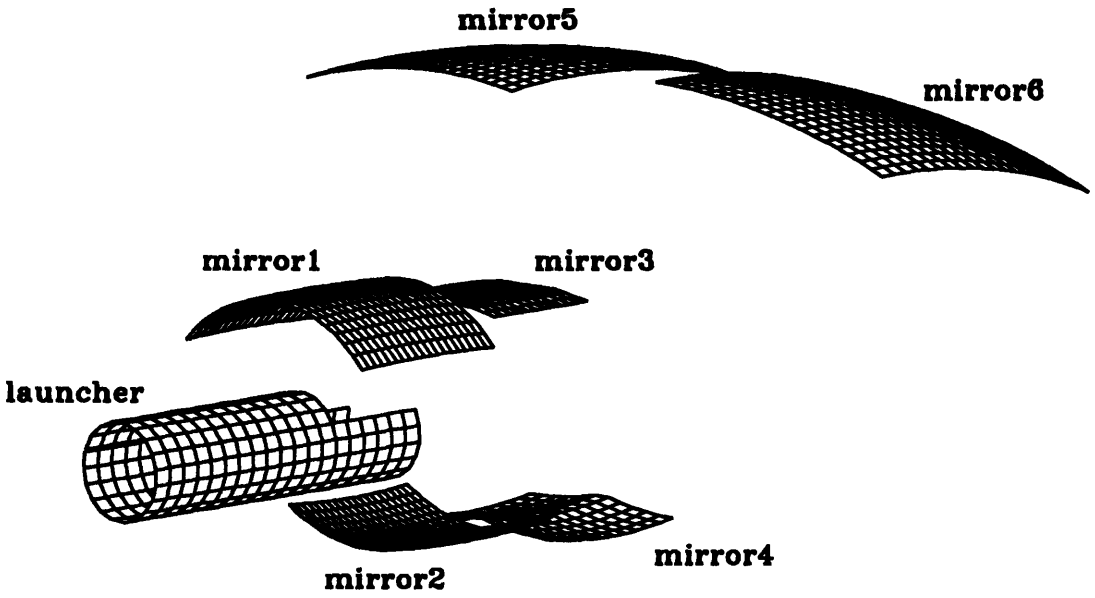

Figure 3.19 Schematic of the $TE_{22,6}$ pre-bunching launcher, the two mirror transmission line (mirrors 1 and 2) and the beam splitting transmission line (mirrors 3 and 4).

The preliminary design of the beam splitting mirror relay was made with geometric optics and Gaussian optics theories. The vector diffraction theory, described in the preceding sections, was then used to propagate the beam through the beam splitting relay and predict the final dual beam output. Based on the diffraction theory prediction, the mirrors were modified and improved, and the final design of the mirror relay was reached. The surfaces of the beam splitting mirrors are toroidal and sinusoidal shapes. Because of the simple shapes, the mirrors are inexpensive, easy to manufacture, and relatively easy to align.

Geometric optics suggests that a uniform field distribution can be transformed to a double peaked distribution upon reflection from a sinusoidally shaped surface. Similarly, the Gaussian beam formed by the two mirror transmission line, with w_0 = 0.9 cm, can be split into two beams upon reflection from a mirror with a sinusoidal amplitude perturbation. Mirror 3, shown in Fig. 3.20, is flat in the longitudinal direction ($\hat{z}$). In the transverse direction ($\hat{x}$), a $\frac{3}{2}$ period sinusoidal ripple with amplitude 0.0305 cm is superimposed on a cylindrical surface with radius of curvature R_{cx} = 20.32 cm. The mirror is centered at position x = 0.0 cm, y = 5.0 cm, z = 20.8 cm, where the coordinate system is shown in Fig. 3.14. The Gaussian beam formed by the two mirror relay is incident on mirror 3 and the diffraction theory prediction of the pattern at the output of mirror 3 is shown in Fig. 3.21. Note that the simple sinusoidal ripple on mirror 3 gives rise to significant beam splitting in the $\hat{x}$ direction.

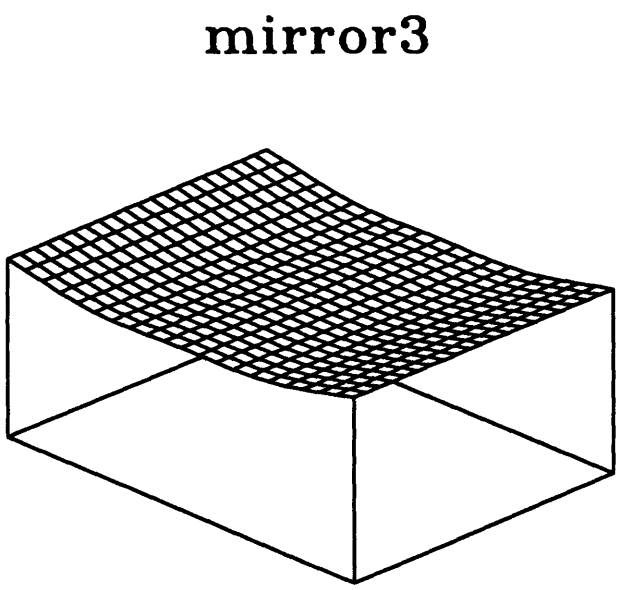

Figure 3.20 Schematic of mirror 3, the mirror that performs initial beam splitting.

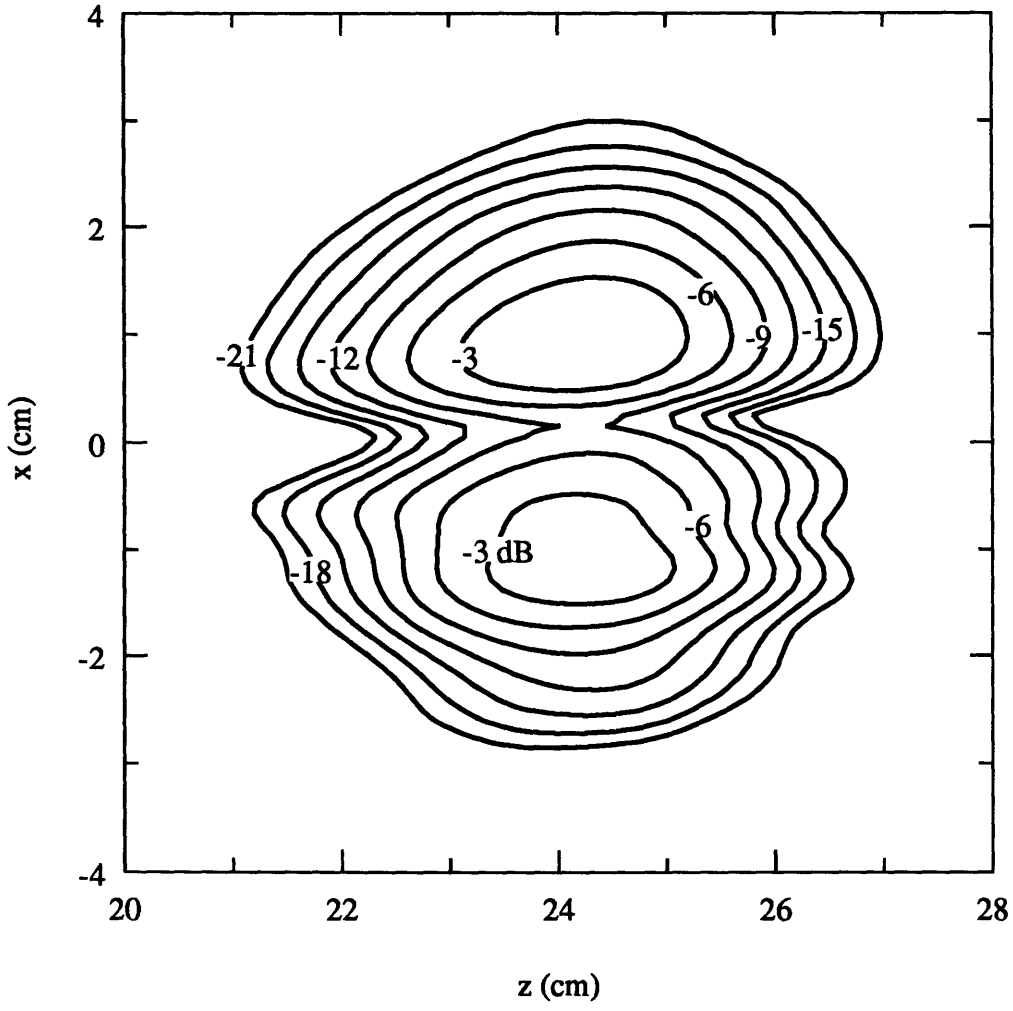

Figure 3.21 Diffraction theory prediction of fields at the output of mirror 3, calculated in the launcher coordinate system. Lines of constant $|E_x|^2$ are shown in dB below peak intensity.

Mirror 4 was designed to complete the beam splitting initiated by mirror 3. As shown in Fig. 3.22, mirror 4 consists of two toroidal surfaces, designed to focus the individual beams, which are angled so as to direct the two beams away from each other. The center of mirror 4 is placed at $x = 0.0$ cm, $y = -5.15$ cm, $z = 24.2$ cm. The two toroidal surfaces are angled $\pm 6^o$ from the $\hat{x}$ axis.

The partially split beam at the output of mirror 3 (Fig. 3.21) is incident on mirror 4 and the vector diffraction theory prediction of the pattern at the output of mirror 4 is shown in Fig. 3.23. Mirror 4 has, thus, completed the beam splitting and produced two elliptic Gaussian-like beams, the upper beam containing 52% of the power and the lower beam containing 48%.

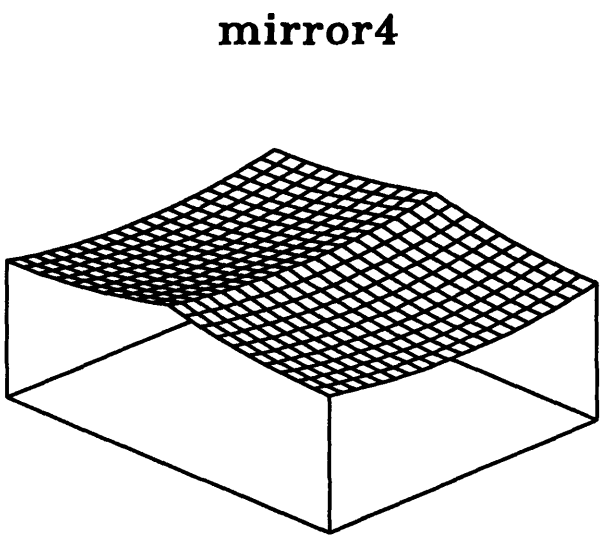

Figure 3.22 Schematic of mirror 4, the mirror that completes the beam splitting.

The final two mirrors, mirror 5 and mirror 6, are toroidal mirrors designed to focus the two elliptic beams into fundamental, circular Gaussian beams. Mirrors 5 and 6, shown in Fig. 3.24, also perform beam steering in two directions. Upon leaving mirrors 5 and 6, the two beams are travelling perpendicular to the waveguide axis and parallel to each other. The diffraction theory prediction of the beams at the output of mirrors 5 and 6 is shown in Fig. 3.25.

In an effort to study the expansions of the beams, theoretical predictions such as the one shown in Fig. 3.25 were made in planes at several values of y. Figure 3.26 shows the diffraction theory predictions of the horizontal and vertical expansions of the two beams. The beam in the positive $\hat{x}$ half plane is referred to as 'beam a' and the beam in the negative $\hat{x}$ half plane is referred to as 'beam b'. The vertical ($\hat{x}$) and horizontal ($\hat{z}$) expansions of

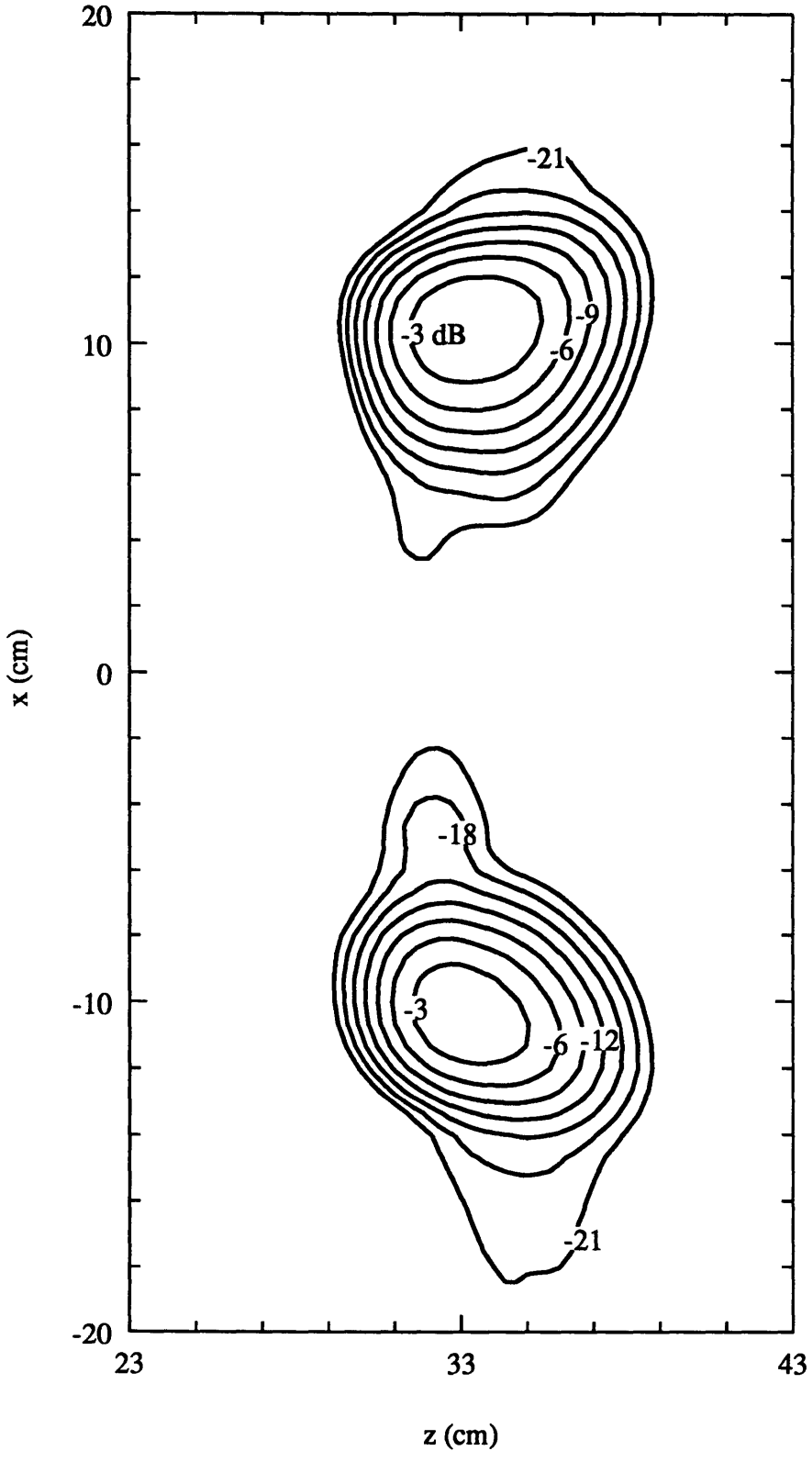

Figure 3.23 Diffraction theory prediction of fields at the output of mirror 4, calculated in the launcher coordinate system. Lines of constant $|E_x|^2$ are shown in dB below peak intensity.

mirror5

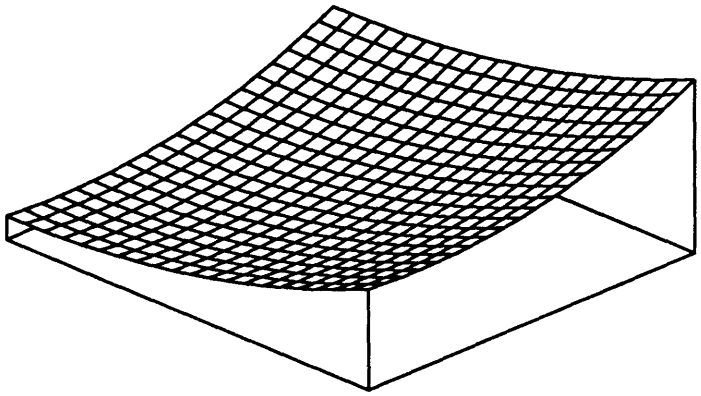

mirror6

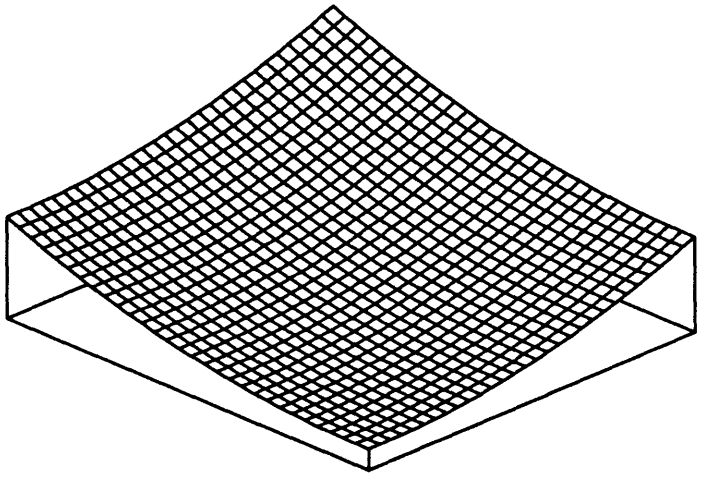

Figure 3.24 Schematic of mirrors 5 and 6, toroidal shaping mirrors.

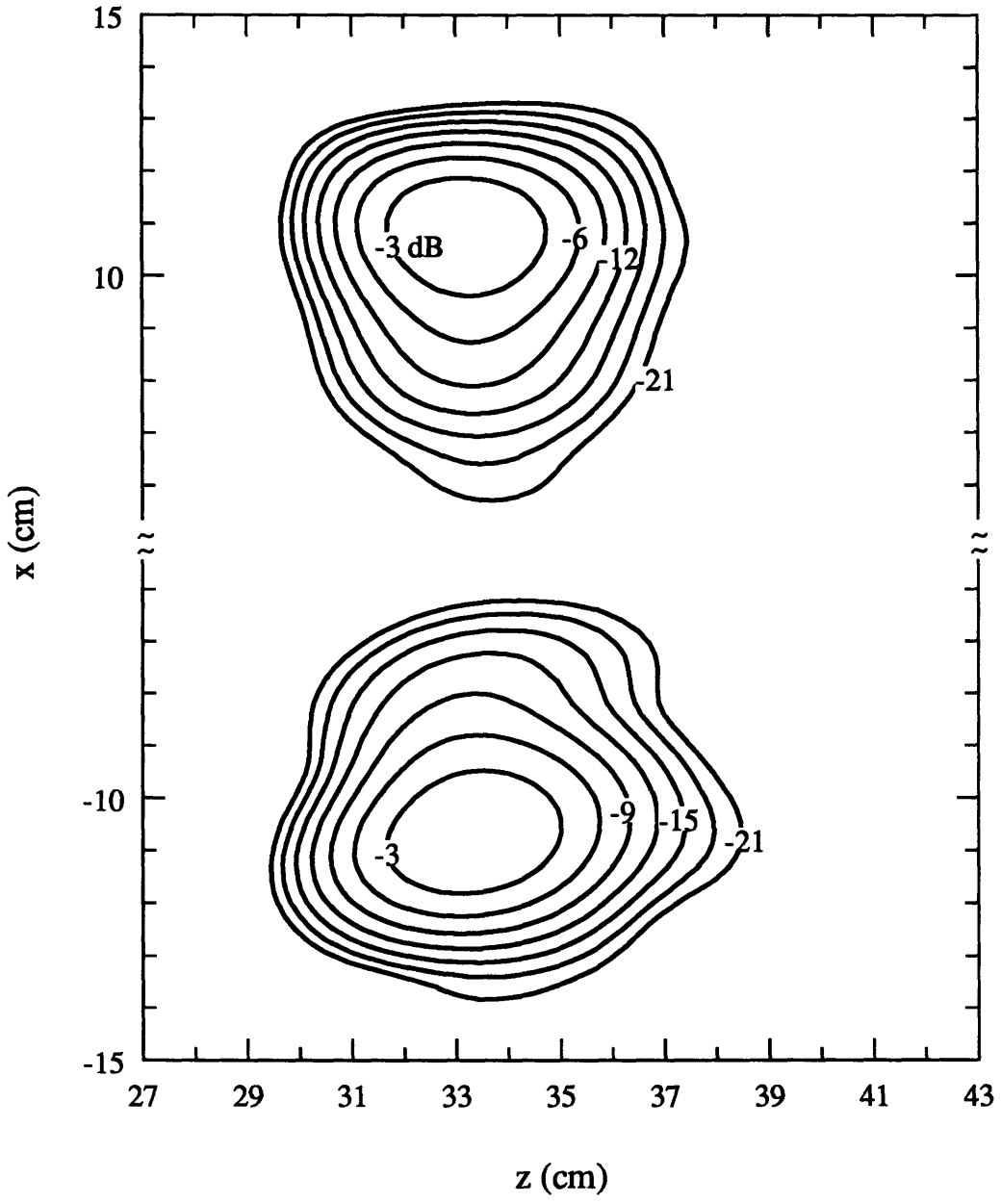

Figure 3.25 Diffraction theory prediction of the dual beam output from mirrors 5 and 6, calculated on a plane perpendicular to the beam propagation path at y =55 cm. Lines of constant $|E_x|^2$ are shown in dB below peak intensity.

both beams are plotted against the theoretical expansion of a fundamental, circular Gaussian beam with waist w_0 = 1.5 cm.

As shown in Fig. 3.26, the vector diffraction theory predicts that the four mirrors in the beam splitting relay transform the incident Gaussian beam into two Gaussian-like beams, each containing approximately half the power. The beam expansions (Fig. 3.26) indicate that the dual beams are expanding in much the same manner as a fundamental Gaussian beam with waist w_0 = 1.5 cm.

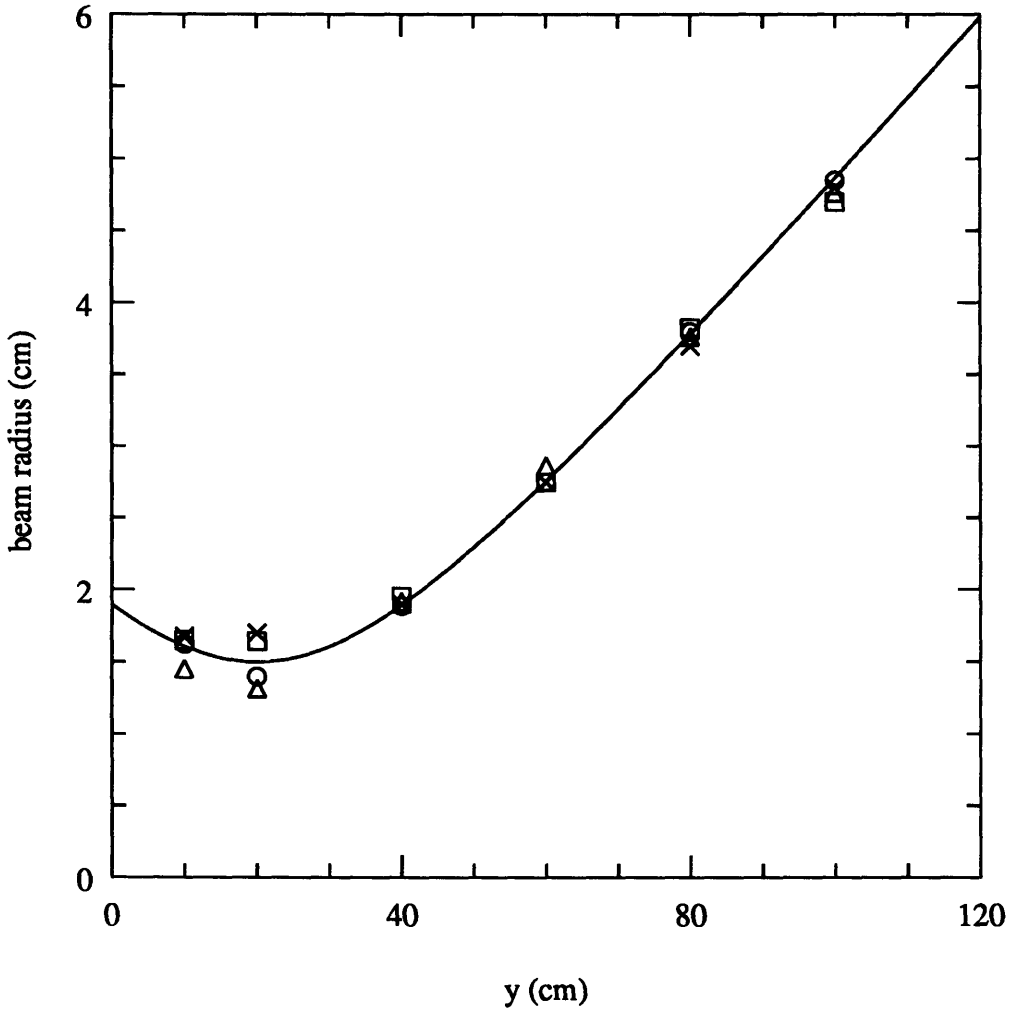

Figure 3.26 Horizontal ($\hat{z}$) and vertical ($\hat{x}$) expansions of the two beams output from the beam splitting mirror relay. The circles indicate w_z for beam a, the upper beam; the squares indicate w_x for beam a; the triangles show w_z for beam b, the lower beam; and the x's show w_x for beam b. The theoretical expansion for the design beam, a fundamental Gaussian beam with waist w_0 = 1.5 cm, is shown with the solid line.

3.4 Pre-Bunching Converter and Beam Splitting Mirror Relay Experiments

The pre-bunching converter described in Tables 3.1 and 3.3 was constructed and experimentally verified. Tests were performed on a megawatt power level, 3μs pulsed gyrotron operating in the $TE_{22,6}$ mode at 110 GHz. The converter was first tested externally, as shown in Fig. 3.27. With the mode converter in the external configuration, it was possible to study the beam radiated from the launcher, as well as the beam at the exit of the two mirror transmission line. Experiments included diode scans of the beam radiated from the pre-bunching launcher, diode scans of the beam at the output of the mirror transmission line, and calorimetric conversion efficiency measurements. The beam form by the external converter was also directed into a 1.25 in. diameter corrugated waveguide, and coupling to the HE_{11} mode was studied.

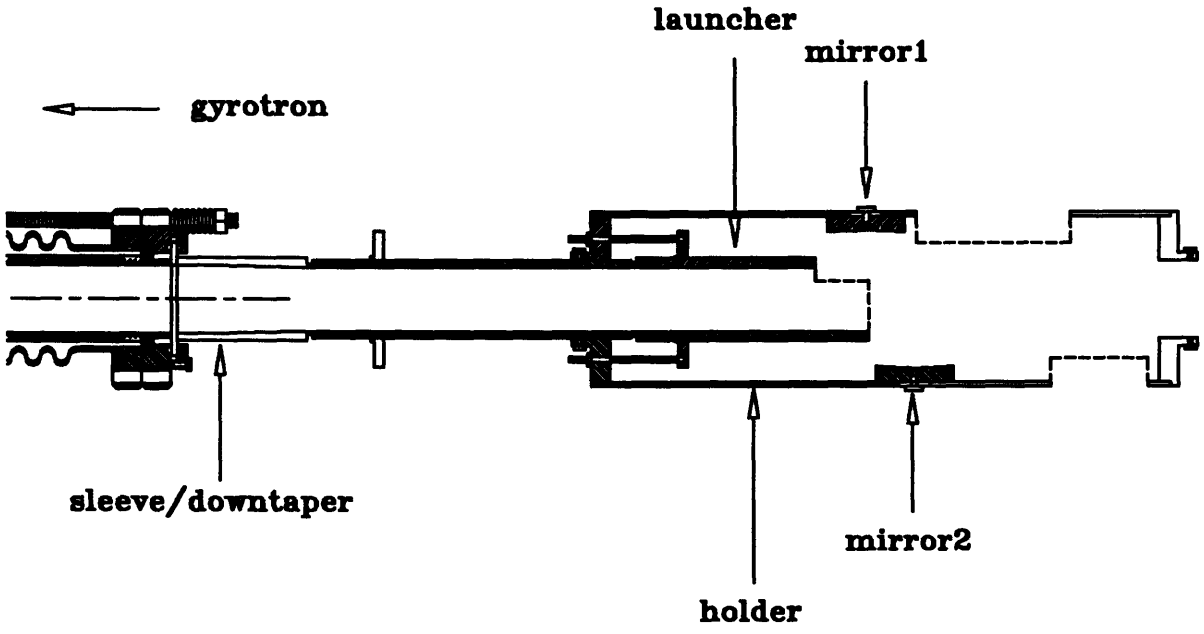

Figure 3.27 Schematic of the pre-bunching mode converter mounted on the external side of the gyrotron vacuum window.

Next, the beam splitting mirror relay, described in the previous section, was added to the launcher and two mirror relay. The test configuration is shown in Fig. 3.28. Experimental verification of the beam splitting mirrors included diode scans of the dual output beam, beam expansion measurements, and calorimetric efficiency measurements.

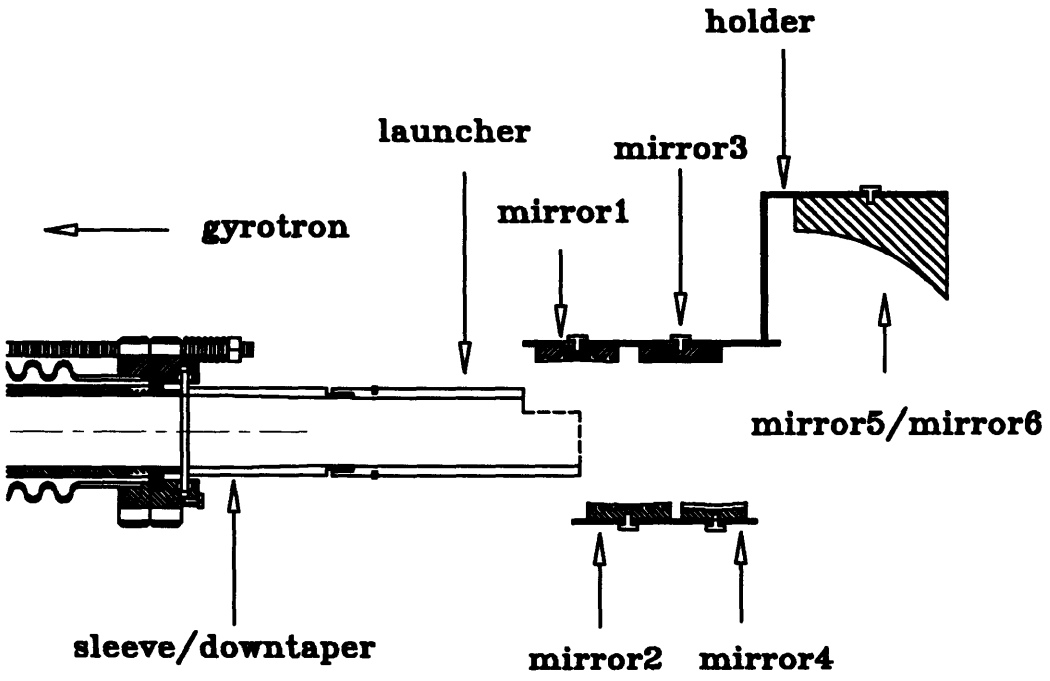

Figure 3.28 Schematic of the pre-bunching launcher, two mirror transmission line (mirrors 1 and 2), and four additional mirrors of the beam splitting transmission line (mirrors 3–6).

Finally, the converter was placed inside the gyrotron vacuum chamber (Fig. 3.29) and another set of experiments was made. With the mode converter inside the gyrotron, only the beam from the full converter (launcher and two mirror relay) could be measured.

For all the beam pattern measurements described below, the receiving unit was comprised of an open ended WR6 waveguide, a precision attenuator, and a WR6 diode detector. In each experiment, the receiving unit was positioned on an optical bench, which was oriented in the direction perpendicular to the incoming beam. The receiving unit was moved in the vertical and horizontal directions and in this way, scans in planes at constant values of propagation distance, d, were made.

Below, the external and internal tests are described and the results are discussed.

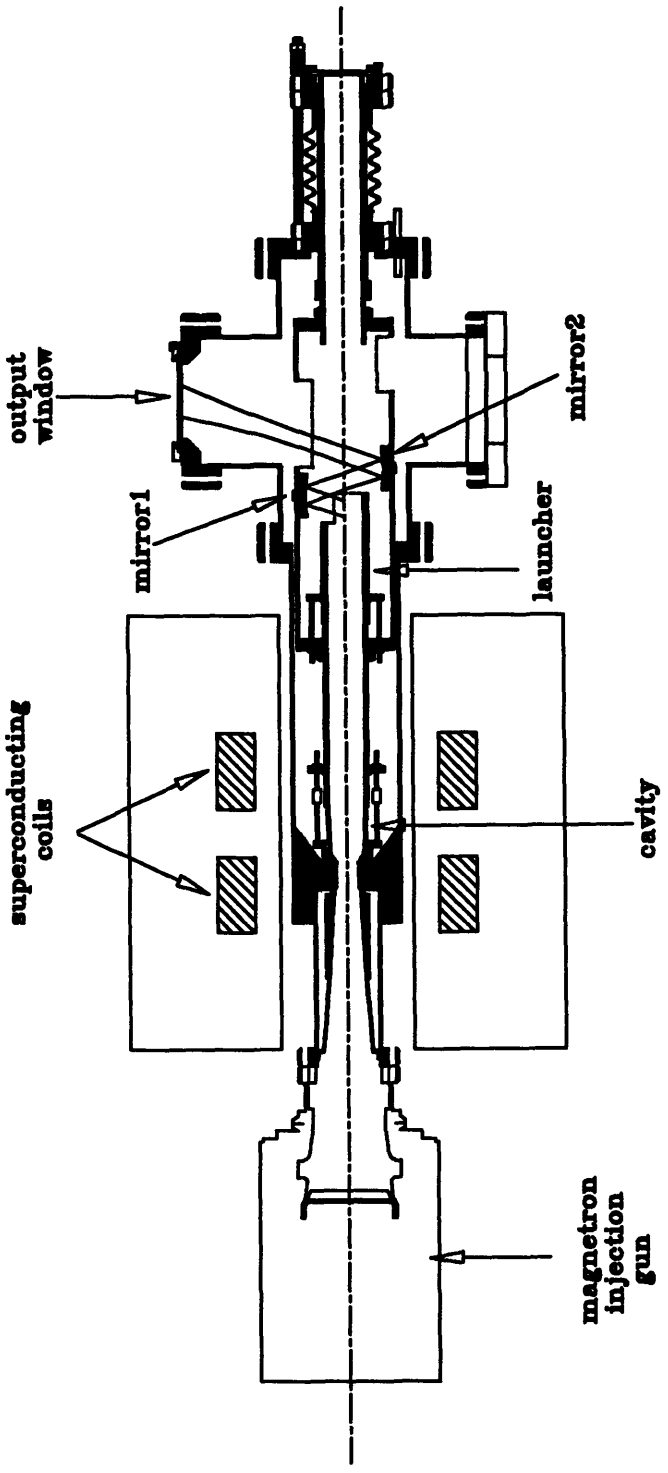

Figure 3.29 Schematic of the pre-bunching mode converter inside the gyrotron vacuum tube.

3.4.1 External Converter Experiments

The configuration of the external converter experiments is shown in Fig. 3.27. Inside the vacuum tube, there is a cylindrical waveguide, R_w = 2.22 cm. The internal waveguide extends to within a few millimeters of the quartz vacuum window. An external waveguide, or sleeve, is positioned on the atmosphere side of the vacuum window and held in place with a collar. The sleeve, which is also a cylindrical waveguide, consists of a short section of radius R_w = 2.22 cm and a linear downtaper to a radius of R_w = 2.1 cm over an axial length of 2.54 cm. The gradual taper was designed to cause a minimum of mode conversion (<0.1%) from the $TE_{22,6}$ mode. The pre-bunching launcher, with mean radius R_w = 2.1 cm, was mounted on the sleeve. As was the case in external Vlasov-type converter testing, the vacuum window automatically produces a discontinuity in the waveguide and provides a mechanism for mode conversion. The external waveguide section was carefully aligned to minimize the mode conversion caused by the disruption of the waveguide wall.

Several experiments were performed to assess the operation of the pre-bunching launcher and the converter as a whole. The experiments, described below, include radiation pattern measurements, calorimetric power measurements, and corrugated waveguide coupling experiments. The four mirrors of the beam splitting transmission line were then added to the launcher and two mirror relay and further radiation pattern and power measurements were made.

3.4.1.1 Measurement of Beam from Launcher

The pre-bunching launcher was mounted on the external sleeve and the near field pattern of the radiated beam was measured. Figure 3.7 shows the configuration for the launched beam measurement. The results of a scan taken at d = 18 cm are shown in Fig. 3.30. Lines of constant $|E_x|^2$ are plotted in dB below peak intensity. The open ended waveguide of the receiving unit was rotated 90° and the peak intensity in the cross polarization ($E_{z'}$) was measured to be <-25 dB from the peak of the E_x intensity.

The measured pattern in Fig. 3.30 shows an elliptic Gaussian-like beam and one additional side lobe with peak intensity 10 dB below the peak of the main lobe. Horizontal and vertical cuts through the center of the pattern were made and the experimental points were compared to theoretical pattern for an elliptic Gaussian beam with waists $w_{0z'}$ = 0.9 cm and w_{0x} = 0.19 cm, as shown in Figs. 3.31 and 3.32, respectively. Figures 3.31 and 3.32 indicate a good match between the measured pattern and the specified Gaussian beam, which is the beam predicted by the Stratton-Chu diffraction theory.

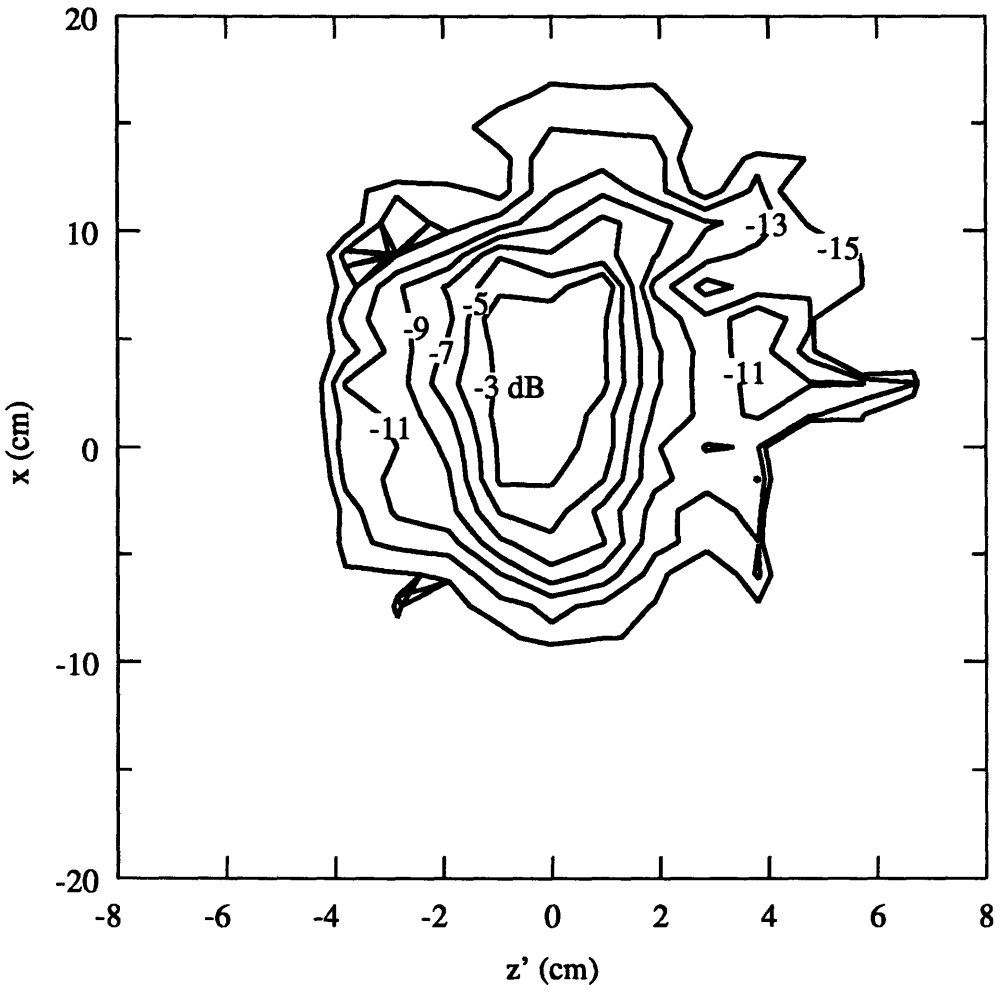

Figure 3.30 Experimental diode scan of the beam radiated from the pre-bunching launcher. The scan was made in a plane perpendicular to the incoming beam at a distance d = 18 cm. Lines of constant $|E_x|^2$ are plotted in dB below peak intensity. The peak intensity in the cross polarization, $E_{z'}$, was measured to be <-25 dB below the peak of the E_x intensity.

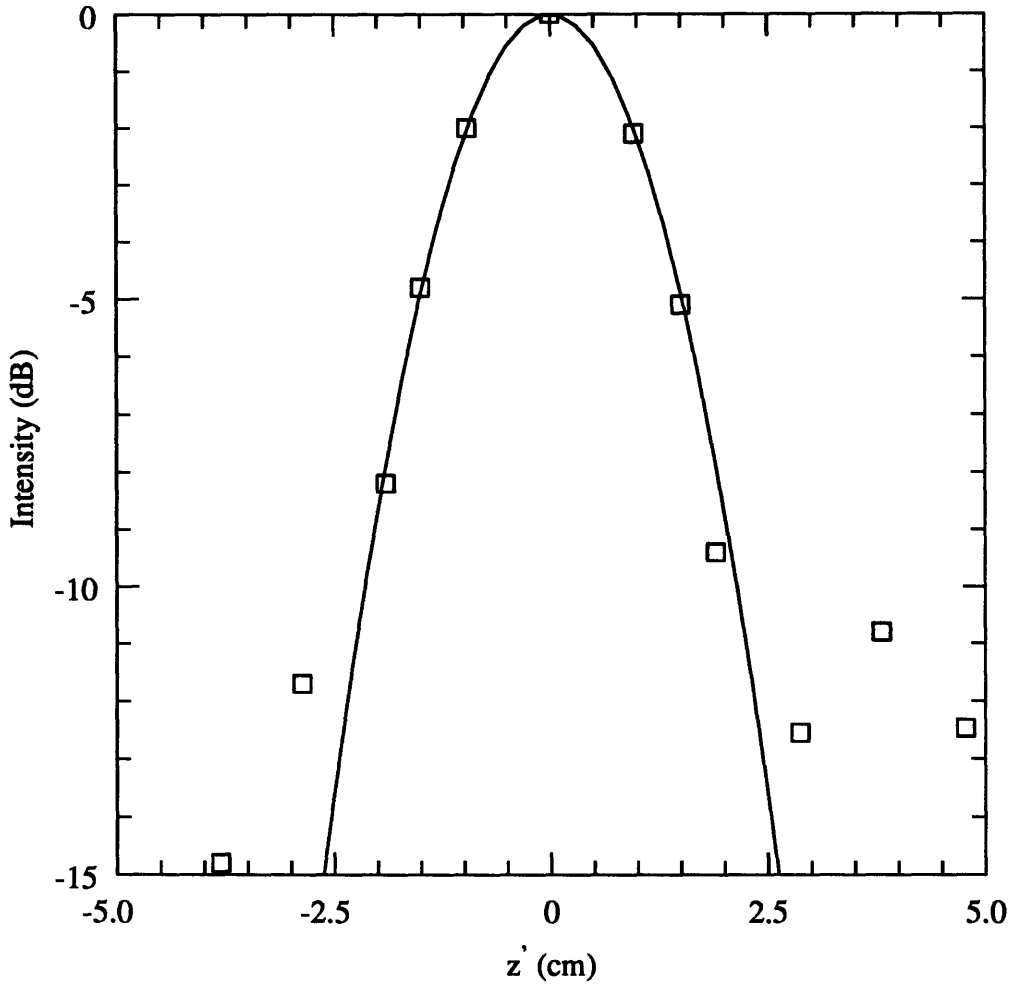

Figure 3.31 Horizontal cut through the center of the beam radiated from the pre-bunching launcher (Fig. 3.30). The squares indicate the experimental values of $|E_x|^2$ measured in a plane at $d = 18$ cm and the solid line shows the theoretical pattern for a Gaussian beam with $w_{0z'} = 0.9$ cm.

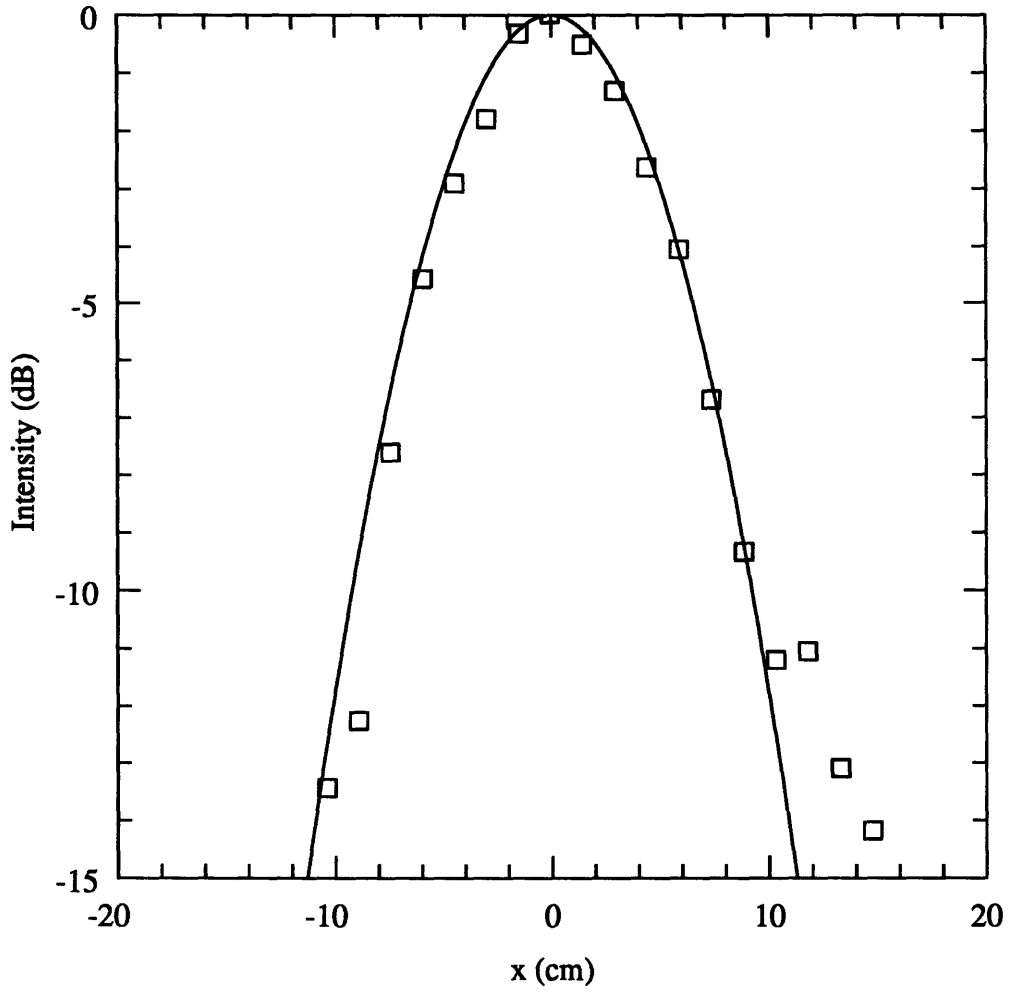

Figure 3.32 Vertical cut through the center of the beam radiated from the pre-bunching launcher (Fig. 3.30). The squares indicate the experimental values of $|E_x|^2$ measured in a plane at $d = 18$ cm and the solid line shows the theoretical pattern for a Gaussian beam with $w_{0x} = 0.19$ cm.

Scans such as that shown in Fig. 3.30 were made in planes at many d values in a effort to measure the horizontal and vertical expansions of the beam radiated by the pre-bunching launcher. The horizontal ($\hat{z}'$) and vertical ($\hat{x}$) beam radii are plotted as a function of beam propagation distance, d, in Figs 3.33 and 3.34. Also plotted in Figs. 3.33 and 3.34 are the Stratton-Chu theory predictions of beam radii and the theoretical expansions for an elliptic Gaussian beam with waists w_{0x} =0.19 cm and $w_{0z'}$ =0.9 cm. Figures 3.33 and 3.34 show good agreement between the measured beam expansions and both the Gaussian optics theory and vector diffraction theory predictions.

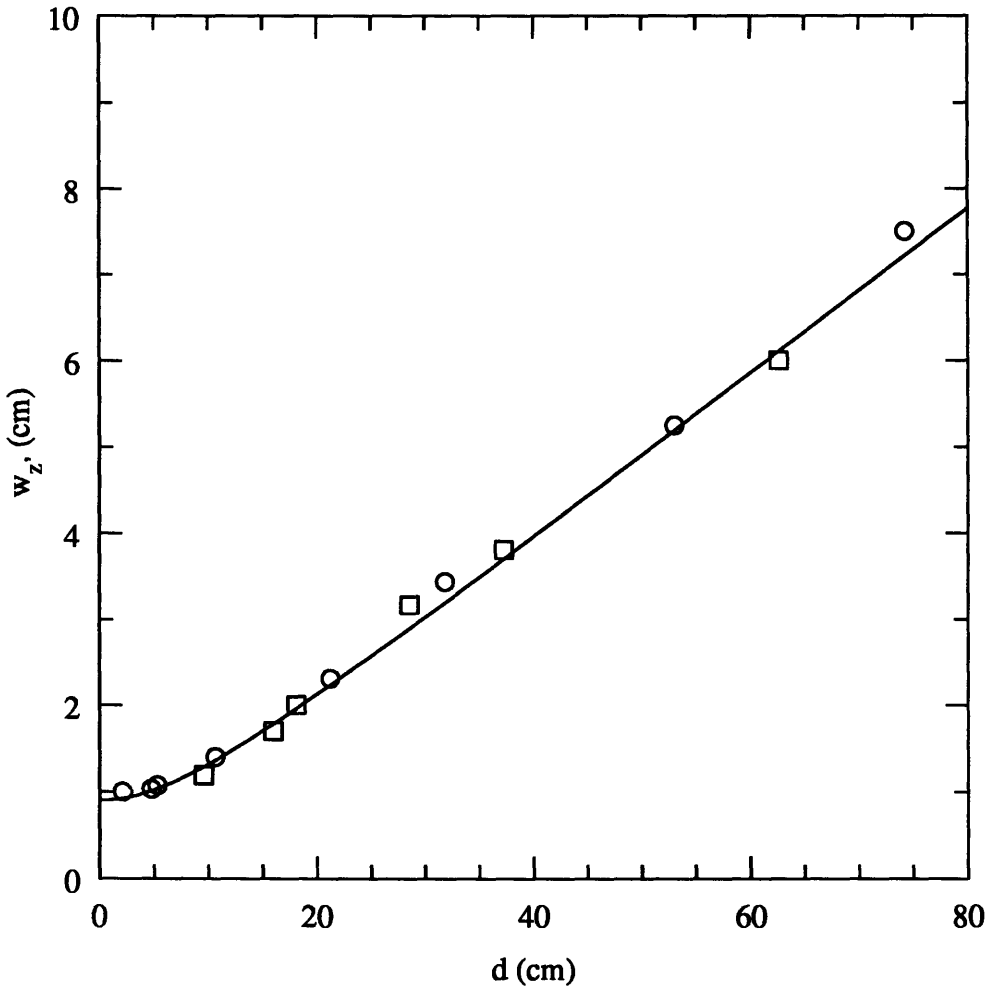

Figure 3.33 Horizontal ($\hat{z}'$) expansion of the beam radiated from the pre-bunching launcher. The squares indicate the measured data points, the circles indicate the values of beam radius predicted by the Stratton-Chu vector diffraction theory, and the solid line shows the theoretical expansion for a Gaussian beam with waist $w_{0z'}$ = 0.9 cm.

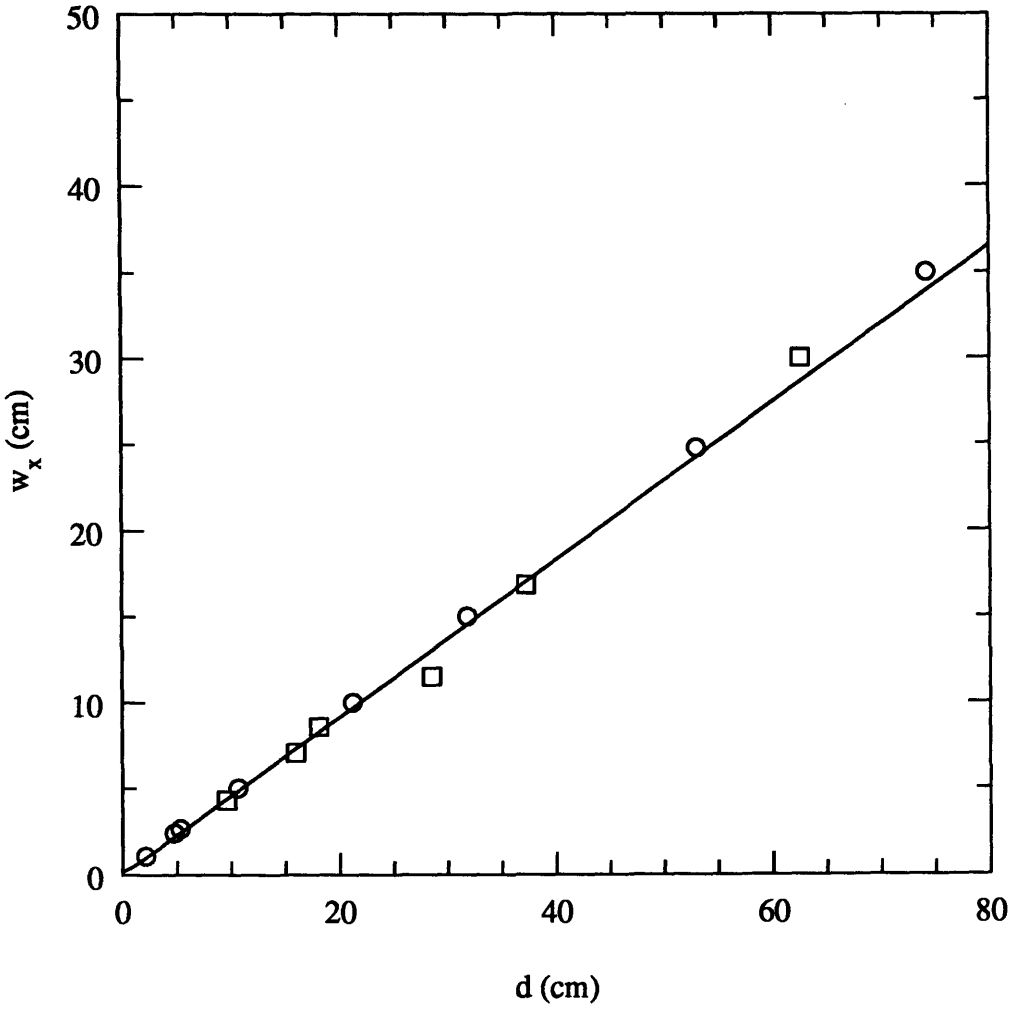

Figure 3.34 Vertical ($\hat{x}$) expansion of the beam radiated from the pre-bunching launcher. The squares indicate the measured data points, the circles indicate the values of beam radius predicted by the Stratton-Chu vector diffraction theory, and the solid line shows the theoretical expansion for a Gaussian beam with waist w_{0x} = 0.19 cm.

It is seen from Figs. 3.30–3.34 that the measurements of the beam radiated from the pre-bunching launcher are in good agreement with predictions of vector diffraction theory, with the exception of the side lobe of power. This side lobe was observed in the tests but was not predicted by the coupled mode theory, which assumed that 100% of the radiation incident on the launcher was in the $TE_{22,6}$ mode.

3.4.1.2 Measurement of Beam from Full Converter

After the measurements of the beam radiated from the pre-bunching launcher were completed, the two mirror relay was mounted on the launcher and measurements of the beam formed by the full converter were made.

Figure 3.14 shows the configuration for the measurements described below. The result of the experimental scan of the $\hat{x}$ component of beam at the output of the full converter is shown in Figure 3.35. The scan was made at d = 32 cm, in a plane perpendicular to the beam propagation direction. Figure 3.35 shows a Gaussian-like main lobe with waists w_x = 1.8 cm and $w_{z'}$ = 2.2 cm, and two additional side lobes of power at peak intensities -12.5 dB and -15.5 dB from the peak of the main lobe, respectively.

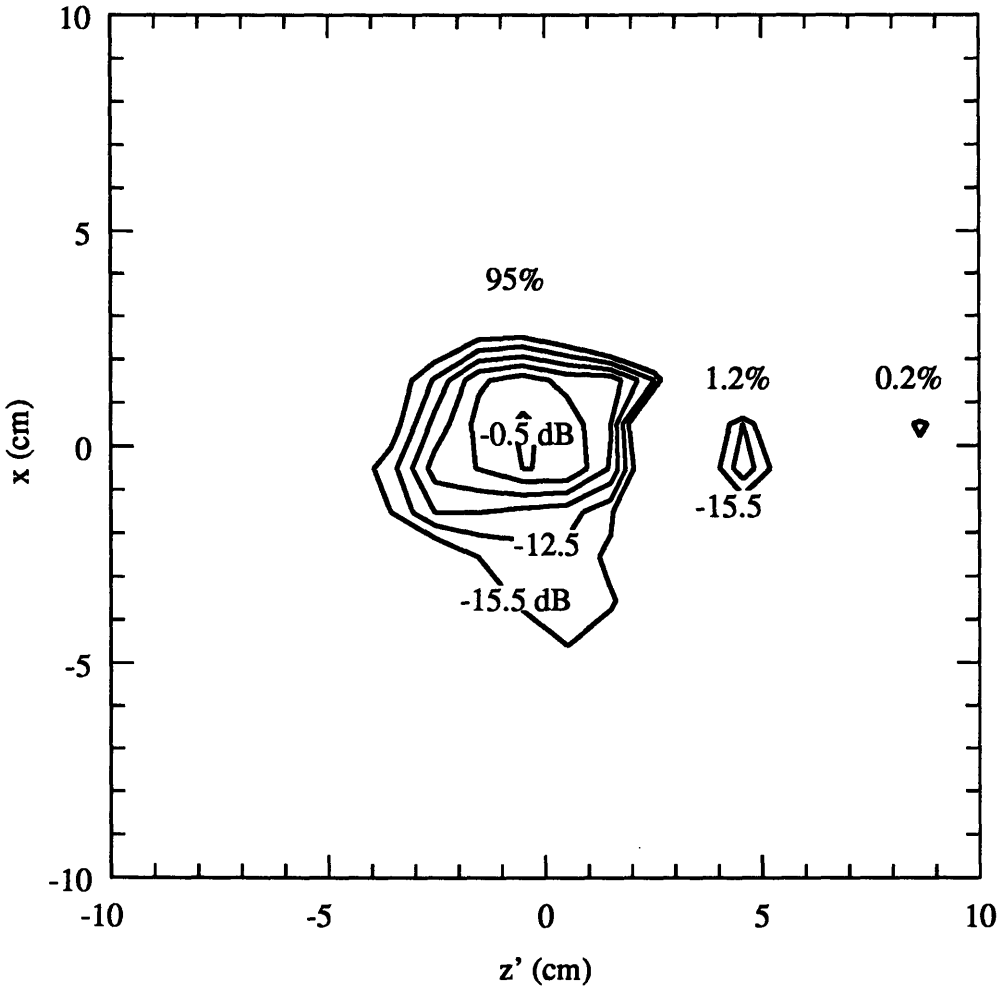

Figure 3.35 Experimental diode scan of the beam leaving the two mirror transmission line. The scan was made in a plane perpendicular to the incoming beam at d = 32 cm. Lines of constant $|E_x|^2$ are shown in dB below peak intensity. The peak of the cross polarization was measured to be <-25 dB from the peak of the E_x intensity.

A piece-wise integration over the experimental data points was performed and it was found that approximately 95% of the power is contained in the main lobe, with 1.2% of the power in the first side lobe and 0.2% in the second side lobe. Approximately 3.6% of the power was scattered over the background, not contained in any of the three lobes. Figures 3.36 and 3.37 show horizontal ($\hat{z}'$) and vertical ($\hat{x}$) cuts through the center of the main lobe. Also shown on the plots are the theoretical patterns for the design output beam. Figures 3.36 and 3.37 indicate good agreement between the design output beam and the measured beam, with the exception of the two small side lobes of power.

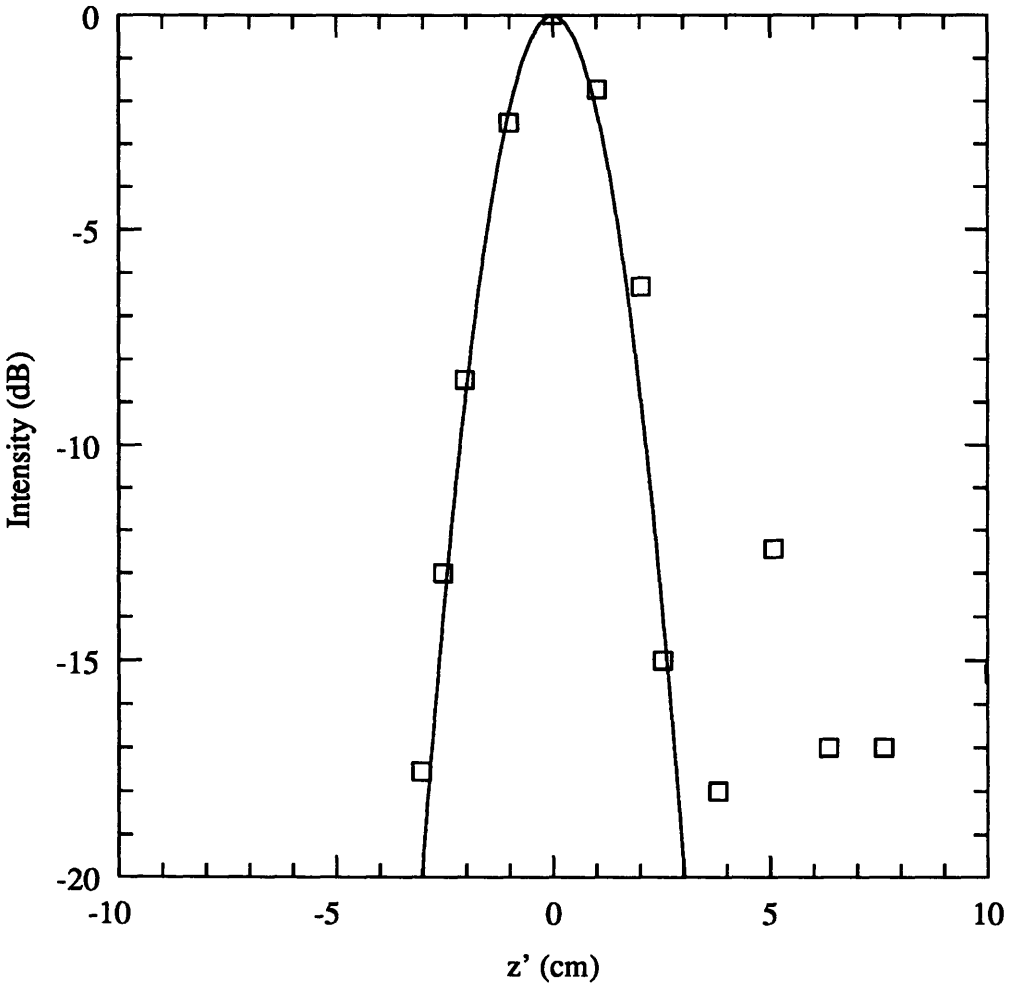

Figure 3.36 Horizontal cut through the center of the beam at the output of the full converter (Fig. 3.35). The squares indicated measured data points and the solid line shows the profile for the desired Gaussian beam, w_0 = 0.9 cm.

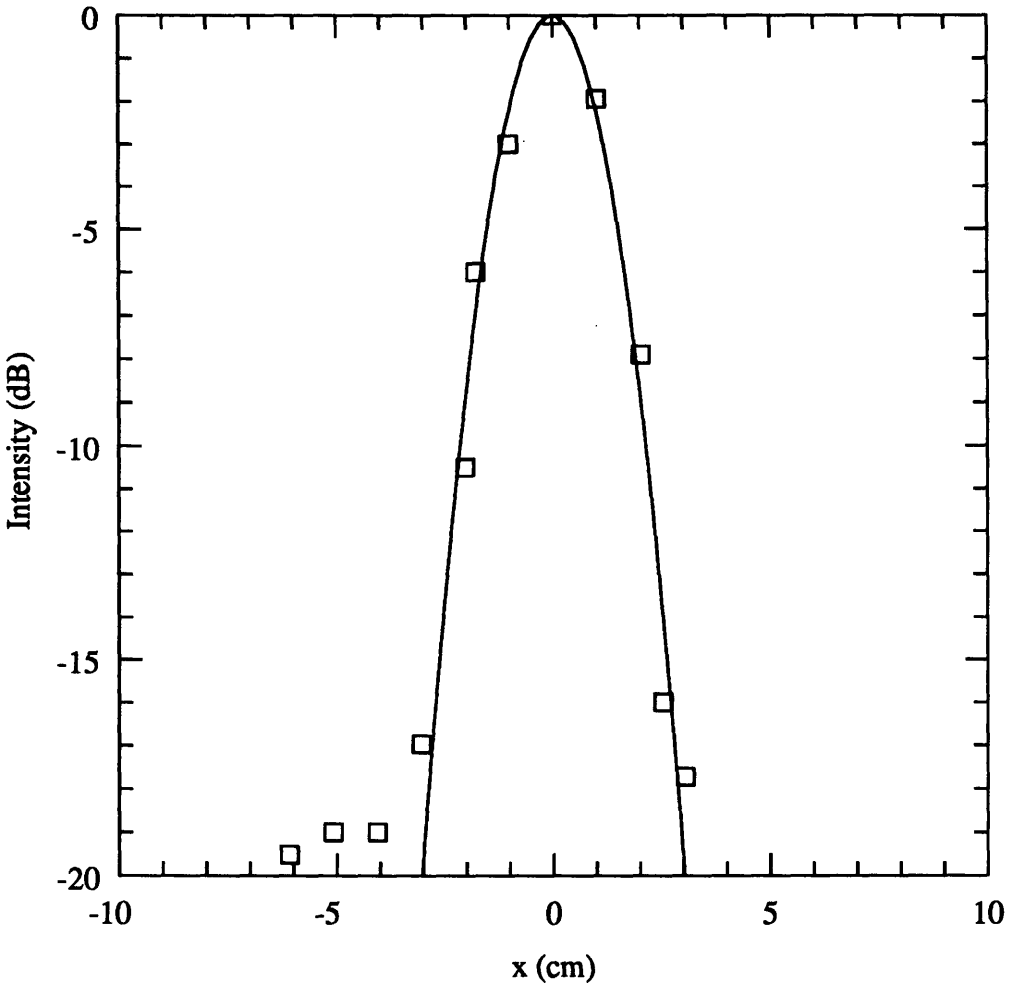

Figure 3.37 Vertical cut through the center of the beam at the output of the full converter (Fig. 3.35). The squares indicated measured data points and the solid line shows the profile for the desired Gaussian beam, w_0 = 0.9 cm.

Scans such as the one shown in Figure 3.35 were made in planes at several values of d. At each d value, the vertical and horizontal beam radii for the main lobe were measured. The results of these beam expansion measurements are shown in Figure 3.38. Measured values of horizontal ($w_{z'}$) and vertical (w_x) beam radii are plotted against d, the propagation distance. Also shown in Figure 3.38 is the theoretical expansion for a fundamental circular Gaussian beam with waist w_0 = 0.9 cm at d = 10.6 cm, which is the design beam. As indicated by the figure, the expansion of the measured beam is in good agreement with the theoretical expansion of the design beam.

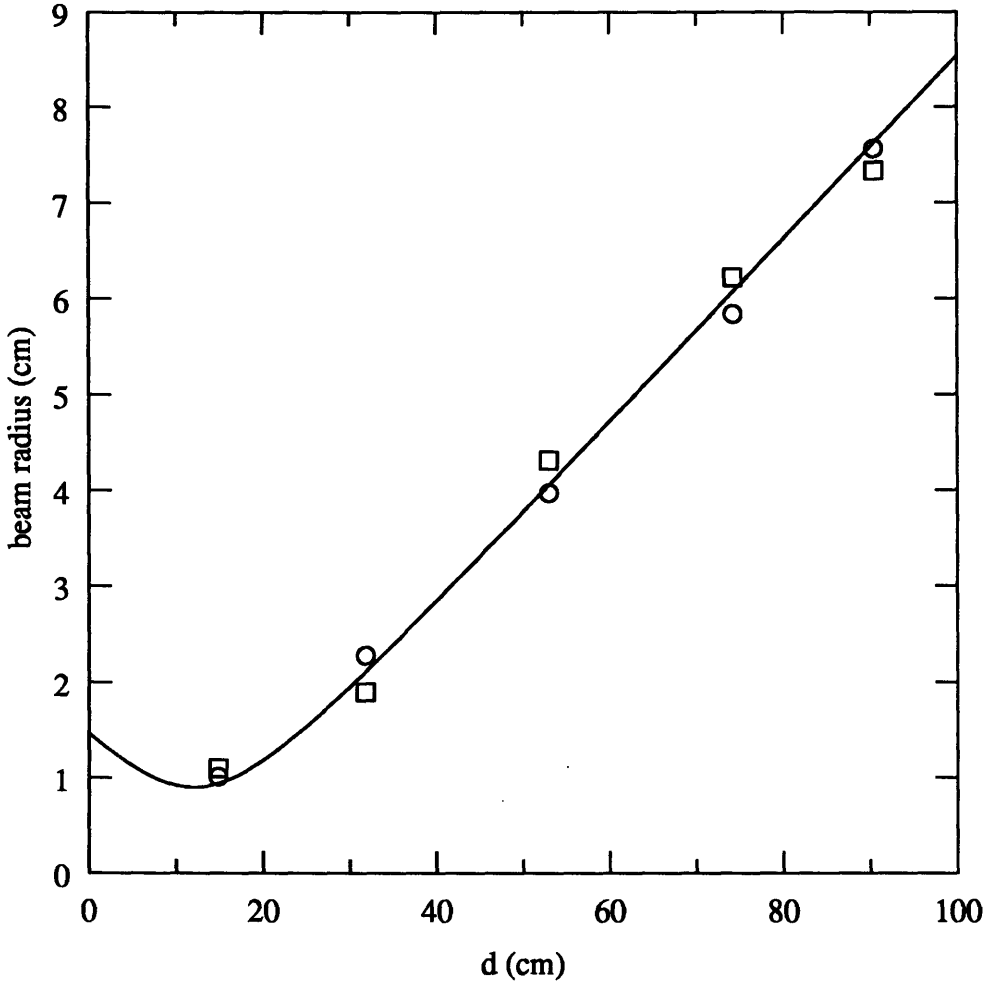

Figure 3.38 Horizontal ($\hat{z'}$) and vertical ($\hat{x}$) expansions of the beam at the output of the pre-bunching converter. The squares indicate the measured values of $w_{z'}$, the circles indicate the measured values of w_x and the solid line shows the theoretical expansion for a Gaussian beam with waist w_0 = 0.9 cm at d = 10.6 cm.

Additional side lobes of power were observed in both the scan of the beam radiated from launcher (Fig. 3.30) and the scan of the beam at the output of the mirror transmission line (Fig. 3.35). It was suspected that these side lobes were due to a mix of modes incident on the pre-bunching launcher, which was designed for an input of 100% $TE_{22,6}$ mode. The discontinuity of the waveguide at the vacuum window was believed to generate this unfavorable mode mix, similar to mode conversion previously observed in the Vlasov-type converter experiments. In order to determine the mix of modes incident on the pre-bunching launcher, a Vlasov-type launcher and reflector were designed for the $TE_{22,6}$ mode at 110 GHz. Any mode conversion from the $TE_{22,6}$ mode at the vacuum window gives rise to neighboring radial and azimuthal modes also at 110 GHz. These additional mode have different characteristic polar bounce angles, θ_B, and appear as distinct focal spots in the far field. This phenomenon was previously noted in Chapter 2.

In the experiments described below, the $TE_{22,6}$ Vlasov-type converter was used only as a diagnostic for determining mode content. The reflector, designed with the geometric optics formula given by Eq. 2.20, subtends only $3\alpha = 180^o$. As discussed in Chapter 2, a mirror must subtend a minimum of 4α degrees in order to intercept >95% of the power radiated from the simple Vlasov launcher. Therefore, significant power was lost around the edges of the doubly curved reflector. Also, any power intercepted by the reflector that falls outside the pattern predicted by geometric optics is directed toward the focus, but will most likely arrive with phase aberrations, creating a beam with a Gaussian amplitude profile at the waist, but non-Gaussian beam expansion characteristics. For these reasons, the Vlasov-type converter is not ideal for converting the $TE_{22,6}$ mode to a Gaussian beam. The Vlasov-type converter does, however, provide a good indication of the mode mix at the sleeve output.

The $TE_{22,6}$ Vlasov-type launcher was mounted on the sleeve, in place of the pre-bunching launcher, and the doubly curved reflector was mounted at its design position relative to the launcher straight cut. The test apparatus for measuring the pattern from the Vlasov-type converter is shown in Fig. 2.10. An experimental scan was made in the focal plane and the results are shown in Fig. 3.39. Lines of constant $|E_x|^2$ are plotted in dB below peak intensity. Figure 3.39 shows a main lobe in the theoretical position for the $TE_{22,6}$ focus and two side lobes of power in the theoretical positions for the focii of the $TE_{23,6}$ mode and the $TE_{21,6}$ mode. A piece-wise power integration over the experimental scan indicates that 93% of the power is contained in the $TE_{22,6}$ focus, 6% in the $TE_{23,6}$ focus, and 1% in the $TE_{21,6}$ focus.

The coupled mode theory and Stratton-Chu diffraction theory were then used to analyze the pattern produced at the output of the mirror transmission line resulting from a mix of

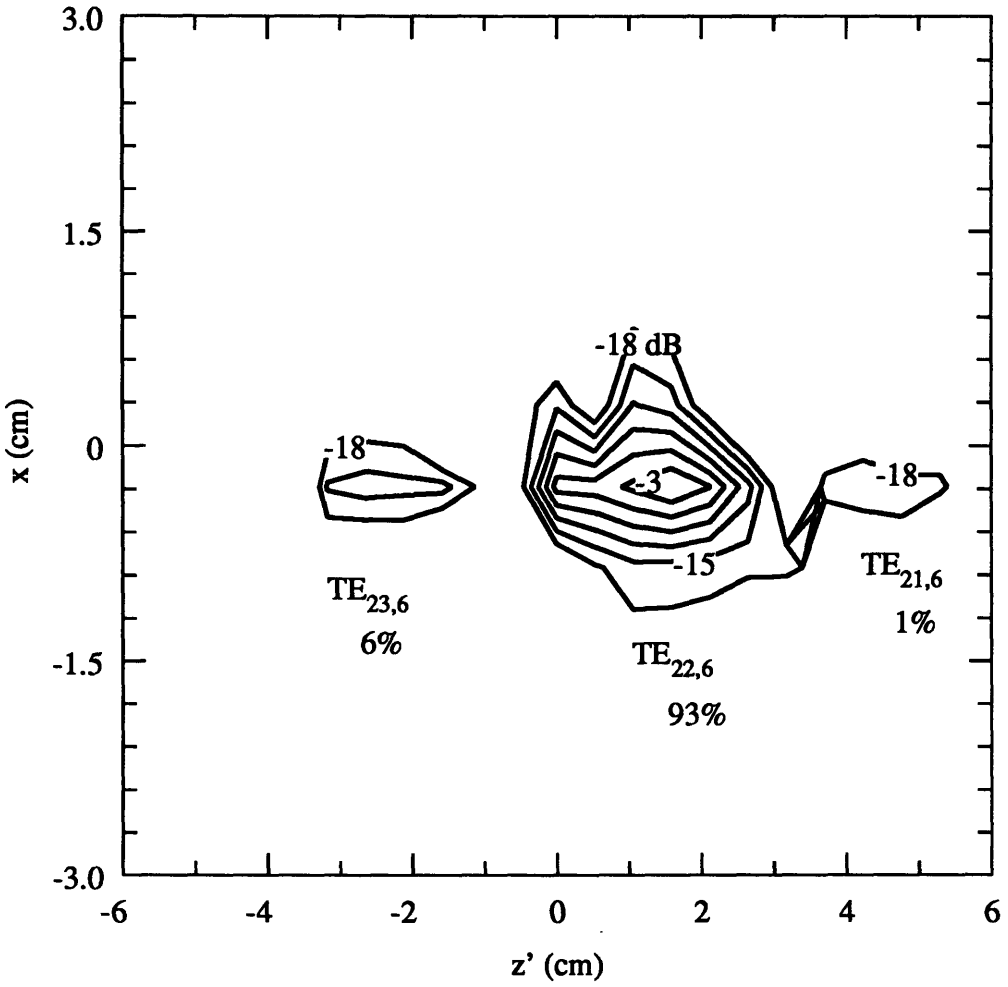

Figure 3.39 Diode scan in the focal plane of the $TE_{22,6}$ Vlasov-type converter. Lines of constant $|E_x|^2$ are plotted in dB below peak intensity. Piece-wise integration over the scan indicates a mode mix of 93% $TE_{22,6}$, 1% $TE_{21,6}$ and 6% $TE_{23,6}$, all at 110 GHz.

modes incident on the pre-bunching launcher. Figure 3.40 shows the theoretical pattern at the output of the two mirror relay at d = 32 cm produced by the input mode mix deduced from the Vlasov converter test; 93% $TE_{22,6}$, 6% $TE_{23,6}$, and 1% $TE_{21,6}$. A comparison of Fig. 3.40 and the experimental scan, Fig. 3.35, shows excellent agreement between theory and measurement. This agreement between theory and experiment indicates that the side lobes of power were due to a mix of modes at the input of the pre-bunching launcher. It was expected that for the internal converter experiments, where no gap in the waveguide present and chances of mode conversion are diminished, the side lobes would not occur.

Finally, power measurements were made with the 10 cm Scientech laser calorimeter. In order to obtain the conversion efficiency, the mode converter was removed and the power at

the output of the sleeve was measured. The converter was reinstalled and the power in the output beam was measured, with the calorimeter in the observation plane that is indicated in Fig. 3.14. It was found the >98% of the power leaving the sleeve was incident on the 10 cm diameter calorimeter. The diode scans made at the output of the two mirror transmission line suggest that 95% of that power, or 93% of the total power leaving the gyrotron, is in the $TE_{22,6}$ main beam.

The corrugated waveguide experiments, described below, provided an additional measure of conversion efficiency.

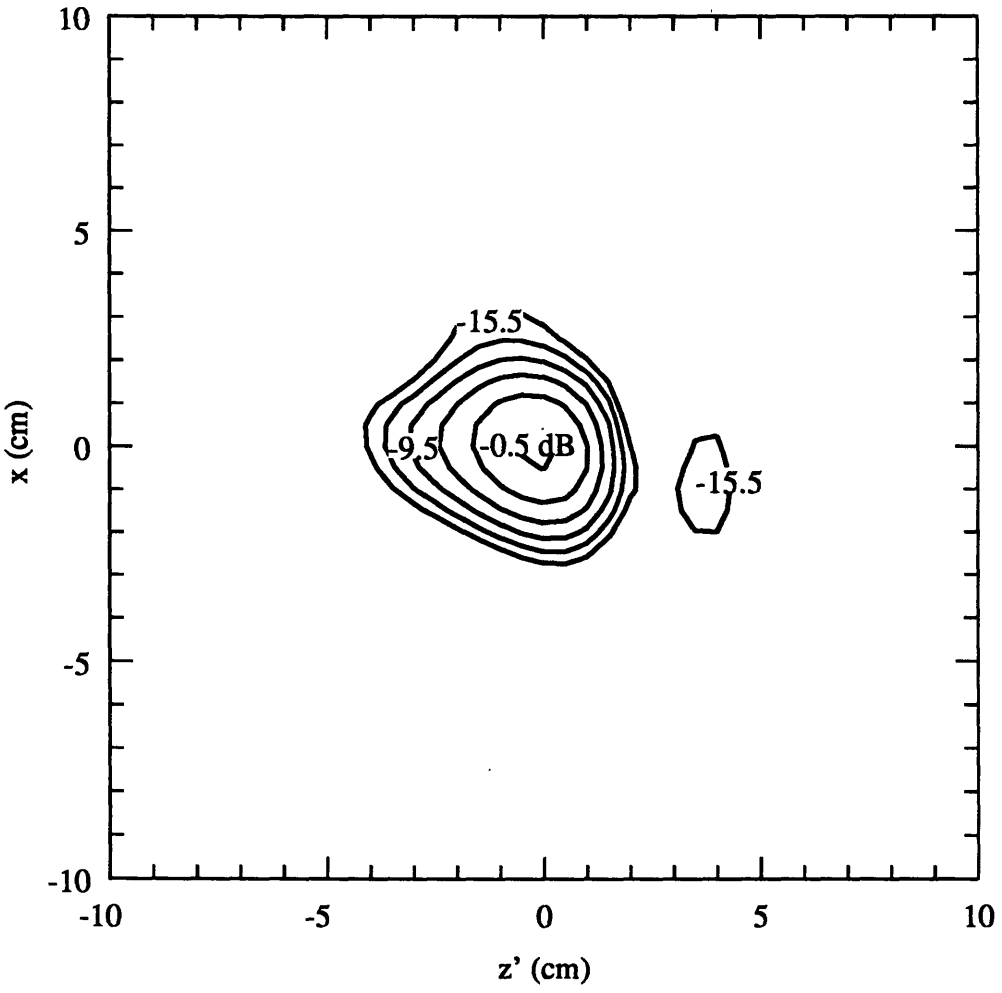

Figure 3.40 Diffraction theory prediction of the beam radiated from the pre-bunching converter based on a mode mix of 93% $TE_{22,6}$, 1% $TE_{21,6}$, and 6% $TE_{23,6}$, all at 110 GHz, incident on the pre-bunching launcher. The observation plane is at d = 32 cm and lines of constant $|E_x|^2$ are plotted in dB below peak intensity.

3.4.1.3 Corrugated Waveguide Experiments

As the next experiment in the external test configuration, the beam from the full converter was directed into a 1.25 in. diameter corrugated waveguide run. The run consists of two straight waveguide sections joined by a 90° miter bend. It was previously mentioned that the most efficient coupling of a Gaussian beam to the HE_{11} mode of a corrugated guide is made when the beam waist is $0.596R_w$, or 0.95 cm in this case, and when the entrance to the guide is at the position of the waist. The beam formed by the pre-bunching converter, with waists $w_{0x} = w_{0z'} = 0.9$ cm should, therefore, couple into the specified corrugated waveguide with high efficiency.

Figure 3.41 shows the configuration for the corrugated guide coupling experiments. The entrance to the guide was placed at $y = 10$ cm, the calculated and measured position of the beam waist. The input guide was aligned with the propagation direction of the incoming beam. Diode scans and calorimetric efficiency measurements were made at the output of the corrugated guide run, in planes perpendicular to the beam propagation direction, distances d from the guide output.

Figure 3.42 shows the results of an experimental scan made at $d = 5$ cm. Lines of constant $|E_x|^2$ are plotted in dB below peak intensity. The peak of the cross polarization, $|E_{z'}|^2$, was measured to be <-25 dB from the peak of the E_x intensity. As shown in Figure 3.42, the pattern at the guide exit has a Gaussian-like profile, indicating that the power in the corrugated waveguide is in the HE_{11} mode. Scans such as that shown in Fig. 3.42 were made in planes at several d values and the beam radii in the horizontal and vertical directions were measured as a function of distance from the guide exit. Figure 3.43 shows the measured values of horizontal and vertical beam radius, indicated by the squares and circles, respectively. In Fig. 3.43, the solid line shows the theoretical expansion for an HE_{11} mode radiated from a 1.25 in. diameter waveguide. It is evident from Figs. 3.42 and 3.43 that the power in the corrugated waveguide is contained primarily in the HE_{11} mode.

Next, the diode detector was removed and the 10 cm calorimeter was placed at the exit of the guide. The power was measured and compared to the power coming directly from the gyrotron sleeve. It was observed that 92% of the total power leaving the sleeve was incident on the calorimeter at the guide exit. This measurement allows for the calculation of overall efficiency given by:

$$\eta_{total} = \frac{\text{power at guide exit}}{\text{TE}_{22,6}\text{ power at sleeve}} = \frac{0.92}{0.93} = 0.98 \qquad (3.35)$$

Thus, the external testing of the pre-bunching converter shows that the experimental results are in good agreement with predictions of vector diffraction theory and that the

pre-bunching converter transforms the $TE_{22,6}$ mode at 110 GHz to a Gaussian-like beam in free space with ~98% efficiency.

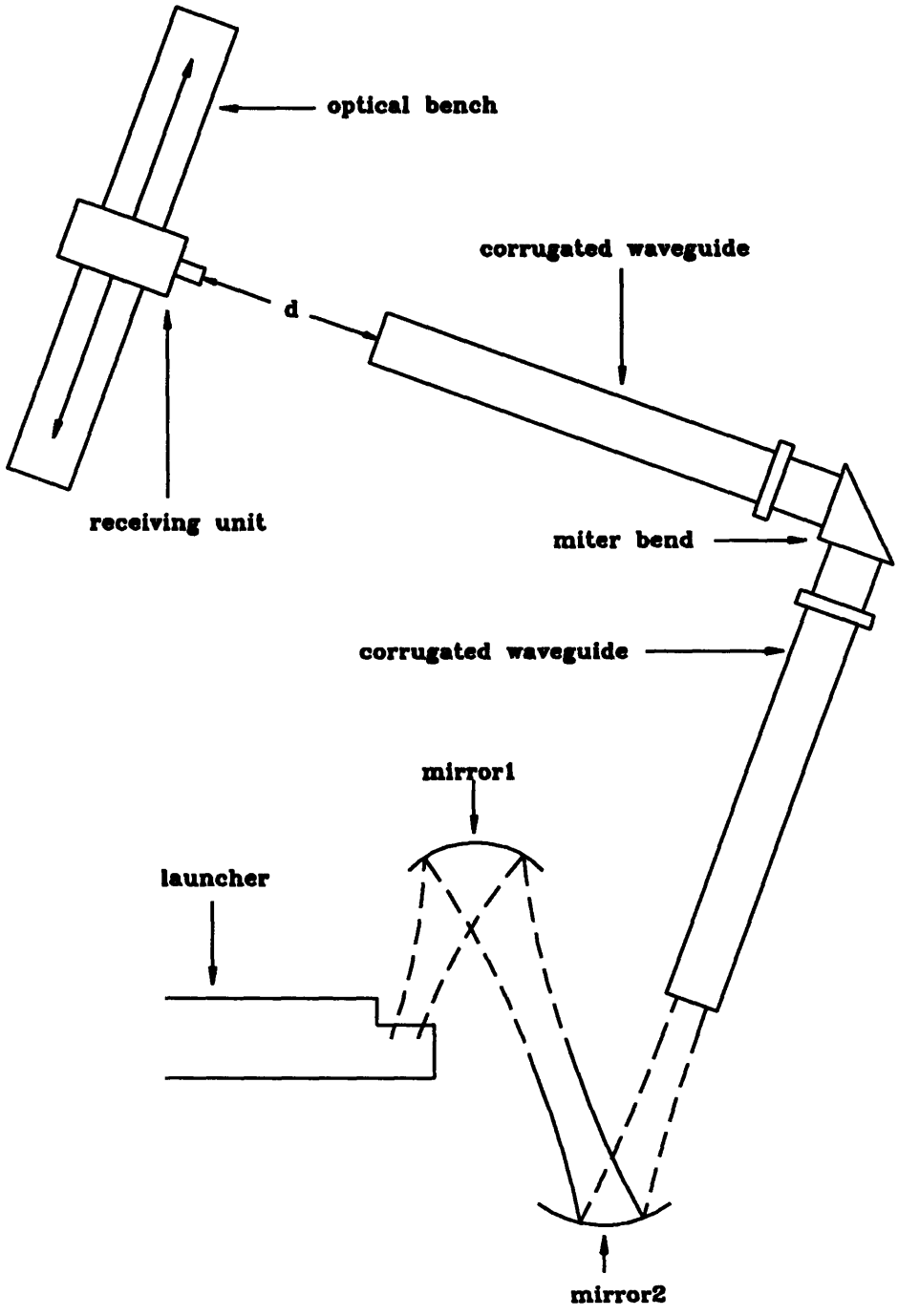

Figure 3.41 Schematic of the corrugated waveguide test apparatus. The receiving unit is placed on an optical bench, which is mounted perpendicular to the waveguide.

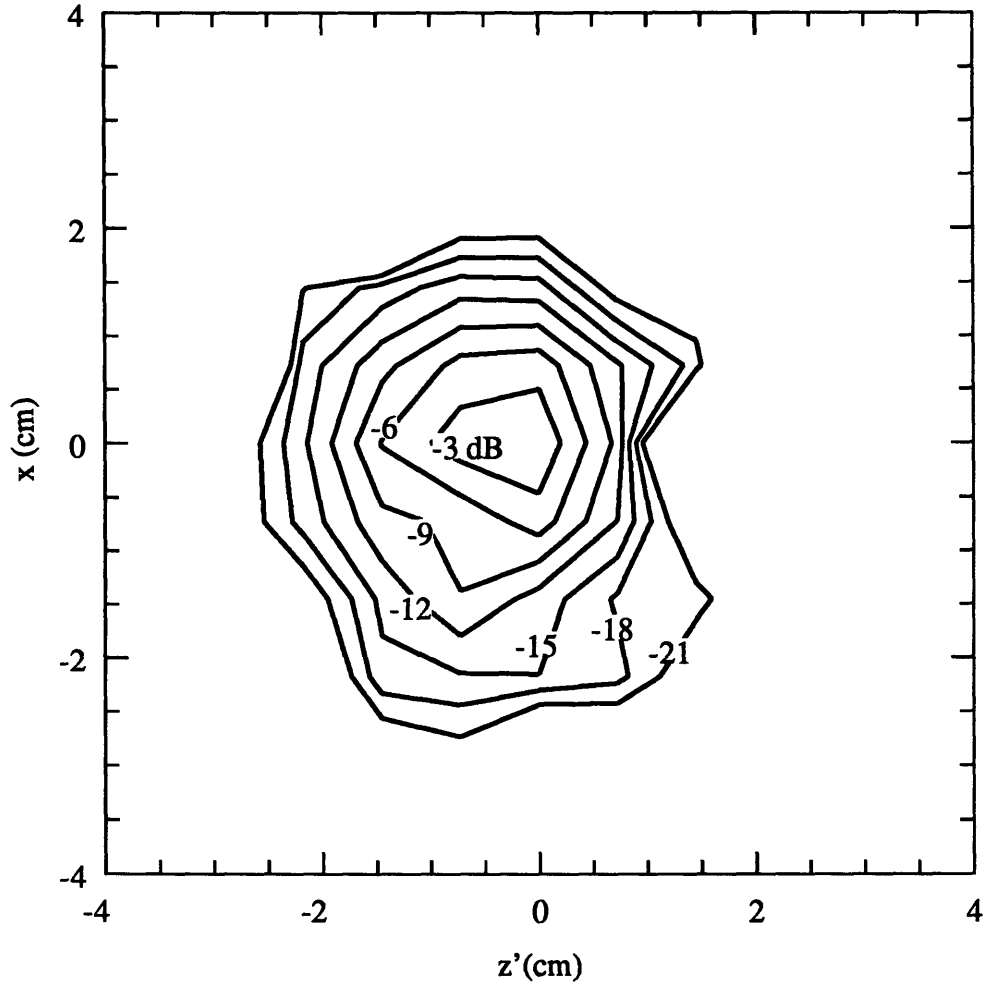

Figure 3.42 Diode scan of the beam exiting the corrugated waveguide at d = 5 cm. Lines of constant $|E_x|^2$ are plotted in dB below peak power. The peak intensity in the cross polarization, $E_{z'}$ was measured to be <-25 dB from the peak of the E_x intensity.

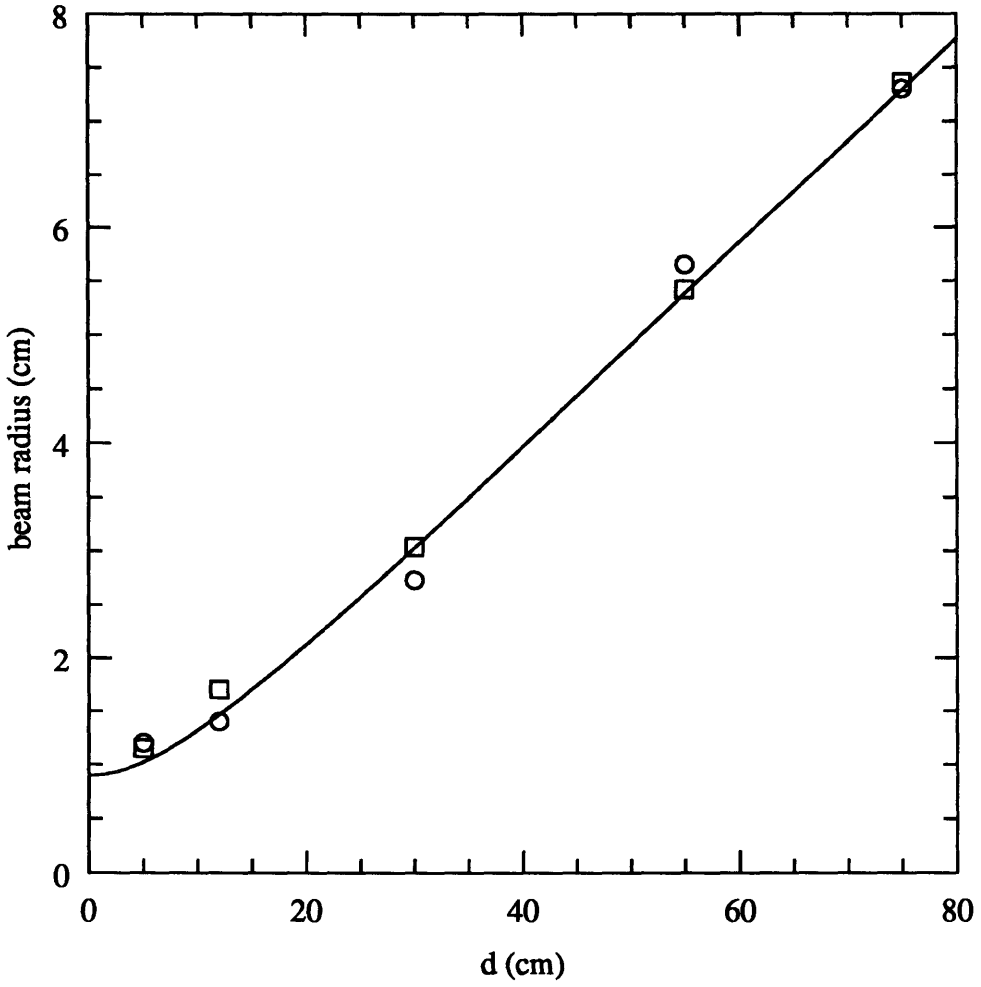

Figure 3.43 Horizontal ($\hat{z'}$) and vertical ($\hat{x}$) expansions of the beam output from the corrugated waveguide. The squares indicate the measured values of $w_{z'}$, the circles indicate the measured values of w_x and the solid line shows the theoretical expansion for the HE_{11} mode from a guide with diameter 1.25 in.

3.4.1.4 Beam Splitting Mirror Relay Experiments

With the operation of the launcher and two mirror transmission line fully characterized, as described above, the four additional reflectors of the beam splitting mirror relay were tested. A schematic of the experimental configuration is shown in Fig. 3.28.

Radiation pattern scans at the output of the beam splitting mirror relay were made in planes perpendicular beam propagation direction, at constant values of y. Figure 3.44 shows the result of a diode scan at y = 53 cm. Lines of constant $|E_x|^2$ are plotted in dB below peak power. The peak intensity of the cross polarization, E_z, was measured to be <-25 dB from the peak of the E_x intensity. The experimental result in Fig. 3.44 can be compared to Fig. 3.25, the diffraction theory prediction of the dual beam pattern at y = 53 cm. The predicted and measured patterns are in excellent agreement. Both show two Gaussian-like beams of approximately equal power.

Figs. 3.45 and 3.46 show the experimental and theoretical dual beam patterns at y = 72 cm. Again, the measured pattern is in good agreement with the prediction of vector diffraction theory.

Scans such as those shown in Figs. 3.44 and 3.45 were made in planes at several values of y and the expansions of the two beams were measured. Figures 3.47 and 3.48 show the measured and theoretical expansions for the upper beam (beam a) and lower beam (beam b), respectively. Also plotted on Figs. 3.47 and 3.48 is the theoretical expansion for the design beam, a fundamental Gaussian with waist w_0 = 1.5 cm at y = 20 cm. Figures 3.47 and 3.48 show that both beams are expanding in much the same manner as the design beam. The measured beam expansions are in good agreement with diffraction theory predictions, which are also plotted on Figs. 3.47 and 3.48.

Calorimetric power measurements showed that 94±% of the power leaving the sleeve was converted into the dual beam output. The upper beam contained 52% of the power from the sleeve and 42% of the power was found in the lower beam. This is in good agreement with the diffraction theory, which suggested that 52% of the power would be found in beam a and 48% of the power would be contained in beam b.

Thus, diode scans and calorimetric efficiency measurements show that the beam splitting mirror relay effectively divides the incident Gaussian beam, formed by mirrors 1 and 2, into two similar Gaussian beams of roughly equal power. The measured beam patterns are in good agreement with diffraction theory calculations.

With the external testing of the pre-bunching converter and beam splitting mirror relay completed, the launcher and two mirror relay were put inside the gyrotron tube, as shown in Fig. 3.29, and further experiments were performed.

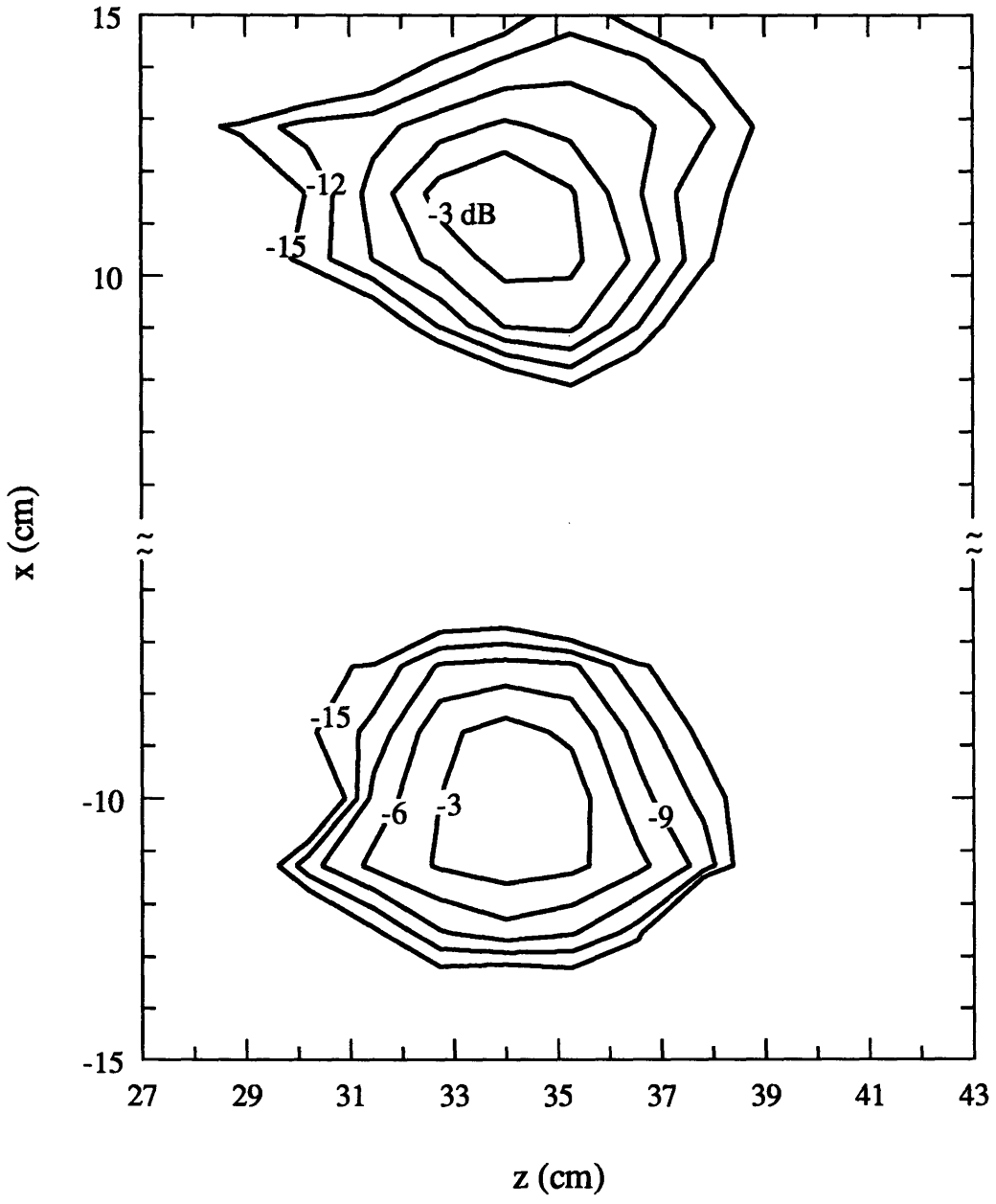

Figure 3.44 Diode scan at y = 53 cm of the dual beam output from the beam splitting mirror relay. Lines of constant $|E_x|^2$ are plotted in dB below peak intensity.

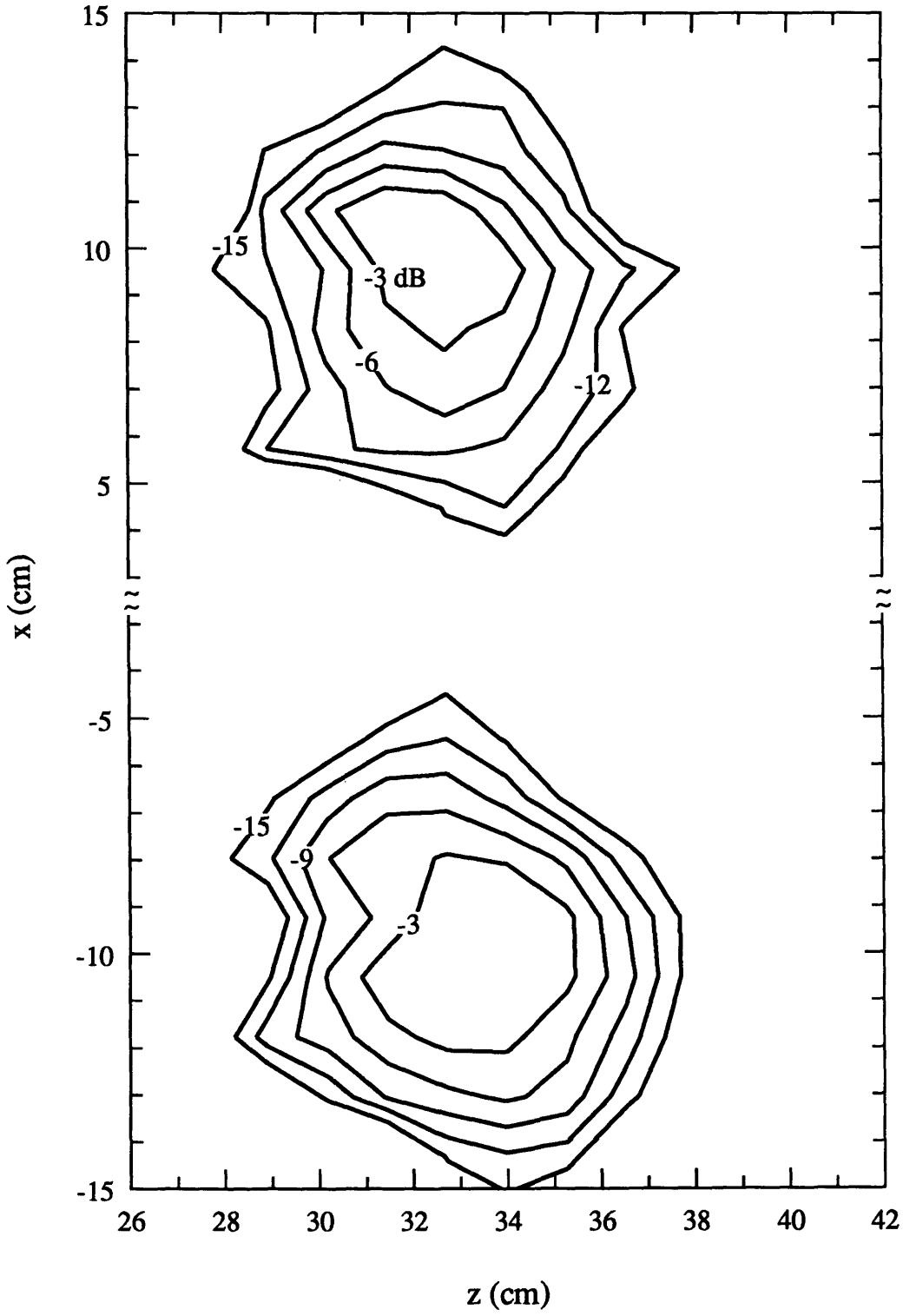

Figure 3.45 Diode scan at y = 72 cm of the dual beam output from the beam splitting mirror relay. Lines of constant $|E_x|^2$ are plotted in dB below peak intensity.

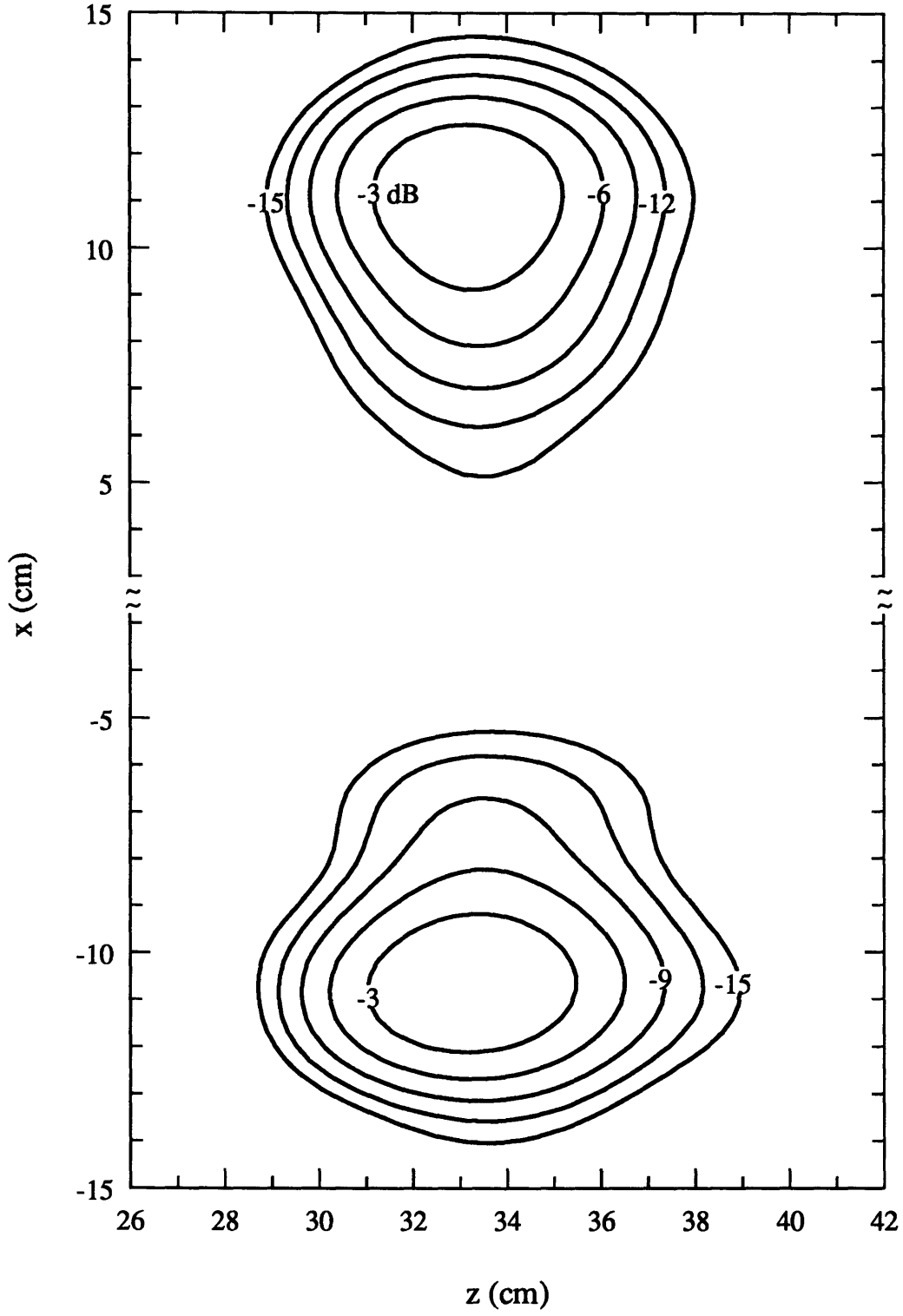

Figure 3.46 Diffraction theory prediction of the dual beam output from mirrors 5 and 6, calculated in the launcher coordinate system at y = 72 cm. Lines of constant $|E_x|^2$ are shown in dB below peak intensity.

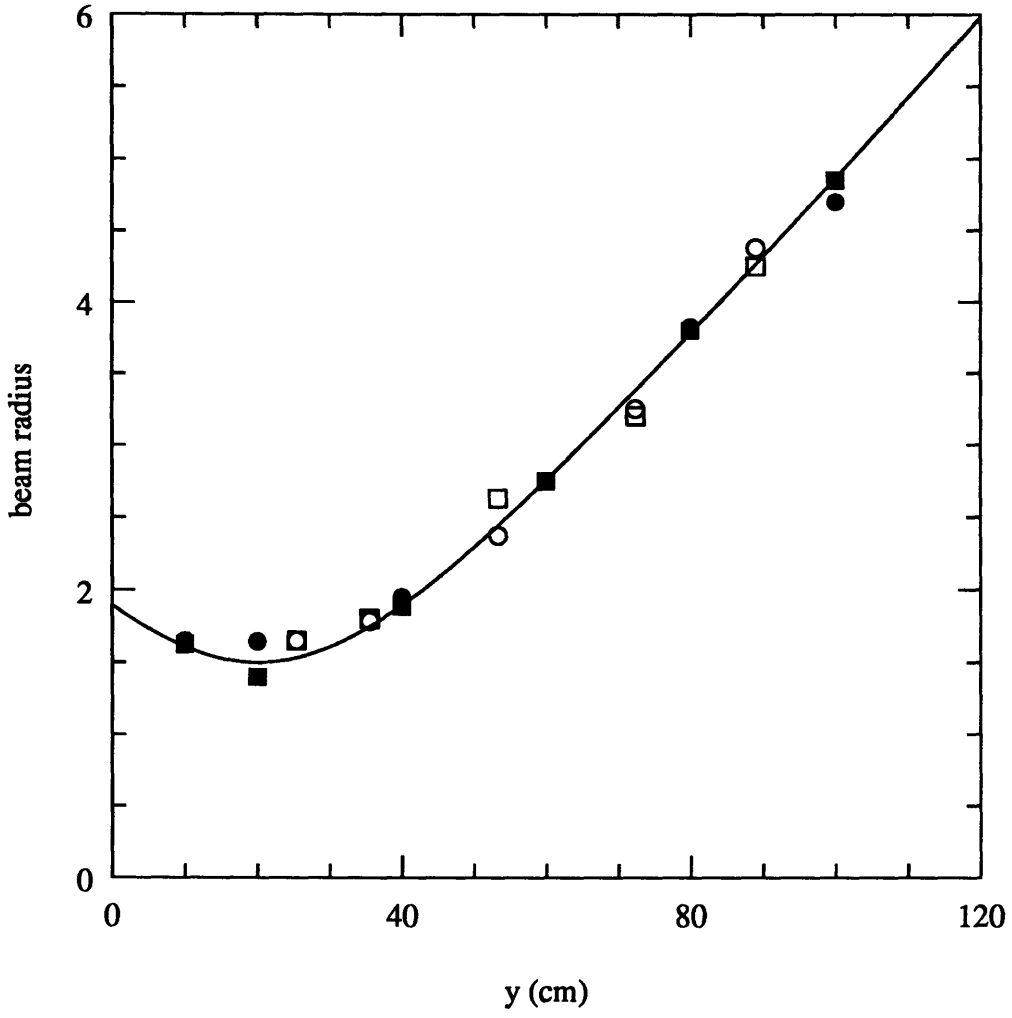

Figure 3.47 Horizontal ($\hat{z}$) and vertical ($\hat{x}$) expansions of the upper beam (beam a) formed by the beam splitting mirror relay. The open squares indicate the measured values of w_z and the open circles indicate the measured values of w_x. The filled squares indicate the diffraction theory predictions of w_z and the filled circles show the diffraction theory predictions of w_x. The solid line shows the theoretical expansion for a Gaussian beam with waist $w_0 = 1.5$ cm at $y = 20$ cm.

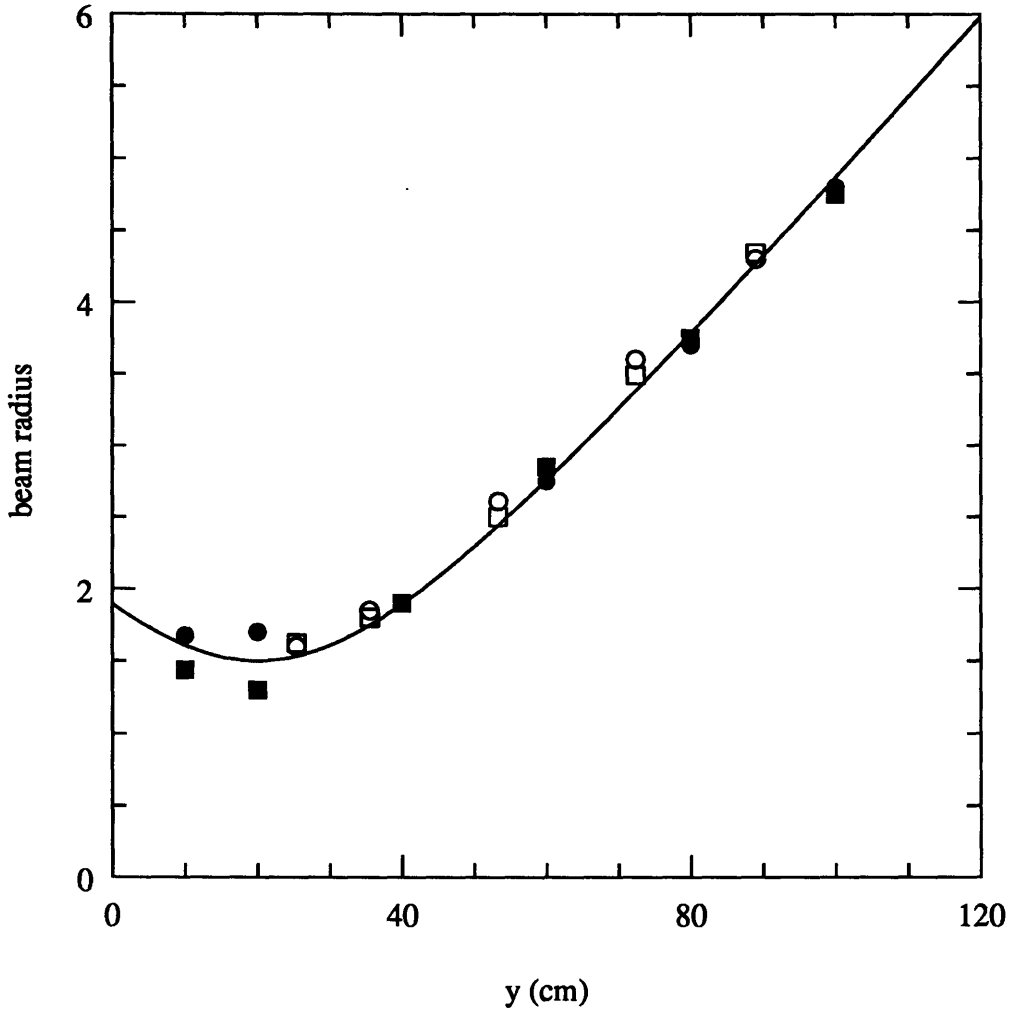

Figure 3.48 Horizontal ($\hat{z}$) and vertical ($\hat{x}$) expansions of the lower beam (beam b) formed by the beam splitting mirror relay. The open squares indicate the measured values of w_z and the open circles indicate the measured values of w_x. The filled squares indicate the diffraction theory predictions of w_z and the filled circles show the diffraction theory predictions of w_x. The solid line shows the theoretical expansion for a Gaussian beam with waist $w_0 = 1.5$ cm at $y = 20$ cm.

3.4.2 Internal Converter Experiments

The pre-bunching mode converter, consisting of the launcher and two mirror transmission line, was installed in the gyrotron vacuum tube, as shown in Fig. 3.29. The beam formed by the converter exited the vacuum tube through a quartz window 4 inches in diameter, which is at the location y = 19 cm in the launcher coordinate system. Near field radiation pattern measurements of the beam formed by the converter were made outside the vacuum tube. The beam and launcher coordinate systems used in the internal testing are identical to those defined for the external tests.

The results of a scan made at d = 38 cm are shown in Fig. 3.49. Lines of constant $|E_x|^2$ are plotted in dB below peak intensity. The peak intensity in the cross polarization, $E_{z'}$ was <-25 dB from the peak of the E_x intensity. Figure 3.49 shows a small, Gaussian-like focus. The additional side lobes that were observed in the external converter experiments are not present in the scan of the beam formed by the internal converter. This fact is consistent with the hypothesis that the spurious lobes were caused by an improper mode mix incident on the launcher. The mode mix was believed to be due to the mode conversion caused by the disruption between the internal and external waveguides at the vacuum window. With the converter inside the vacuum tube, no such disruption occurs, and the mode incident on the converter is believed to be purely $TE_{22,6}$. Consequently, the small level side lobes were not expected to be present in the internal converter experiments, and, in fact, they were not observed.

Scans such as that shown in Fig. 3.49 were made at several values of d. Figure 3.50 shows the measured horizontal and vertical beam radii plotted as a function of propagation distance, d. Also shown in Fig. 3.50 is the theoretical expansion for a circular fundamental Gaussian beam with waists $w_{0x} = w_{0z'}$ = 0.9cm at d = 10.6 cm. Figure 3.50 shows that the measured beam formed by the internal converter expands in very much the same manner as the desired Gaussian beam. A comparison between the expansion of the beam from the internal converter (Fig. 3.50) and the expansion of the main lobe formed by the external converter (Fig. 3.38) shows that the two beams expand in an identical fashion.

Thus, the internal converter experiments confirmed the results obtained from the external testing. In addition, the internal experiments showed no indication of the side lobe power observed in the external experiments, indicating the those spurious side lobes were the result of mode conversion before the pre-bunching launcher due to the vacuum window, and not the result of a design or machining error in the pre-bunching converter.

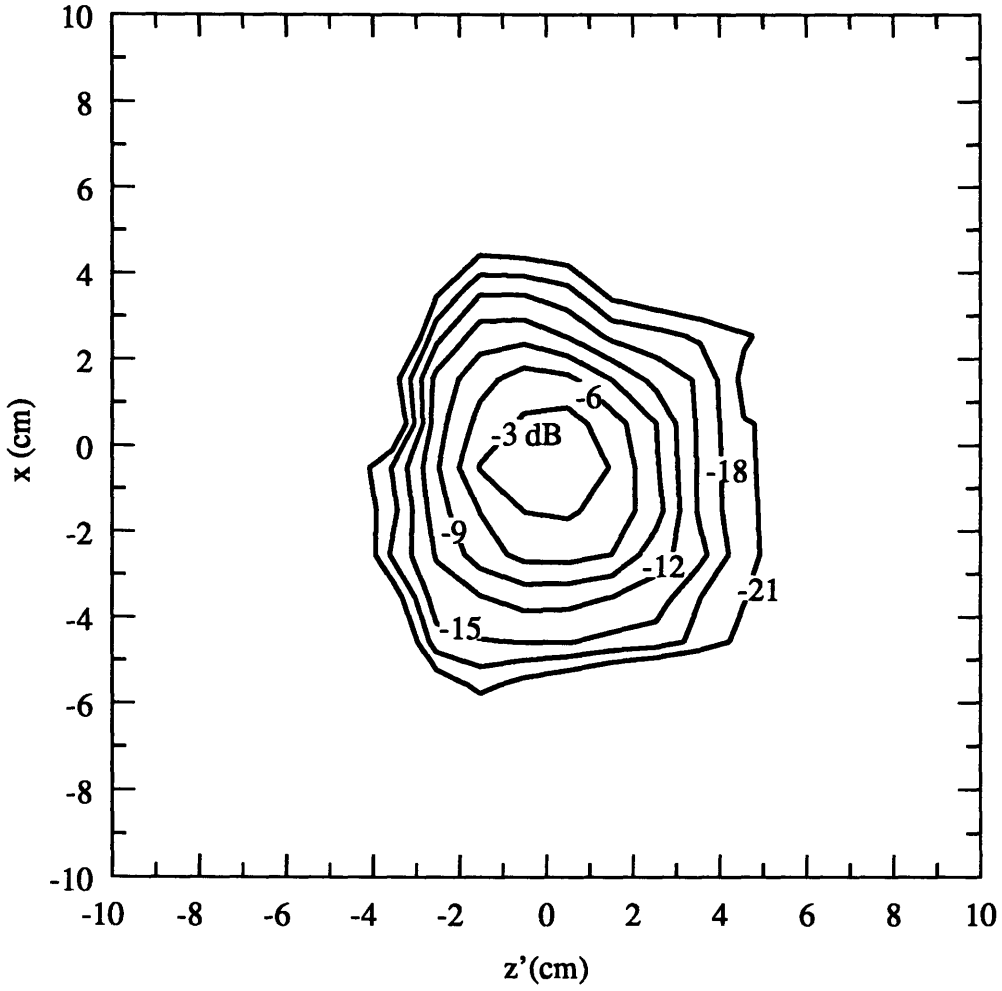

Figure 3.49 Diode scan of the beam from the internal converter at d = 38 cm. Lines of constant $|E_x|^2$ are plotted in dB below peak intensity. The peak intensity in the cross polarization, $E_{z'}$ was measured to be <-25 dB from the peak of the E_x intensity.

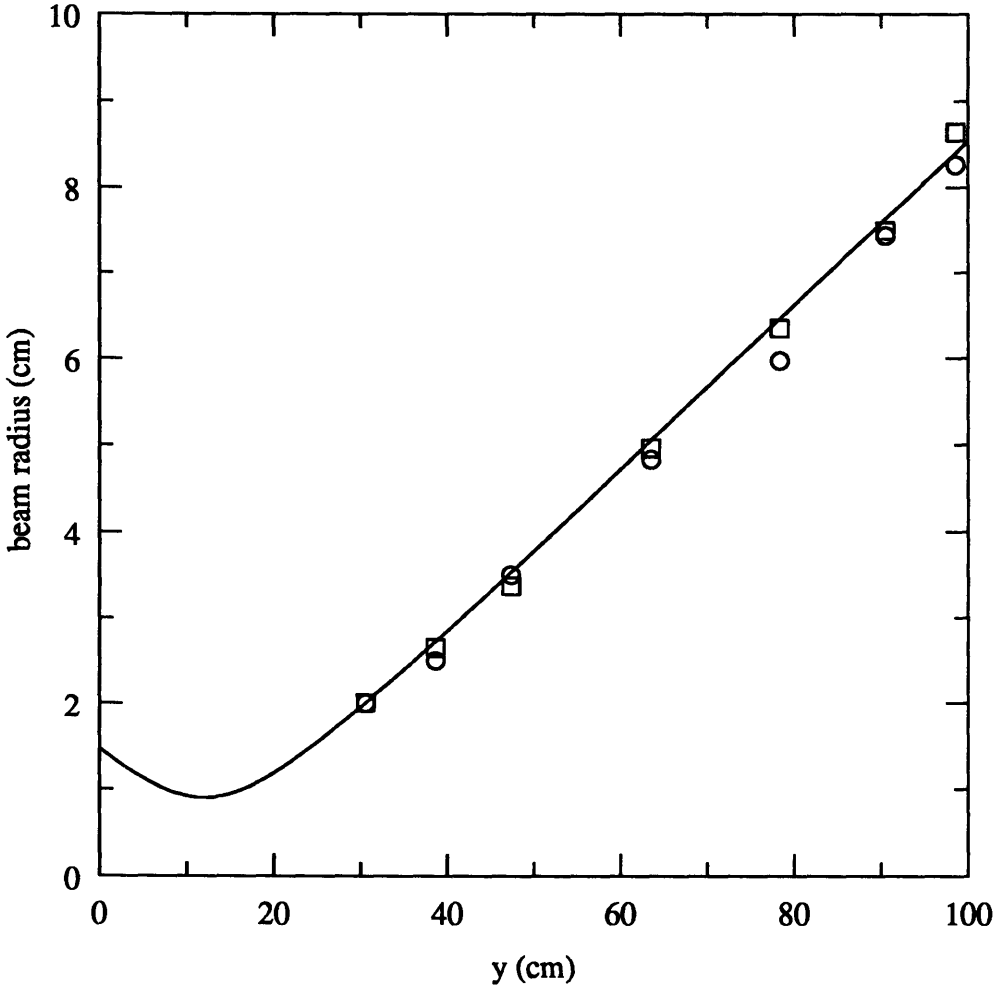

Figure 3.50 Horizontal ($\hat{z}'$) and vertical ($\hat{x}$) expansions of the beam output from the internal converter. The squares indicate the measured values of $w_{z'}$, the circles indicate the measured values of w_x and the solid line shows the theoretical expansion for a Gaussian beam with waist $w_0 = 0.9$ cm at $d = 10.6$ cm.

3.5 Discussion of Results

The experiments described in Section 3.4 fully characterized the operation of the $TE_{22,6}$ pre-bunching converter and beam splitting mirror relay. The experiments were performed in two configurations. First, the mode converter was mounted on the window flange, external to the gyrotron vacuum tube. This configuration had the advantage of allowing the removal of the mirror transmission line to measure the beam as it was radiated from the launcher. Also, with the converter external to the tube, the output beam could be directed into a corrugated waveguide. The external configuration also allowed for direct calorimetric efficiency measurements. The mode converter was removed and the total power from the gyrotron was measured. The mode converter was then reinstalled and the power in the output beam was measured. The efficiency was found by normalizing the Gaussian beam power to the total power from the tube. The external test configuration had the disadvantage of the vacuum window causing a discontinuity and between the waveguide internal to the vacuum and the external waveguide, which provided a potential source of mode conversion.

The near field launcher pattern measurements were in good agreement with predictions of vector diffraction theory. Both theory and experiment showed that the pre-bunching launcher radiates an elliptic beam that expands in the same manner as a Gaussian beam with waists $w_{0z'}$ = 0.9 cm and w_{0x} = 0.19 cm. The experimental scans showed that in addition to this beam, there was a low level side lobe at -11 dB. This side lobe was not predicted by theory for 100% $TE_{22,6}$ mode at 110 GHz incident on the launcher.

The measurements of the beam from the full converter (launcher and two mirror transmission line) also showed a Gaussian-like beam with additional side lobes at the -12.5 dB and -15.5 dB levels. An integration over the experimental scan showed that 95% of the power was contained in the main beam, with 1.2% in the larger side lobe and 0.2% in the smaller side lobe. The integration suggested that 3.6% of the power was spread over the 400 cm^2 area of the scan. Diode measurements at many positions along the propagation length showed that the main beam, containing ~95% of the power, had a fundamental circular Gaussian profile and expanded like a Gaussian beam with waist w_0 = 0.9 cm. The measured beam was in good agreement beam predicted by theory.

A $TE_{22,6}$ Vlasov-type converter was used to measure the mode mix at the sleeve output. A diode scan in the focal plane suggested that 93% of the power leaving the sleeve was contained in the $TE_{22,6}$ mode, with 1% in the $TE_{21,6}$ mode and the remaining 6% in the $TE_{23,6}$ mode. Just as in the Vlasov-type converter experiments (Chapter 2), the discontinuity in the waveguide caused by the vacuum window gave rise to this mode conversion.

The mode mix determined by the Vlasov converter experiments was used as the input to the launcher for the coupled mode and vector diffraction theory simulation of the converter.

With this incident mix, the theory predicted a sidelobe of power at the level of -12.5 dB in the approximate position of the measured side lobe, confirming that the sidelobes arose from an improper mode mix incident on the pre-bunching launcher.

Calorimetric efficiency measurements showed that 98% of the power leaving the gyrotron window was incident on a 10 cm calorimeter centered on the main beam. This suggests 95% of 98%, or 93%, of the power leaving the gyrotron was contained in the main beam.

The entrance to a 1.25 in. diameter corrugated waveguide was placed at the position of the waist of the main beam. As previously discussed, a fundamental Gaussian beam with waist $w_0 = 0.596 \times R_w = 0.95$ cm couples to the HE_{11} mode of the guide with >98% efficiency. Thus, it was expected that the beam formed by the converter would couple efficiently into the corrugated waveguide. Power measurements at the guide output showed that 92% of the power leaving the gyrotron exited the corrugated waveguide. Diode measurements of the beam leaving the guide showed its behavior to be that of an HE_{11} mode. Thus, the overall efficiency of the converter can be calculated, according to Eq. 3.35, at 98%.

Next, the four additional reflectors of the beam splitting mirror relay were added to the pre-bunching launcher and two mirror relay. Diode scans of the dual beam output showed two Gaussian-like beams of roughly equal power. Beam expansion measurements indicated that both beams were expanding in much the same way as the design beam. The measured beams were compared to diffraction theory predictions and good agreement was obtained. Calorimetric efficiency measurements showed that 52% of the power leaving the gyrotron was found in beam a and 42% was contained in beam b, giving an over all measured efficiency of 94%. Both experiment and theory showed that simple toroidal and sinusoidal reflector surfaces can be used to divide a fundamental Gaussian beam into two Gaussian-like beams. This technique can also be used to divide a fundamental Gaussian beam into several Gaussian-like beams. A mirror relay to produce four beams was designed by superimposing two sinusoidal ripples on the initial beam splitting mirror, mirror 3 (Fig. 3.20). Two sinusoids, one in the horizontal and one in the vertical direction, split the beam into four parts, which can than be further separated with a pyramidal mirror that completes the beam splitting process. The technique is quite general, and by altering the number of sinusoidal variations and their periods, different numbers of output beams can be produced.

Finally, the launcher and two mirror transmission line were installed in the vacuum tube and measurements of the beam exiting the tube were made. The internal configuration allowed for measurement of the beam formed by the full converter, but not the beam radiated

from the launcher. Also, because the beam waist occurs within the vacuum, corrugated waveguide tests were not possible. The internal test configuration did, however, provide an advantage over the external testing in that the chance of mode conversion from the $TE_{22,6}$ mode before the launcher was greatly reduced. As suspected, without the vacuum window to cause mode conversion between the internal and external waveguides, diode scans showed one beam with a circular, fundamental Gaussian profile. No spurious side lobes of power were observed. Measurements of the beam at several points along its propagation path showed that, just as in the external tests, the beam expands with the characteristics of the design beam.

It is interesting to note that although the pre-bunching launcher was designed for a $TE_{22,6}$ mode at 110 GHz, the converter also works well for other nearby modes. Figures 3.51 and 3.52 show the resulting wall current profiles for the $TE_{23,6}$ mode at 113 GHz and the $TE_{21,6}$ mode at 107 GHz, respectively, incident on the $TE_{22,6}$ launcher described in Table 3.1.

As seen in Figs. 3.51 and 3.52 an incident $TE_{23,6}$ mode at 113 GHz or $TE_{21,6}$ mode at 107 GHz produces a wall current profile that is nearly identical the profile produced by the $TE_{22,6}$ mode at 110 GHz (Fig 3.5).

The similar wall current profiles lead to the launching of similar beams, which propagate through the mirror transmission line in much the same manner as the design beam produced by the incident $TE_{22,6}$ mode. This property of the pre-bunching converter allows for the possibility of step-tuning the gyrotron through a series of modes while preserving the high conversion efficiency observed for the design mode.

In the internal converter experiments, the gyrotron was step-tuned from the $TE_{21,6}$ mode at 107 GHz to the $TE_{22,6}$ mode at 110 GHz, and finally to the $TE_{23,6}$ mode at 113 GHz. In each mode, a fundamental, circular Gaussian-like beam was observed at the output of the gyrotron.

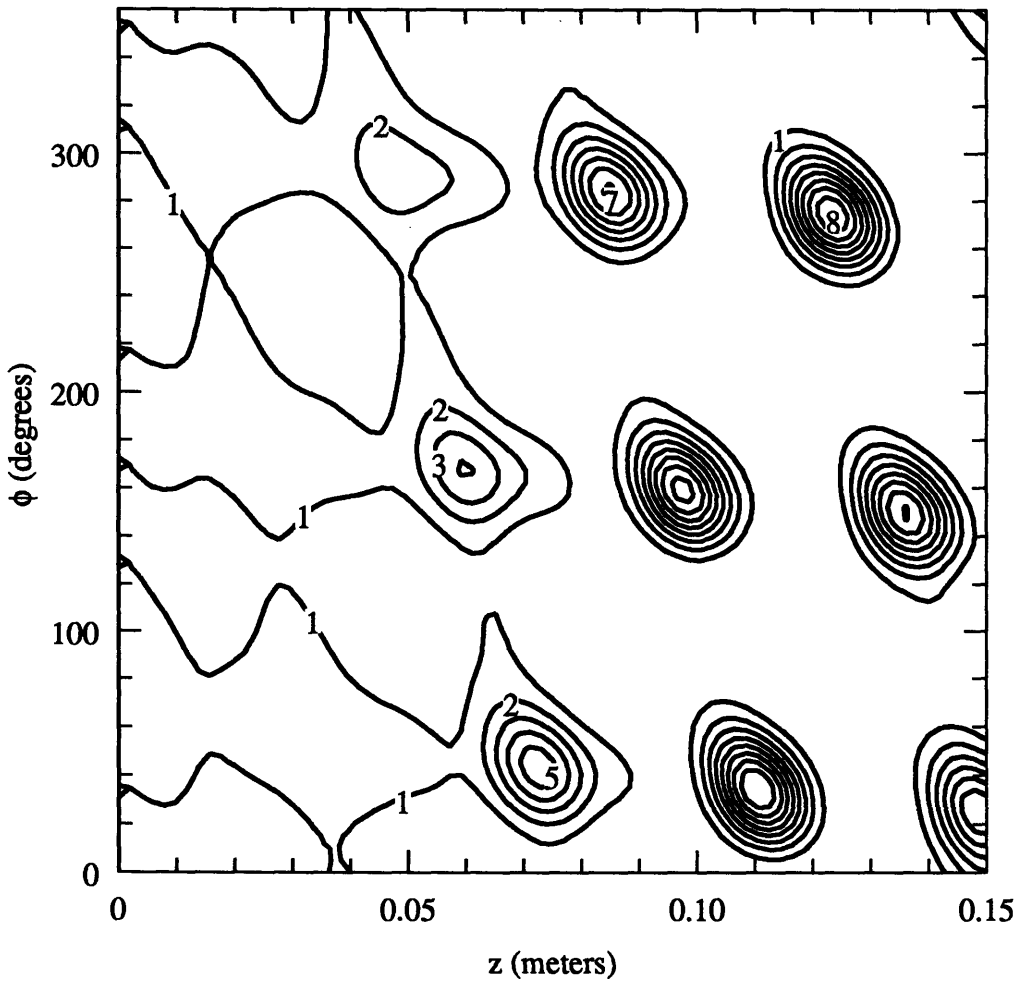

Figure 3.51 Field intensity ($|E_r|^2$) on the pre-bunching launcher wall for an incident $TE_{23,6}$ mode at 113 GHz. Lines of constant intensity, normalized to the uniform intensity of the $TE_{23,6}$ rotating mode, are plotted in steps of 1.

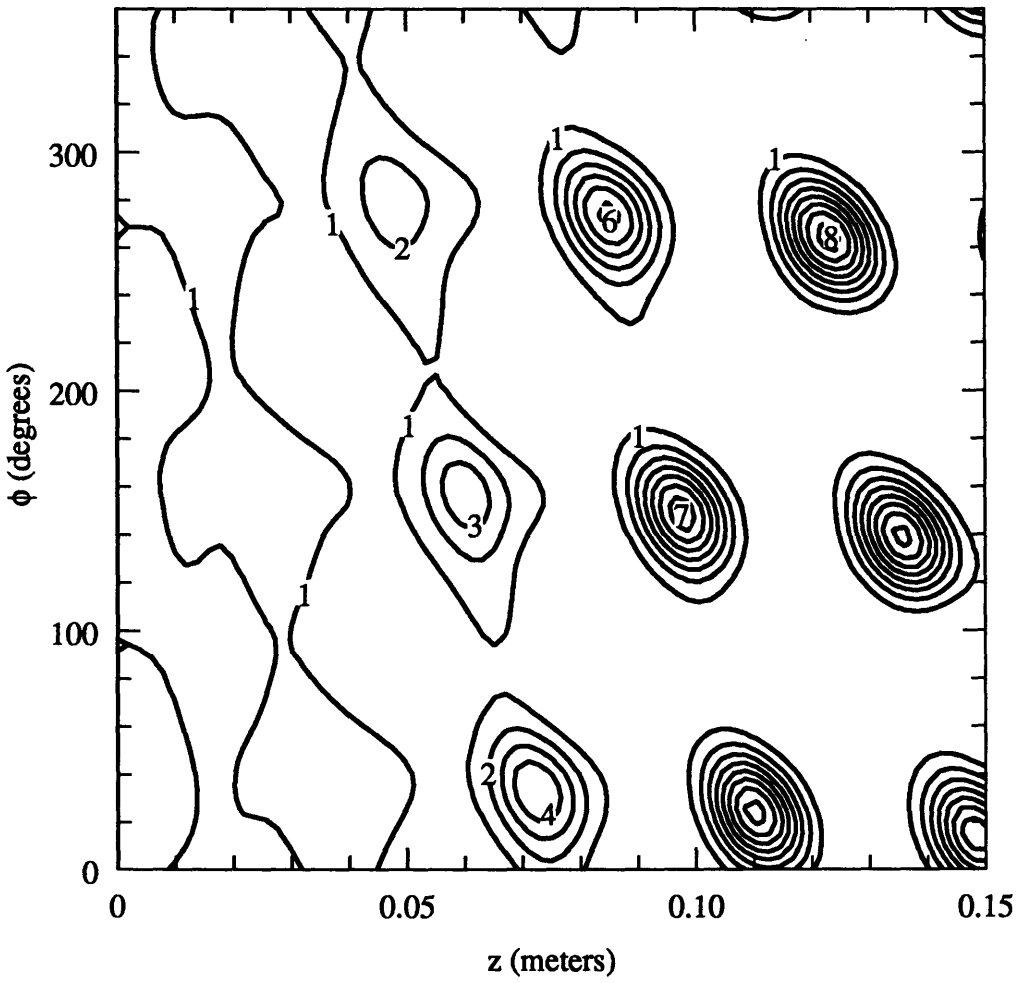

Figure 3.52 Field intensity ($|E_r|^2$) on the pre-bunching launcher wall for an incident $TE_{21,6}$ mode at 107 GHz. Lines of constant intensity, normalized to the uniform intensity of the $TE_{21,6}$ rotating mode, are plotted in steps of 1.

Chapter 4

Rotating Mode Studies

It was mentioned in earlier chapters that the annular electron beam of the gyrotron oscillator can, in general, couple to either rotation of a given high order cylindrical cavity mode. It was also mentioned that both types of quasi-optical mode converters considered in this thesis are rotation specific. The direction of the Vlasov helical cut and the sense of the helicoidal ripples in the pre-bunching launcher allow the converters to operate on either left or right rotating modes, but not both. Thus, the ability to predict and maintain one output mode rotation direction throughout the operation of gyrotron oscillators is essential to the success of the quasi-optical mode converters previously described.

There was some concern that slight misalignments of the annular beam in the gyrotron cavity could cause the output mode to switch rotation sense or to contain components of both rotations simultaneously. This concern was addressed with a theoretical and experimental study of the rotating modes of a gyrotron oscillator.

Below, the linear coupling theory for both a centered annular electron beam and an off axis beam are discussed. Experiments designed to measure the output mode rotation direction for the centered electron beam and to study the effect of electron beam misalignment are also described, and the results are compared to theory.

4.1 Linear Coupling Theory

A brief description of the linear theory for coupling between a $TE_{m,p}$ cylindrical cavity mode and an annular electron beam is found below. The linear theory for coupling to both a centered electron beam and a beam displaced from the waveguide axis are discussed.

The geometry of the problem at hand is shown in Fig. 4.1. In the figure, O marks the center of the waveguide, G marks the position of the guiding center, the point about which one electron is gyrating, and E marks the position of one electron at one particular moment in time. In the waveguide frame, the coordinates of the electron are (R,ϕ) and the coordinates of the guiding center are (R_e,ϕ_e). In the beam frame, the frame with its origin

at the guiding center, the coordinates of the electron are (r,θ). The electric field components in both frames are indicated on the figure.

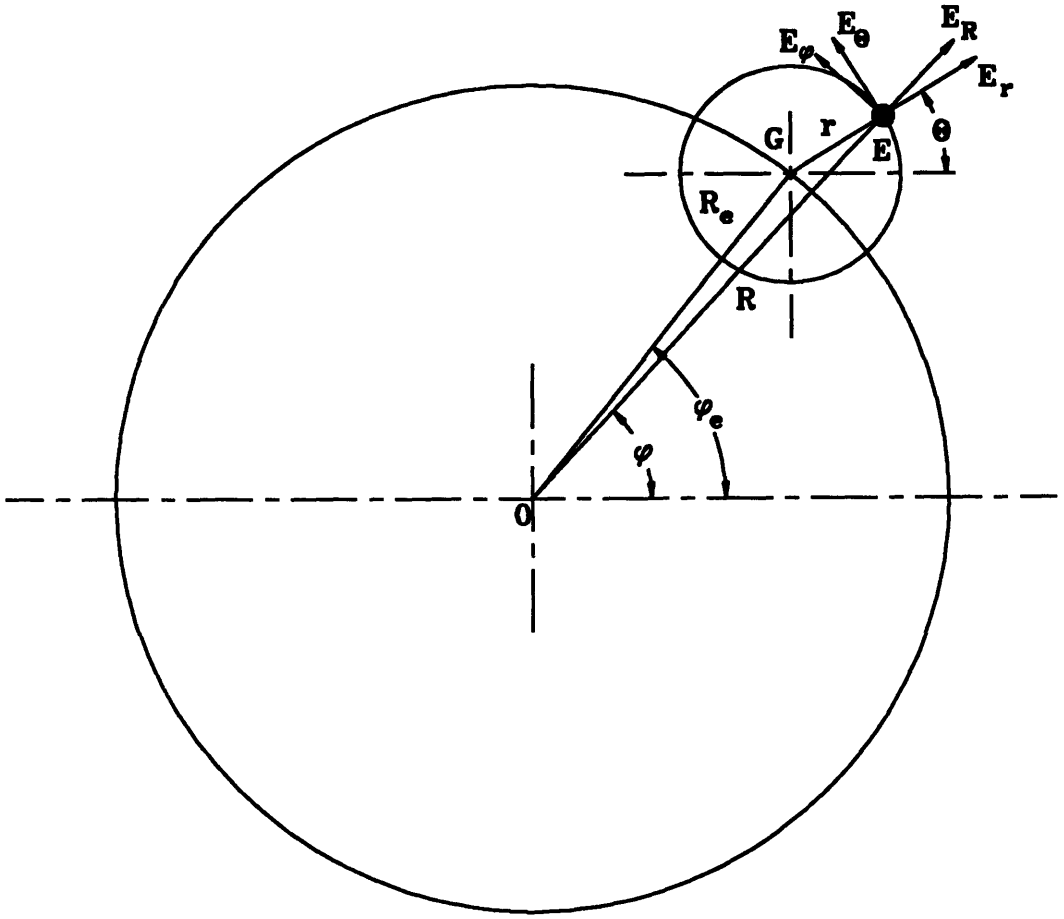

Figure 4.1 The geometry of the cylindrical waveguide cavity and annular electron beam in a typical gyrotron oscillator.

From this geometry, it is evident that the electric fields in the beam frame can be written in terms of the fields in the waveguide frame according to Eq. 4.1.

$$E_\theta = E_R \sin(\phi - \theta) + E_\phi \cos(\phi - \theta) \tag{4.1a}$$

$$E_r = E_R \cos(\phi - \theta) - E_\phi \sin(\phi - \theta) \tag{4.1b}$$

For the $TE_{-m,p}$ (left rotating) cylindrical waveguide mode, the fields in the waveguide frame are given by Eq. 4.2.

$$\mathbf{E} = \left[E_r\hat{r} + E_\phi\hat{\phi}\right] e^{i(-m\phi+k_z z-\omega t)} \tag{4.2a}$$

$$\mathbf{E} = \eta_0 H_0 e^{-im\phi}\left[\frac{mk}{k_r^2 r}J_m(k_r r)\hat{r} - \frac{ik}{k_r}J'_m(k_r r)\hat{\phi}\right] e^{i(k_z z-\omega t)} \tag{4.2b}$$

where $k = \frac{\omega}{c}$; ω is the angular frequency in radians; c is the speed of light; $k_r = \nu_{mp}/R_w$, where ν_{mp} is the pth zero of J'_m and R_w is the waveguide radius; $k_z = \sqrt{k^2 - k_r^2}$; η_0 is the free space wave impedance; and H_0 is a constant.

Substituting Eqs. 4.2a and 4.2b into Eqs. 4.1a and 4.1b and making use of Graf's formula gives the left rotating electric field in the beam frame [32], given by Eqs. 4.3 and 4.4.

$$\mathbf{E_r} = iA\sum_{n=-\infty}^{\infty}\frac{n}{k_r r}e^{-i(m-n)\phi_0}J_{m-n}(k_r R_e)J_n(k_r r)e^{-in\phi} \tag{4.3}$$

$$\mathbf{E}_\phi = A\sum_{n=-\infty}^{\infty}e^{-i(m-n)\phi_0}J_{m-n}(k_r R_e)J'_n(k_r r)e^{-in\phi} \tag{4.4}$$

where ϕ_e is the azimuthal angle between the waveguide origin and the guiding center, R_e is the vector between the waveguide origin and the guiding center, n is the harmonic index, and $A = -i\eta_0 H_0 \frac{k}{k_r}e^{i(k_z z-\omega t)}$.

From Eqs. 4.3 and 4.4, the synchronous components of the fundamental ($n = 1$) left rotating ($TE_{-m,p}$) electric field can be written as [32]:

$$\mathbf{E_r} = \frac{iA}{k_r r}J_{m-1}(k_r R_e)J_1(k_r R_e)e^{-i(m-1)\phi_0} \tag{4.5}$$

$$\mathbf{E}_\phi = AJ_{m-1}(k_r R_e)J'_1(k_r R_e)e^{-i(m-1)\phi_0} \tag{4.6}$$

Coupling between the electric field and the electron beam is proportional to $\mathbf{E}\cdot\mathbf{J}$, where the perturbed current, $\mathbf{J}$, is proportional to $\mathbf{E}$. Therefore, it can be seen from Eqs. 4.5 and 4.6 that coupling the left rotating wave is proportional to $J^2_{m-1}(k_r R_e)$. Similarly, coupling to the right rotating wave is proportional to $J^2_{m+1}(k_r R_e)$.

For a gyrotron oscillator with a symmetric annular beam centered about the axis, the rotation direction of the output mode can be selected by choosing a beam radius near the peak of the function $J^2_{m\pm1}(k_r R_e)$. For lower order modes, the right and left rotation

coupling peaks are well separated, and placing the beam on the desired peak is not difficult. However, as the azimuthal mode number, m, increases, the coupling peaks draw closer together in radius and beam placement becomes more critical, as shown in Fig. 4.2.

Slight misalignments of the gyrotron tube can cause an asymmetric or off-center beam in the cavity. The linear theory for a gyrotron with an eccentricity of the electron beam in the cavity was developed by Dumbrajs and Liu [33]. The starting current, or the inverse of coupling strength, for a mode coupling to the off axis beam is given by [33]:

$$I_{st} = -\frac{\pi k_c^2 R_w^2 v_{||} \gamma_0 \left(1 - m^2/(k_c^2 R_w^2)\right) J_m^2(k_c R_w)}{\eta_0 \mu_0 \left(1 - \frac{s^2\lambda^2}{4L^2}\right) Q \sum_{i=1}^{4} Re\left[\frac{p_i}{A}\right]} \tag{4.7}$$

where $k_c \sim k_r$ for the gyrotron interaction which occurs near cutoff, $v_{||}$ is the perpendicular velocity of the electrons, $\gamma_0 = \frac{1}{\sqrt{1-(|v_0|/c)^2}}$, v_0 is the electron velocity, $\eta_0 = \frac{|e|}{m_0}$, μ_0 is the free space permeability, L is the cavity length, λ is the wavelength, and s is the longitudinal mode index. The terms p_i and Q are given in [33]. The linear coupling theory in [33] was derived for an ideal beam with no guiding center spread.

For the two rotations of the same mode, the ratio of starting currents simplifies to:

$$\frac{I_{st}^+}{I_{st}^-} = \frac{\sum_{q=-\infty}^{\infty} J_q^2(k_c d) J_{m-q-1}^2(k_r R_e)}{\sum_{q=-\infty}^{\infty} J_q^2(k_c d) J_{-m-q-1}^2(k_r R_e)} \tag{4.8}$$

where d is the displacement of the electron beam from the centered position.

The $TE_{16,2,1}$ mode can be used as an example to illustrate the theoretical prediction of the effect of beam offset on output mode rotation direction. The ratio of starting currents, as calculated by Eq. 4.8, for the $TE_{16,2,1}$ mode generated near cutoff at 146 GHz coupling to an electron beam of radius 0.56 cm is plotted against beam displacement, d, in Fig. 4.3. In regions of displacement where $\frac{I_{st}^+}{I_{st}^-}$ is > 1, left rotation is expected, and where $\frac{I_{st}^+}{I_{st}^-}$ is < 1 right rotation is expected. According to Eq. 4.8, the rotation for the centered beam should be left, and a switch to right rotation should occur at a beam displacement of about .085 cm.

Experiments designed to determine the effect of tube misalignment, or beam offset, on output mode rotation direction are described below.

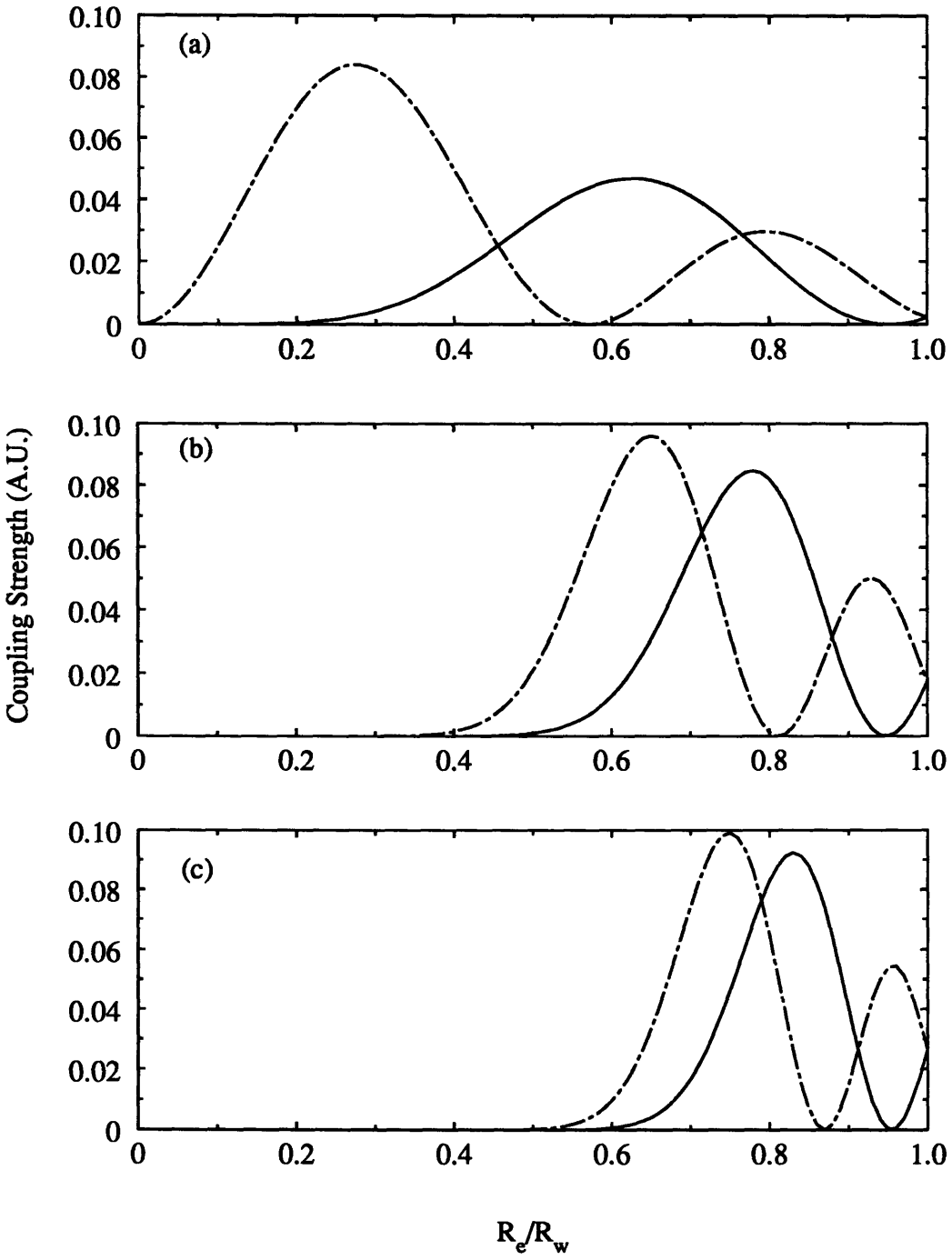

Figure 4.2 Theoretical coupling to a centered beam for the (a) $TE_{2,2}$ mode, (b) $TE_{10,2}$ mode, and (c) the $TE_{18,2}$ mode at 146 GHz. Coupling strength is plotted against normalized beam radius. The dashed lines indicate the coupling to left rotating mode and the solid lines indicate coupling to the right rotating mode.

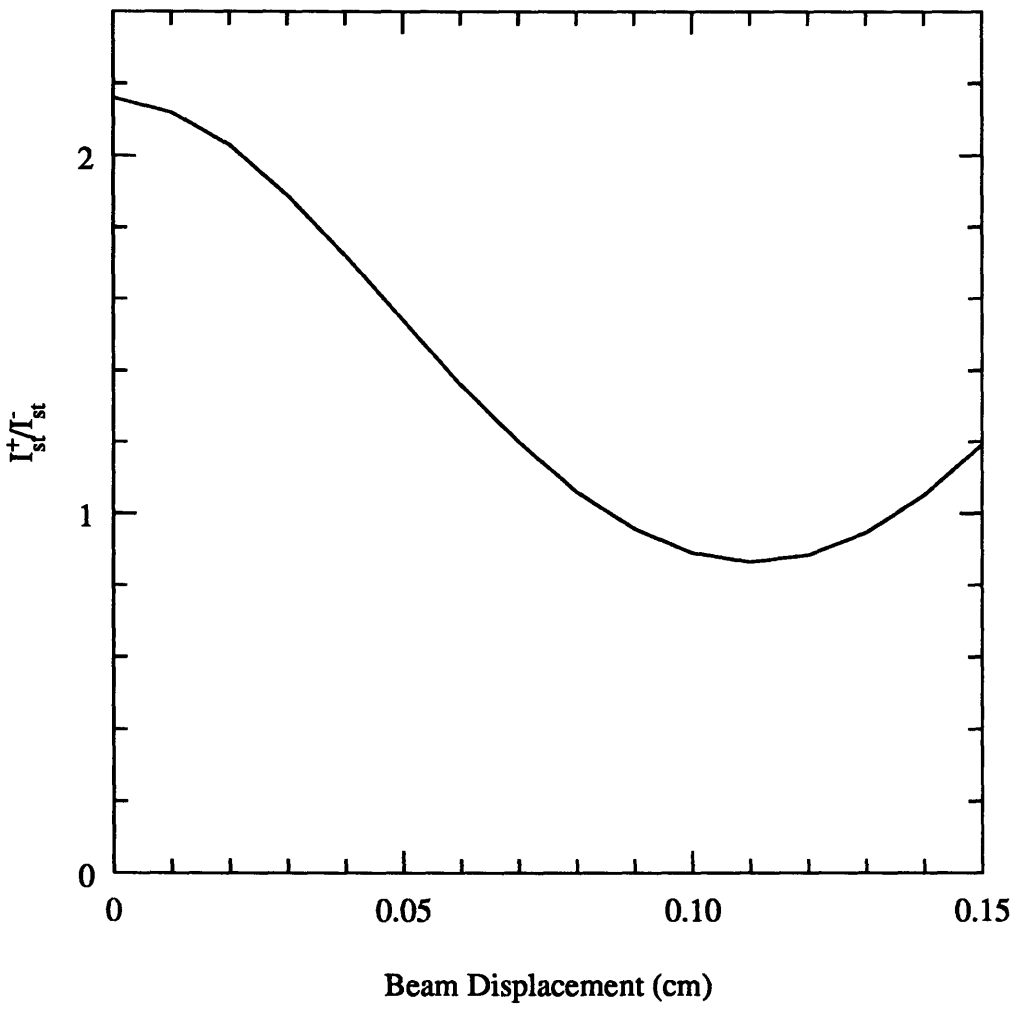

Figure 4.3 Theoretical ratio of starting currents for an off axis electron beam with radius 0.56 cm coupling to the $TE_{16,2,1}$ mode generated near cutoff at 146 GHz.

4.2 Tube Misalignment Experiments

Experiments were performed on a megawatt power level, 3μs pulsed gyrotron [5]. In the first set of experiments involving beam misalignment in the cavity, the rotation sense of the $TE_{16,2,1}$ mode operating at 146 GHz was determined using matched right-hand and left-hand Vlasov launchers and focussing reflectors. As described in Chapter 2, the launcher and reflector are configured such that radiation rotating in the direction of the helical cut is radiated from the straight edge of the launcher, intercepted by the doubly curved reflector, and focussed to a Gaussian-like focal spot approximately 50 cm away, while radiation rotating in the opposite sense spills from the helical cut and is not focussed by the reflector. The schematic of the Vlasov-type converter is found in Fig. 1.2.

In order to study the effect of tube misalignment on rotation direction of the $TE_{16,2,1}$ mode, the vacuum tube, which houses the electron beam tunnel, cavity, and collector, was moved incrementally away from the centered position. The electrons continue to follow the electric field lines, which are no longer parallel to the tube. Thus, moving the tube has the effect of changing the location of the electron beam in the cavity. The tube was held fixed at the gun end so that the electron optics remained virtually the same for all values of displacement. At each tube position, the total power, as well as power at the left-hand and right-hand foci, was measured with a 10 cm Scientech laser calorimeter. The process was then repeated after changing the direction of the magnetic field in the cavity and at the cathode, leaving the field amplitudes and all other parameters the same. This second measurement was used to determine the symmetry of the diagnostic system. The only result of changing the direction of the magnetic field should have been to change the rotation sense of the output mode at each tube position.

The results of the tube misalignment experiments are shown in Fig. 4.4. The radius of the electron beam was experimentally determined to be 0.56 cm, which corresponds to a ratio of $\frac{R_e}{R_w}$ of 0.73. Both the linear coupling theory for the centered beam and the asymmetric beam (Fig. 4.3), which are identical at zero beam displacement, predict that when centered in the cavity, the specified electron beam should couple to the left rotating $TE_{16,2,1}$ mode. At the centered beam position, only left rotation was observed (Fig. 4.4). Figure 4.3 indicates that a switch from left rotation to right is expected at a beam displacement of approximately $\pm$0.085 cm from center. Figure 4.4 shows that the rotation switch was experimentally observed at approximately 0.08 cm and -0.085 cm, which is in good agreement with the theory.

Reversing the direction of the magnetic field in the cavity and repeating the tube displacement experiments indicated that the measurements were symmetric and reproducible to within $\pm$ 5%.

Thus, both the linear coupling theory and the experimental study show that significant beam misalignments, approximately 0.08 cm in the case of a $TE_{16,2,1}$ mode at 146 GHz, are possible before a rotation switch occurs. These results indicate that slight beam misalignments are not hazardous to the operation of a Vlasov or other type of rotation sensitive mode converter.

The alignment experiments also showed that the gyrotron output power remains relatively constant as the beam is displaced from the centered position (Fig. 4.4). This result was unexpected because the linear theory predicts that the coupling between the beam and the rf field is greatly reduced at substantial beam offset.

Figure 4.4 shows an abrupt transition from the left rotating to the right rotating $TE_{16,2}$ mode at beam displacements of $\sim \pm 0.08$ cm. The same type of behavior was seen in a theoretical study performed at the Naval Research Laboratory [34] which investigated coupling to the $TE_{\pm 6,2,1}$ counter rotating modes. In [34], the power and rotation direction of the output mode were calculated as a function of beam radius for the centered beam case. The theoretical study predicted an abrupt transition from the left rotating to the right rotating $TE_{6,2}$ mode, similar to the transition observed in the experiments discussed above. The nonlinear multimode theory described in [34] also predicted nearly constant output power at varying beam radii, as was observed in the $TE_{16,2}$ mode misalignment experiments.

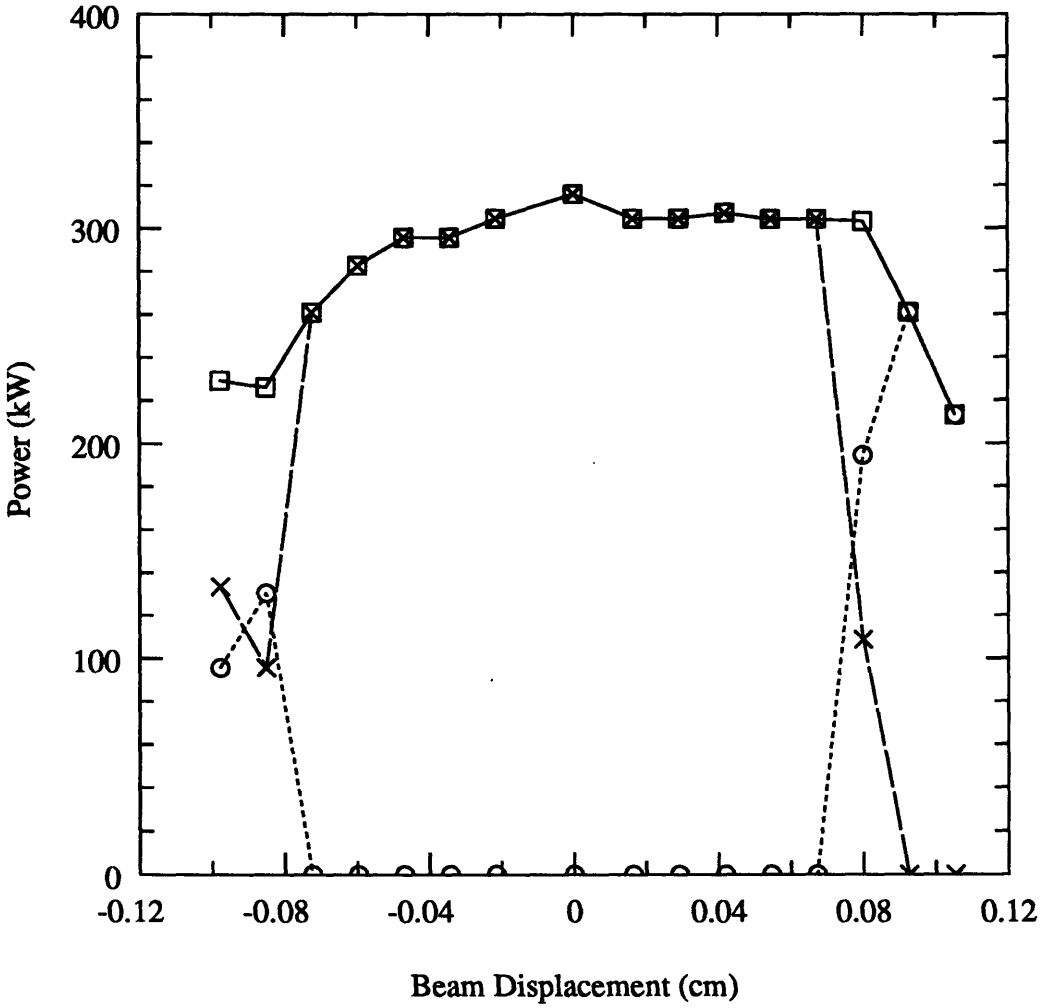

Figure 4.4 Results of the tube misalignment experiments. Total power is indicated by the squares, power in the right rotating $TE_{16,2}$ mode by the circles, and power in the left rotating $TE_{16,2}$ mode by the x's.

4.3 Step Tuning Experiments

In a second set of experiments, a multi hole directional coupler [35], shown in Fig. 4.5, was used to determine relative amounts of left and right rotating radiation for a given mode. The coupler consists of nine coupling holes at a constant axial position around the azimuth of a circular waveguide coupling through the narrow wall of a fundamental rectangular waveguide, in this case WR6. The coupler is configured such that a mode rotating in the right-handed sense will add constructively in arm 2 of the fundamental waveguide and destructively in arm 1, and the opposite adding will occur for a mode rotating in the left-handed sense. By comparing the signals in the two arms of the directional coupler, a measure of the relative amounts of left and right rotating components in the output radiation mode mix can be made.

The matching condition between the two waveguides is given by [35]:

$$k_g = \left(\frac{-m}{R}\right) + \left(\frac{2\pi}{s}\right) \tag{4.9}$$

where k_g is the parallel wave number for the fundamental mode of the rectangular waveguide, m is the azimuthal mode number of the cylindrical waveguide mode, R is the radius of the cylindrical waveguide, and s is the spacing of the coupling holes.

For the desired coupling between the $TE_{16,2}$ mode in a guide with radius R=1.746 cm and the fundamental TE_{10} mode in a WR6 waveguide at 146 GHz, the coupling hole spacing, calculated with Eq. 4.9, is 0.19 cm. The rotating mode coupler was designed to provide greater than 30 dB directivity for the $TE_{16,2}$ mode at 146 GHz. At 123.5 GHz, the directivity is reduced to 5.6 dB.

The directional coupler was constructed and was used to examine the rotation mode mix with the electron beam centered in the cavity as the gyrotron was step tuned by varying the cavity magnetic field. Five $TE_{m,2,1}$ modes, m = 13 to 17, were excited from 123.5 to 153.5 GHz.

For each of the modes, the signals in the two arms of the coupler were compared and the relative signal strengths are plotted in Fig. 4.6. Figures 4.7–4.11 show the centered beam coupling curves for the five modes under consideration. The beam extents, calculated from the experimental parameters and normalized to the cavity radius, are shown on each of the coupling curves.

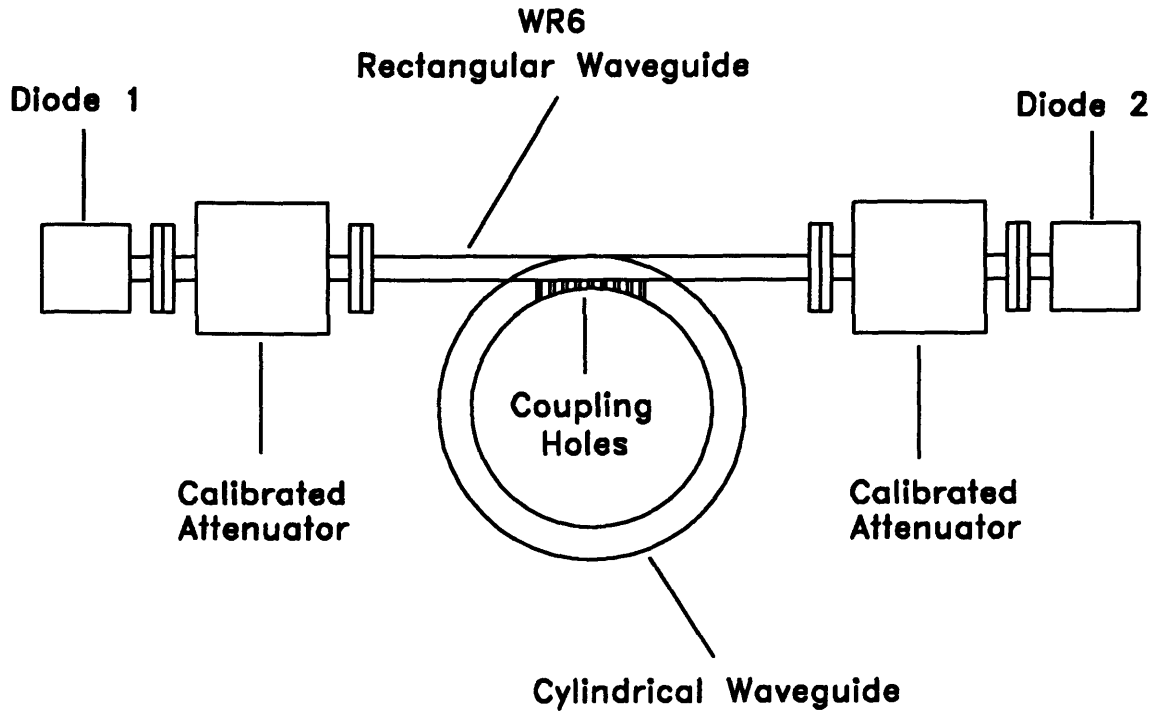

Figure 4.5 Schematic of the rotating mode directional coupler for determining the rotation of the gyrotron output mode.

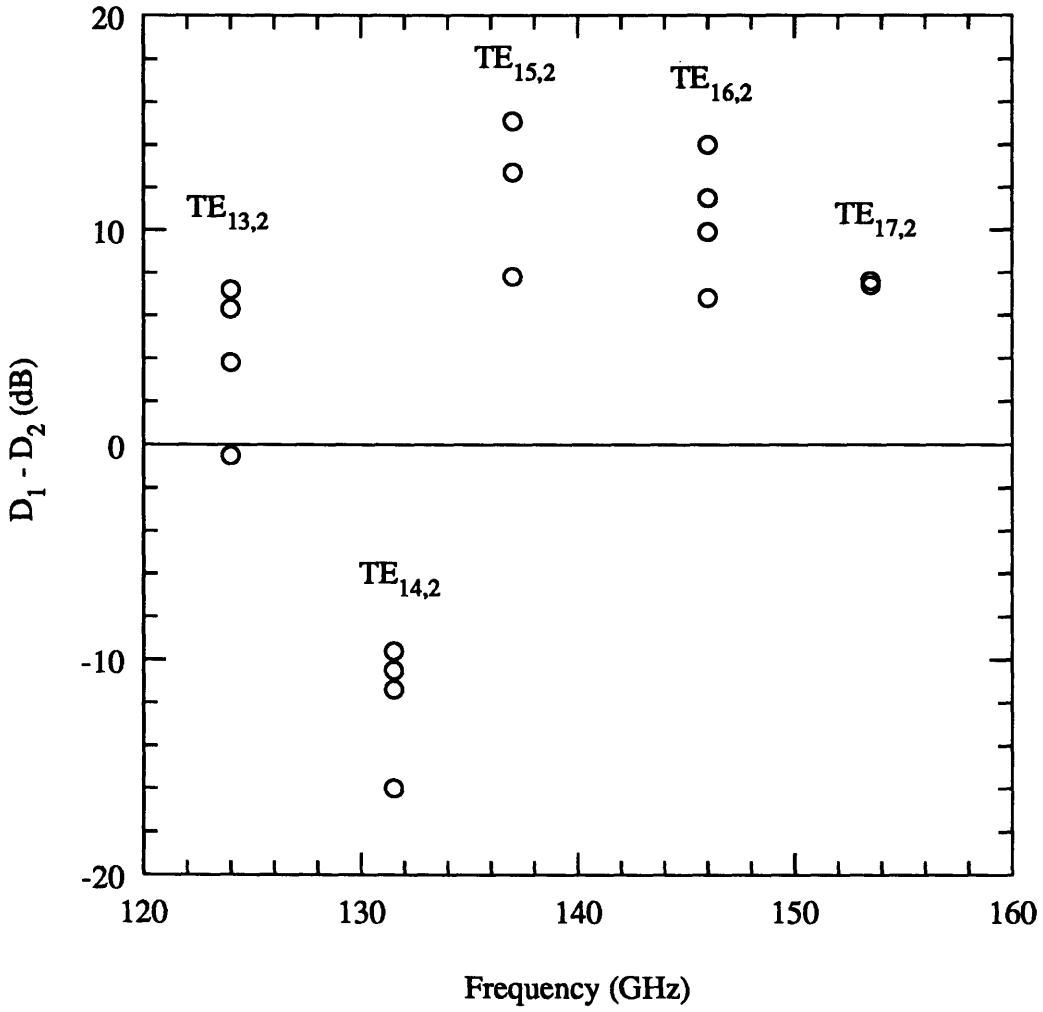

Figure 4.6 Results of the step tuning experiments. The relative signal strengths in the two arms of the coupler are plotted for five modes.

Figure 4.7 shows that beam falls near the peak of the left rotating $TE_{17,2}$ coupling curve, which suggests that a left rotating output mode is expected. Figure 4.6 shows that the signal in arm 1 of the directional coupler was approximately 7 dB higher than the signal in arm 2, indicating that the left rotating mode was dominant.

Figures 4.8 and 4.9 show that left rotating $TE_{16,2}$ and $TE_{15,2}$ modes were expected based on the linear coupling theory and calculated beam radius. Figure 4.6 shows that dominant left rotating modes were observed with the directional coupler. The scatter in the data points is due to reflections in the arms of the coupler, caused by machining errors and imperfect joints between the circular and rectangular waveguides.

In Figure 4.10, the beam intersects the $TE_{14,2}$ coupling curves at a point where the right and left rotating coupling strengths are approximately equal, with the right mode slightly stronger. The signal in arm 2 of the directional coupler was stronger than the signal in arm 1 (Fig. 4.6) indicating that the right rotating mode was the dominant part of the output mode.

Figure 4.11 shows that the beam intersects the linear coupling curves near the right rotating peak of the $TE_{13,2}$ mode. However, the directional coupler showed that the signal observed in arm 1 of the directional coupler was several dB larger than the signal observed in arm 2, which is characteristic of a dominant left rotating wave. It is believed that the reduced directivity at 123.5 GHz, in combination with reflections due to machining errors, caused this discrepancy between theory and experiment for the $TE_{13,2}$ mode.

Thus, the directional coupler was able discriminate between different rotating modes near its design frequency, 146 GHz. With careful machining, such a directional coupler could serve as a useful diagnostic for verifying that the beam is aligned in a gyrotron cavity and coupling to the correct rotation of the rf field.

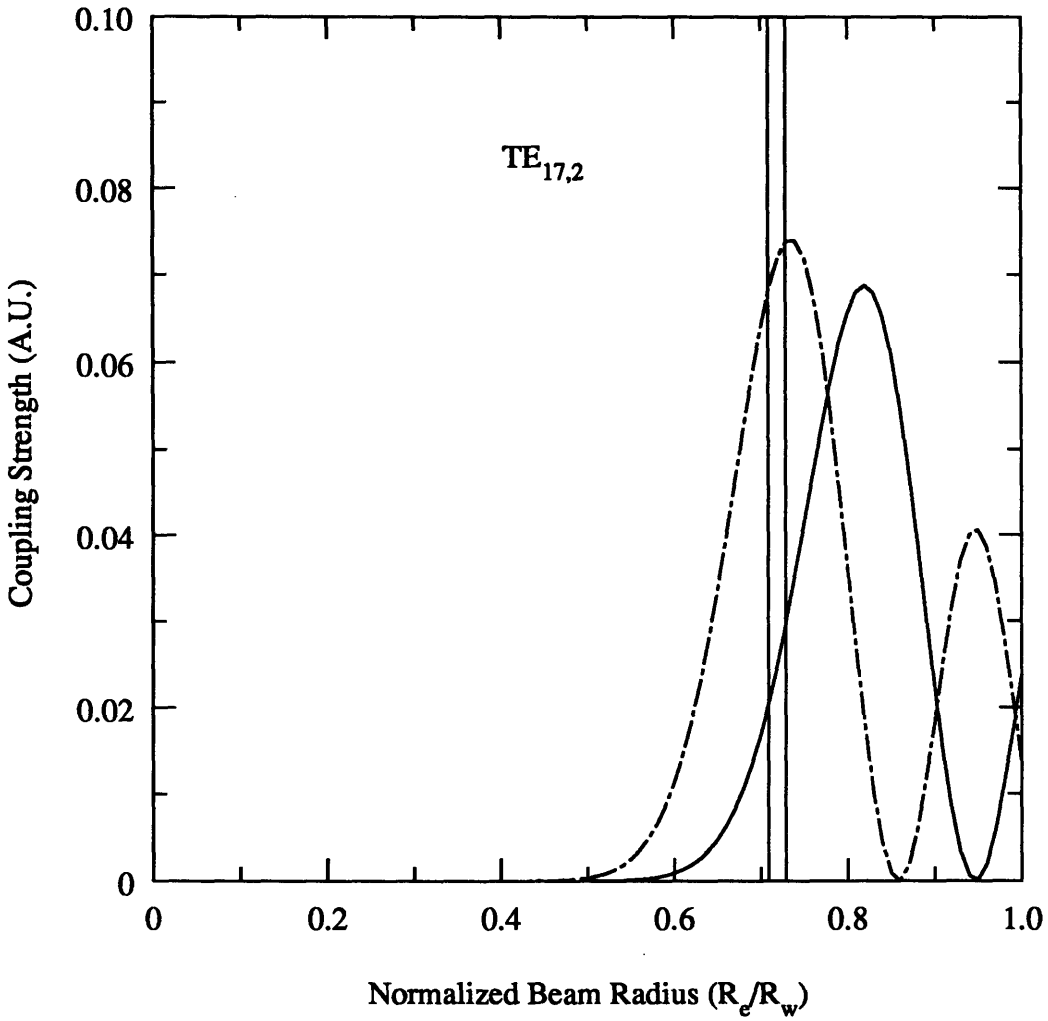

Figure 4.7 Theoretical coupling to a centered beam for the $TE_{17,2}$ mode at 153.5 GHz. The beam extents, shown as the vertical solid lines, were calculated from the experimental parameters. The dashed lines indicated coupling to the left rotating mode and the solid lines indicate coupling to the right rotating mode.

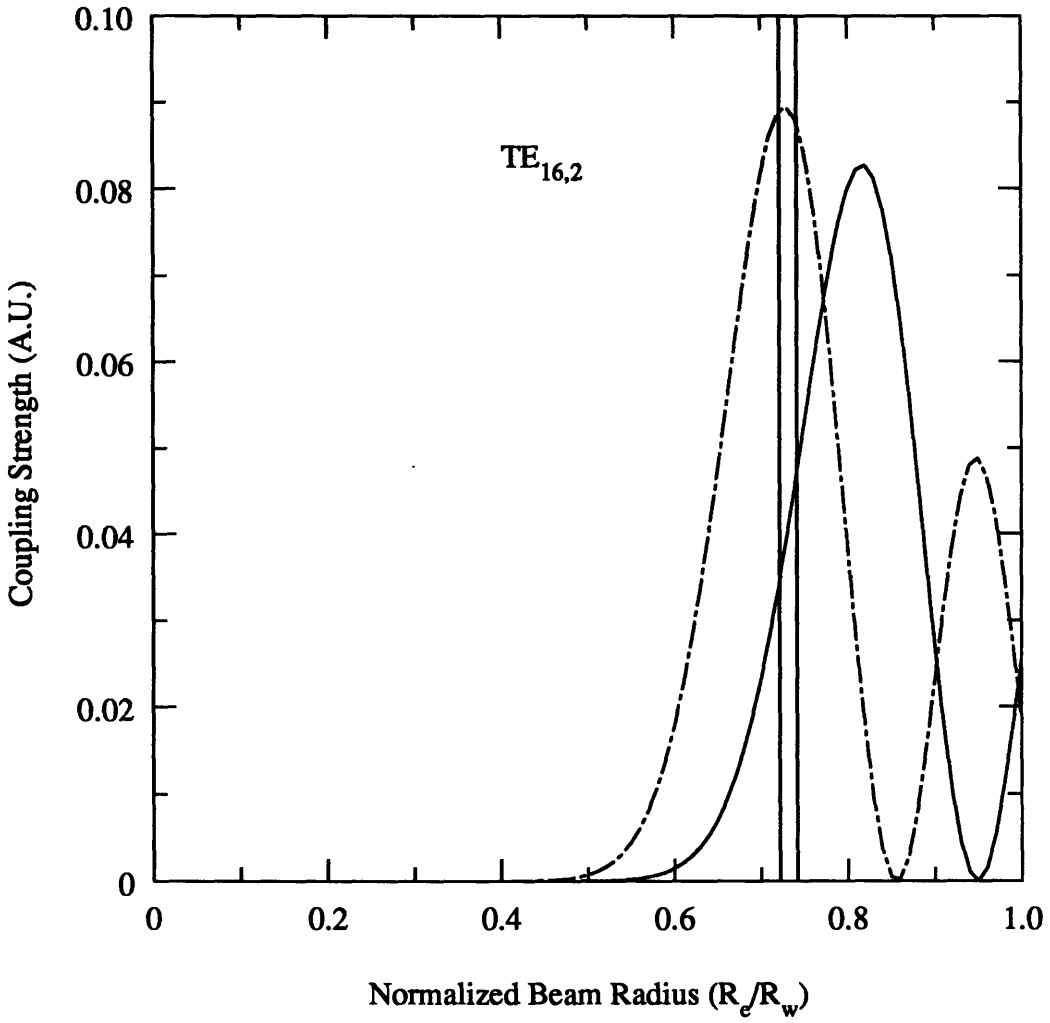

Figure 4.8 Theoretical coupling to a centered beam for the $TE_{16,2}$ mode at 146 GHz. The beam extents, shown as the vertical solid lines, were calculated from the experimental parameters. The dashed lines indicated coupling to the left rotating mode and the solid lines indicate coupling to the right rotating mode.

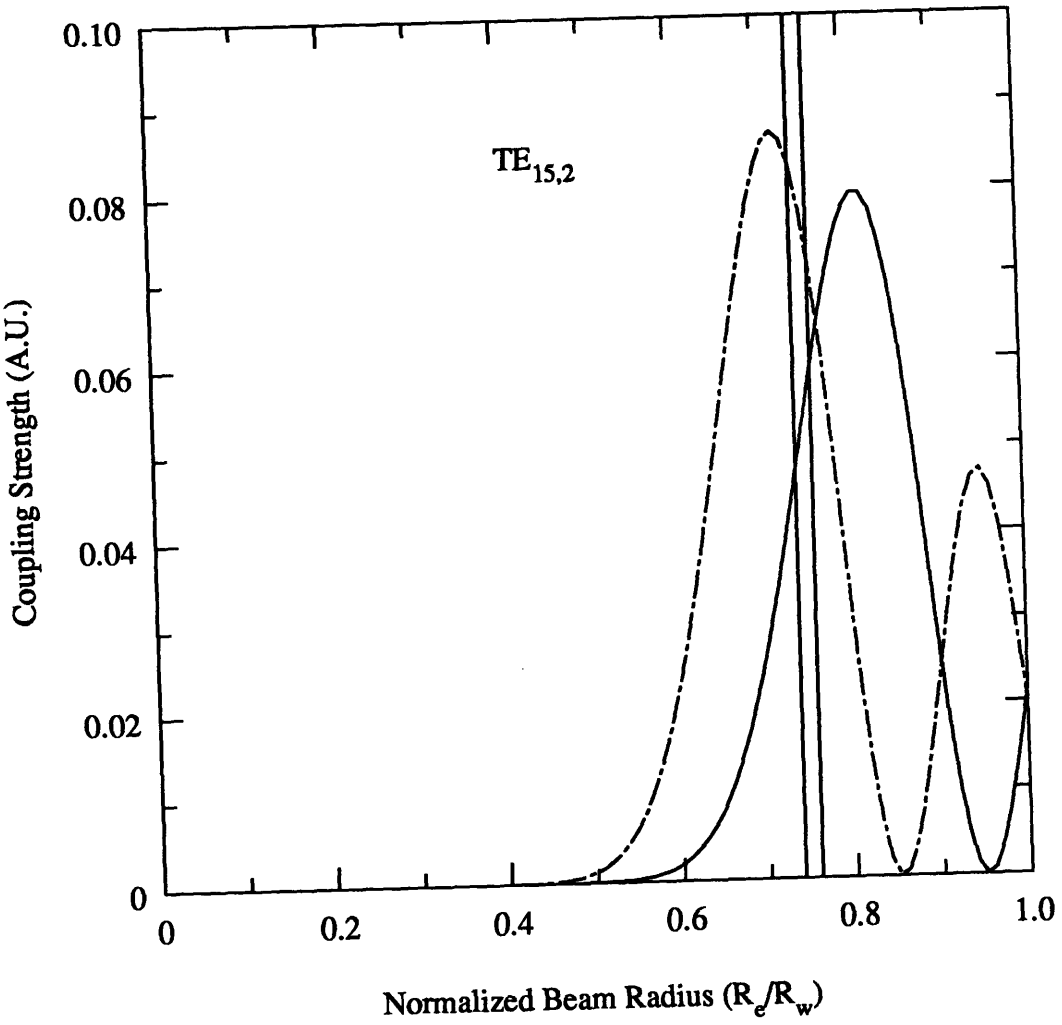

Figure 4.9 Theoretical coupling to a centered beam for the $TE_{15,2}$ mode at 138.5 GHz. The beam extents, shown as the vertical solid lines, were calculated from the experimental parameters. The dashed lines indicated coupling to the left rotating mode and the solid lines indicate coupling to the right rotating mode.

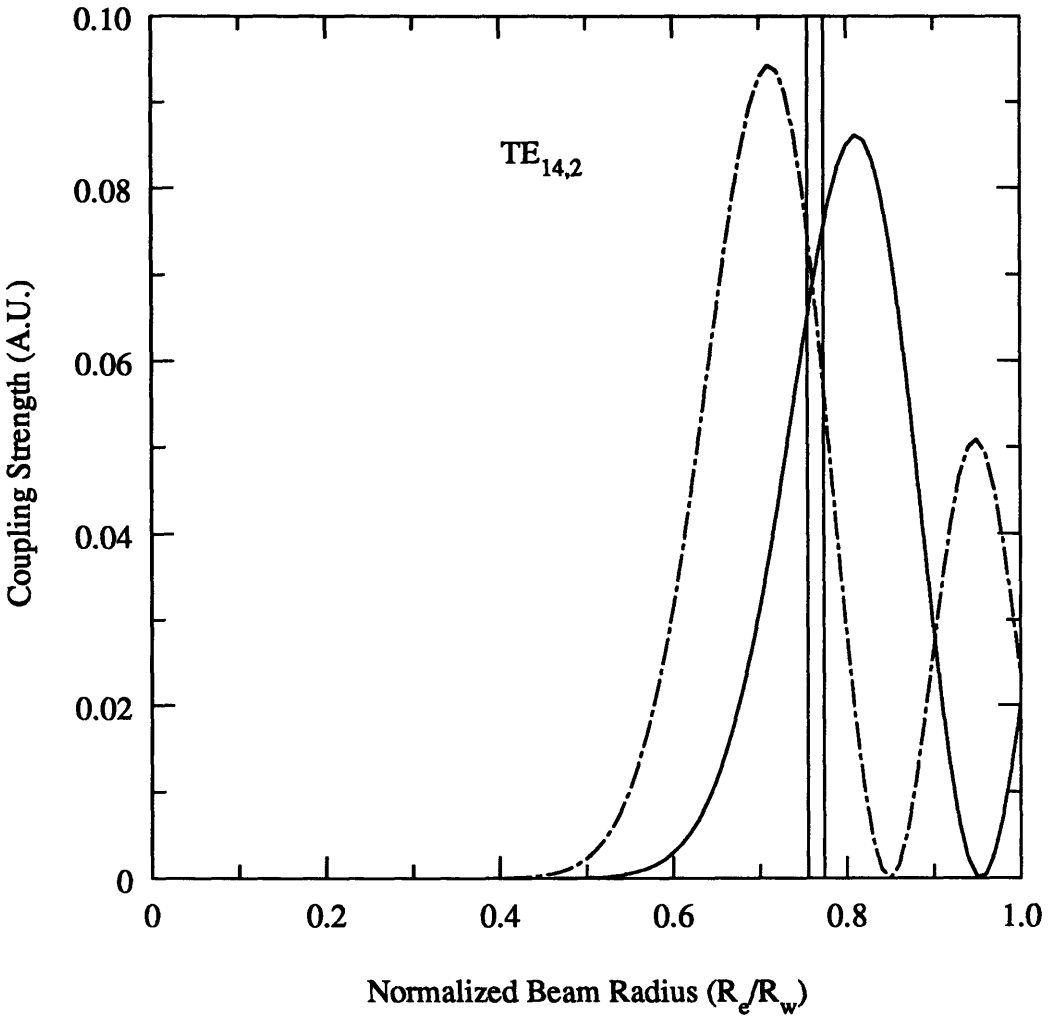

Figure 4.10 Theoretical coupling to a centered beam for the $TE_{14,2}$ mode at 131 GHz. The beam extents, shown as the vertical solid lines, were calculated from the experimental parameters. The dashed lines indicated coupling to the left rotating mode and the solid lines indicate coupling to the right rotating mode.

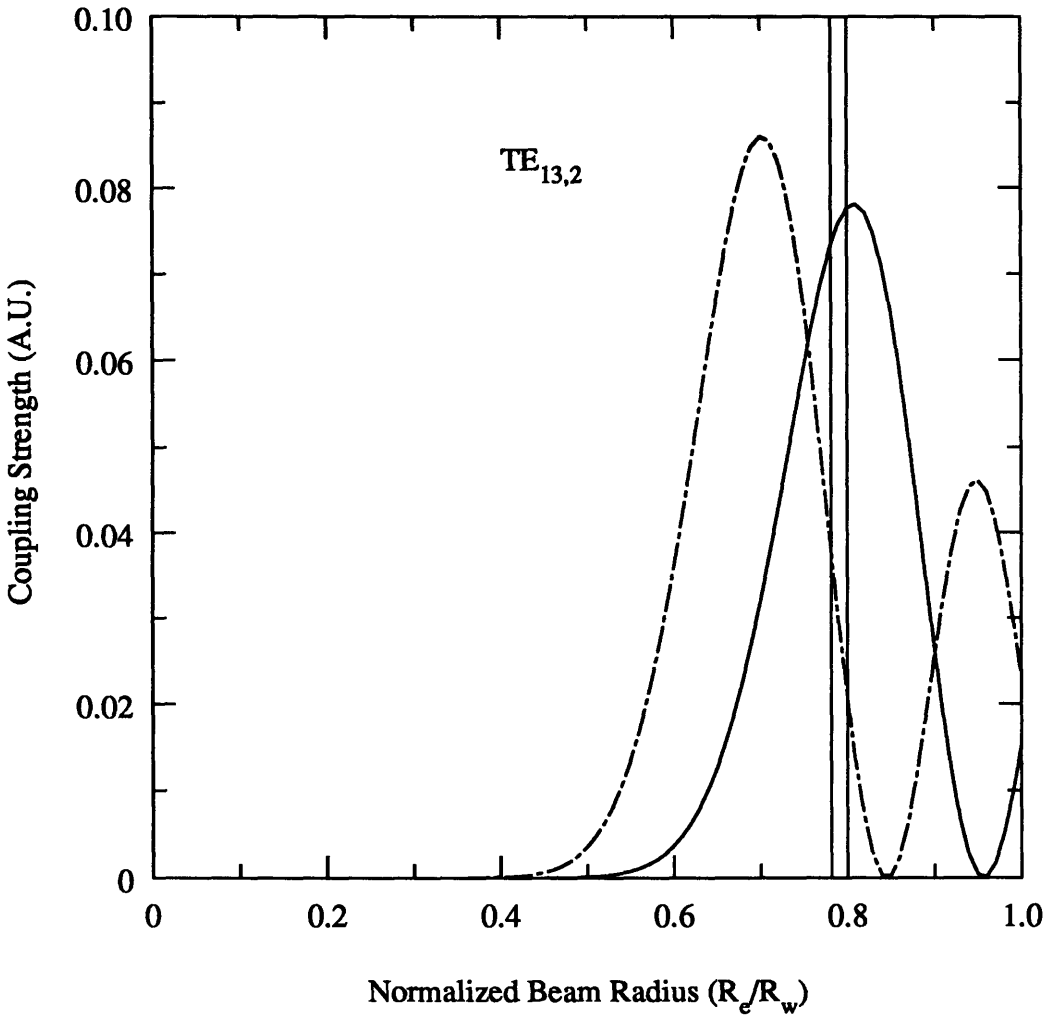

Figure 4.11 Theoretical coupling to a centered beam for the $TE_{13,2}$ mode at 123.5 GHz. The beam extents, shown as the vertical solid lines, were calculated from the experimental parameters. The dashed lines indicated coupling to the left rotating mode and the solid lines indicate coupling to the right rotating mode.

4.4 Discussion of Results

A study of coupling to the counter rotating $TE_{\pm m,2,1}$ modes of a gyrotron oscillator was made. Two experiments were performed and the results were compared to theory. The alignment experiments, which employed matched left and right Vlasov converters, showed that the centered electron beam coupled to the left rotating $TE_{16,2,1}$ mode, as predicted by the linear coupling theory. It was observed that the beam could be displaced $\sim \pm 0.08$ cm from the centered position in the cavity before a change in the rotation sense of the output mode was detected. This displacement agrees well with the linear coupling theory for an off-axis beam, which predicts a switch in rotation direction at a displacement of 0.085 cm. Because beam alignments to within ± 0.025 cm are easily achievable in practice, the study suggests that predicting and maintaining the output mode rotation sense is possible and that slight misalignments of the beam will not prevent the use of a rotation specific output mode converter.

In the second set of experiments, a directional coupler was used to determine the relative amounts of right and left rotating components of the output mode as the gyrotron was step tuned from the $TE_{13,2}$ mode at 123.5 GHz to the $TE_{17,2}$ mode at 153.5 GHz. Although machining errors limited the success of the experiments, the coupler was able to discriminate between counter rotations >6 dB directivity for the design mode, the $TE_{16,2}$ at 146 GHz. The coupler was also able to discriminate between the left and right rotating $TE_{14,2}$, $TE_{15,2}$ and $TE_{17,2}$ modes. The observed rotation directions for these modes is in agreement with linear coupling theory predictions for a centered electron beam, indicating that such a coupler could be a useful diagnostic in aligning a gyrotron tube and verifying output mode rotation direction.

Chapter 5

Summary

An investigation of quasi-optical mode converters for high order mode gyrotrons was made. Two converters, the Vlasov-type and pre-bunching converters, were examined. A Vlasov-type converter was designed to transform the $TE_{16,2}$ cylindrical waveguide mode at 146 GHz to a Gaussian beam in free space. The preliminary converter design was made with the geometric optics approximation. Both experimental results and vector diffraction theory predictions showed that only 75% of the near field launcher radiation pattern fell within the bounds of the geometric optics predicted pattern. The size of the reflector was, consequently, chosen on the basis of the diffraction theory prediction, but the reflector shape was calculated with geometric optics theory.

Tests on a MW power level gyrotron showed that the converter directed 95% of the incident $TE_{16,2}$ power to a small, Gaussian-like focus in the far field. The focal plane measurements were in good agreement with predictions of vector diffraction theory. In addition to the $TE_{16,2}$ focus, two other low level focii, corresponding to the mode converted $TE_{15,2}$ and $TE_{17,2}$ modes, were observed in the far field. This observation pointed out a useful property of the Vlasov-type converter. Each mode that is incident on the launcher appears as a distinct focal spot in the far field. The Vlasov-type converter is, thus , a good diagnostic for determining the mode content of an incident mode mix.

Beam expansion measurements, which were in good agreement with predictions of vector diffraction theory, showed that although the main beam exhibited a Gaussian profile in the focal plane, only 88% of the power, or 88% $\times$ 95% = 83% of the incident $TE_{16,2}$ power, was contained in the TEM_{00} mode. Aberrations to the phase fronts caused a non-Gaussian expansion of the beam beyond the focus. These phase aberrations are the result of the rays not predicted by geometric optics being focussed by the reflector surface designed with geometric optics.

Directing the beam into a corrugated waveguide confirmed the total conversion efficiency inferred from the beam expansion measurements. The corrugated guide experiments showed that 82.5% of the $TE_{16,2}$ power leaving the gyrotron was converted to the HE_{11} mode of the guide.

The vector diffraction theory, developed as part of this thesis, allows for the possibility of improving the reflector design and increasing the efficiency of the Vlasov-type converter. However, fundamental limitations involving the large azimuthal expansion angle for higher order modes renders the Vlasov-type converter impractical for certain classes of modes. The more useful solution was to modify the launcher, rather than modify the reflector design.

A pre-bunching converter, which is a modification on the Vlasov-type, was designed to transform the $TE_{22,6}$ cylindrical waveguide mode at 110 GHz to a Gaussian beam in free space. The converter consists of an irregular waveguide section, followed by a step cut launching aperture and two reflectors in an open mirror transmission line. The goal of the irregular waveguide section is bunch the radiation into Gaussian bundles prior to the launch so that a more controlled, well defined beam is radiated from the aperture. The shaping and steering reflectors that follow are designed with Gaussian optics and modified with vector diffraction theory. Even with the diffraction theory design modifications, the simple toroidal mirror shape is preserved.

The converter was built and tested on a MW power level gyrotron operating in the $TE_{22,6}$ mode at 110 GHz. Experiments were performed with the converter both external and internal to the gyrotron vacuum tube. With the converter in the external configuration, measurements of the beam radiated from the launcher and the beam at the output of the full converter were in excellent agreement with diffraction theory predictions. In addition to the $TE_{22,6}$ beam, two other low level side lobes were observed. A $TE_{22,6}$ Vlasov-type converter was used to determine that the side lobes were caused by a mix of modes incident on the pre-bunching launcher, which was designed for an input of 100% $TE_{22,6}$ mode. The $TE_{22,6}$ beam was directed into a 1.25 in. diameter corrugated waveguide and calorimetric efficiency measurements showed that 98% of the $TE_{22,6}$ mode at the launcher input was coupled to the HE_{11} mode of the corrugated guide.

Next, four additional reflectors that formed a beam splitting mirror relay were tested. Diode scans and beam expansion measurements showed that the beam splitting reflectors transformed the fundamental Gaussian beam, formed by the two mirror relay, to two Gaussian-like beams of waist w_0 = 1.5 cm. Calorimetric efficiency measurements showed that 52% of the power leaving the gyrotron was found in beam a and 42% of the power was contained in beam b, giving an overall efficiency of 94%. The measured patterns were in excellent agreement with predictions of vector diffraction theory.

The pre-bunching launcher and two mirror relay were then tested in the internal configuration. Measurements of the output beam showed no evidence of the additional side lobes observed in the external experiments. Beam expansion measurements showed that the beam formed by the internal converter expanded in an identical fashion to the beam

formed by the converter in the external configuration. Output beam measurements were in good agreement with predictions of vector diffraction theory.

Lastly, a study of coupling to counter rotating $TE_{\pm m,2,1}$ modes of a gyrotron oscillator was made. Beam alignment experiments, which employed matched left and right Vlasov-type converters, showed that the centered electron beam coupled to the left rotating $TE_{16,2}$ mode, as predicted by linear coupling theory. The beam could be displaced $\sim \pm$ 0.08 cm from center before a change in rotation direction of the output mode was detected. This displacement agrees well with predictions of linear coupling theory for an off axis electron beam. Because alignments to within $\pm$0.025 cm are easily achievable in practice, this study suggests that predicting and maintaining the rotation sense of the output mode is possible and that slight misalignments of the beam will not prevent the use of a rotation sensitive mode converter, such as the Vlasov-type or pre-bunching converters.

Thus, this thesis presents the theory, design, and experimental verification of two high efficiency quasi-optical mode converters for gyrotron oscillators. This thesis also presents a theoretical and experimental study that shows the rotation direction of a gyrotron output mode can be predicted by linear coupling theory and can be maintained throughout operation of the the gyrotron, enabling the use of rotation sensitive mode converters described above.

References

[1] V.L. Granatstein and I. Alexeff, 'High Power Microwave Sources,' Artech House:Boston, 1987.

[2] K. Felch, H. Huey, and H. Jory, 'Gyrotrons for ECH applications,'*Journal of Fusion Energy*, Vol. 9, No. 1, pp. 59–75, 1990.

[3] P.P. Woskov, 'Advantages of using gyrotron scattering for alpha particle diagnostics,' MIT Plasma Fusion Center Report No. PFC/RR/87–16, 1987.

[4] B.E. Paton, V.E. Sklyarevich, and M.M.G. Slusarczuk,'Gyrotron Processing of Materials,'*MRS Bulletin*, pp. 58–63, 1993.

[5] K.E. Kreischer, T.L Grimm, W.C. Guss, A.W. Möbius, and R.J. Temkin, 'Experimental study of a high frequency megawatt gyrotron oscillator,' *Physics of Fluids B*, Vol. 2, No. 3, pp. 640–646, 1990.

[6] V. A. Flyagin, G.S. Nusinovich, 'Gyrotron oscillators,' *Proceedings of the IEEE*, Vol. 76, No. 6, pp. 644-656, 1988.

[7] S.N. Vlasov, L.I. Sagryadskaya, and M.I. Petelin, 'Transformation of a whispering gallery mode, propagating in a circular waveguide, into a beam of waves.' *Radio Engineering*, Vol. 12, No. 10, pp. 14–17, 1975.

[8] O. Wada, M. Hashimoto, M. Nakajima, 'Calculation of radiation from a quasi-optical reflector antenna for whispering gallery mode,' *International Journal of Electronics*, Vol. 65, No. 3, pp. 725–732, 1988.

[9] J.A. Casey, A.W. Möbius, A. Li, K.E. Kreischer, and R.J. Temkin, 'Study of helical Vlasov launchers for MW gyrotrons,' *14th International Conference on Infrared and Millimeter Waves, Conference Digest*, 1989.

[10] A. Li, M. Blank, J.A. Casey, K.E. Kreischer, R.J. Temkin, and T. Price, 'Experimental study of a quasi-optical mode converter for whispering gallery mode gyrotrons,' *15th International Conference on Infrared and Millimeter Waves, Conference Digest*, pp. 210–211, 1990.

[11] A. Möbius, J.A. Casey, K.E. Kreischer, A. Li, and R.J. Temkin, 'An improved Design for quasi-optical mode conversion of whispering gallery mode gyrotron radiation,'*International Journal of Infrared and Millimeter Waves*, Vol. 13, No. 8, pp. 1033–1063, 1992.

[12] G.G. Denisov, A.N. Kuftin, V.I. Malygin, N.P. Venediktov, D.V. Vinogradov, and V.E. Zapevalov, '110 GHz gyrotron with built-in high-efficiency converter,' *International Journal of Electronics*, Vol. 72, Nos. 5 and 6, pp. 1079–1091, 1992.

[13] A. Möbius and J. Pretterebner, 'Conditions to achieve stable propagation of a Gaussian-beam-like mode mixture in a deformed waveguide,' *17th International Conference on Infrared and Millimeter Waves, Conference Digest*, pp. 34–35, 1992.

[14] M. Iima, M. Sato, Y. Amano, S. Kobayashi, M. Nakajima, M. Hashimoto, O. Wada, K. Sakamoto, M. Shiho, T. Nagashima, M. Thumm, A. Jacobs, W. Kasparek, 'Measurement of radiation field from an improved efficiency quasi-optical converter for whispering-gallery mode,' *14th International Conference on Infrared and Millimeter Waves, Conference Digest*, pp. 405–406, 1989.

[15] J.A. Lorbeck and R.J. Vernon, 'Singly curved dual-reflector synthesis technique applied to a quasi-optical antenna for a gyrotron with a whispering-gallery mode output,' *IEEE Transactions on Antennas and Propagation*, Vol. 39, No. 12, pp. 1733–1741, 1991.

[16] A. Möbius and J. Pretterebner, 'Avoidance of edge diffraction effects of WGM-fed quasi-optical antennas by feed waveguide deformation,' *16th International Conference on Infrared and Millimeter Waves, Conference Digest*, pp. 531–532, 1991.

[17] L.A. Weinstein, *Open Resonators and Open Waveguides*, The Golem Press:Boulder, Colarado, pp.139–141, 1969.

[18] S. Ramo, J.R. Whinnery, and T. Van Duzer, *Fields and Waves in Communication Electronic, 2nd Edition*, John Wiley & Sons, Inc.:New York, pp. 739–741, 1984.

[19] S.N. Vlasov and M.A. Shapiro,'Use of bi-involute mirrors to transport caustic surfaces,'*Soviet Technical Physics Letters*, Vol. 15, No. 5, pp. 374–375, 1989.

[20] J.A. Kong, *Electromagnetic Wave Theory*, John Wiley & Sons, Inc.:New York, pp. 376–385, 1986.

[21] S. Silver, Ed., *Microwave Antenna Theory and Design*, Peter Peregrinus Ltd.:London, p. 132, 1984.

[22] W.C. Guss, M.A. Basten, K.E. Kreischer, R.J. Temkin, T.M. Antonsen, Jr., S.Y. Cai, G. Saraph, B. Levush, 'Sideband Mode Competition in a Gyrotron Oscillator,' *Physical Review Letters*, Vol. 69, No. 26, pp. 3727–3730, 1992.

[23] L. Rebuffi and J.P. Crenn, 'Radiation patterns of the HE_{11} mode and gaussian approximations,' *International Journal of Infrared and Millimeter Waves*, Vol. 10, No. 3, pp. 291–311, 1989.

[24] J.L. Doane, 'Propagation and mode coupling in corrugated and smooth-wall circular waveguides,' *Infrared and Millimeter Waves*, Vol. 13, pp. 123–170, 1985.

[25] J.L. Doane, 'Polarization converters for circular waveguide modes,' *International Journal of Electronics*, Vol. 61, No. 6, pp. 1109–1133, 1986.

[26] P. Garin, E. Jedar, G. Jendrzejczak, G. Mourier, F. Payen, L. Teyssier, 'Symmetric and non-symmetric mode in a 200 kW, 100 GHz gyrotron,' *12th International Conference on Infrared and Millimeter Waves, Conference Digest*, pp. 194–195, 1987.

[27] H.A. Haus, *Waves and Fields in Optoelectronics*, Prentice Hall, Inc.: Englewood Cliffs, New Jersey, pp. 128–132, 1984.

[28] A. Yariv, *Quantum Electronics*, John Wiley & Sons, Inc.: New York, pp. 112–117. 1975.

[29] C.P. Moeller, 'Distributed windows,' *Proceedings of the Second International Workshop on Electron Cyclotron Resonance Heating Transmission Systems*, 1992.

[30] F.V. Hartmann, P. Garin, G. Faillon, G. Mourier, G. Tonon, J.P. Crenn, M. Pain, and M. Bon Mardion, 'Numerical analysis of a cryogenically cooled gyrotron window,' *17th International Conference on Infrared and Millimeter Waves, Conference Digest*, pp. 458–459, 1992.

[31] T. Yamamoto, K. Yokokura, A. Kasugai, K. Sakamoto, M. Tsuneoko, and T. Nagashima, 'Development of cryogenic window for high power millimeter wave,' *17th International Conference on Infrared and Millimeter Waves, Conference Digest*, pp. 460–461, 1992.

[32] M.K. Haldar and A.H. Beck, 'Simple derivation of the expression for the synchronous field in circular cylindrical cavity gyrotons,' *Electronics Letters*, Vol. 15, No. 16, pp. 487–489, 1979.

[33] O. Dumbrajs. and L. Shenggang, 'Kinetic Theory of Electron-Cyclotron Resonance Masers with Asymmetry of the Electron Beam in a Cavity,' *IEEE Transactions on Plasma Science*, Vol. 20, No. 3, pp. 126–132, 1992.

[34] A.W. Fliflet, R.C. Lee, S.H. Gold, W.M. Manheimer, and E.Ott, 'Time-dependent multimode simulation of gyrotron oscillators,' *Physical Review A*, Vol. 43, No. 11, pp. 6166–6176, 1991.

[35] C.P. Moeller, private communication, October 1991.